DESIGN METHODOLOGIES

FOR ROBUST LOW-POWER DIGITAL SYSTEMS

UNDER STATIC AND DYNAMIC VARIATIONS

A Dissertation
Presented to
The Academic Faculty

by

Kwanyeob Chae

In Partial Fulfillment
of the Requirements for the Degree
Doctor of Philosophy in the
School of Electrical and Computer Engineering

Georgia Institute of Technology
August 2013

DESIGN METHODOLOGIES

FOR ROBUST LOW-POWER DIGITAL SYSTEMS

UNDER STATIC AND DYNAMIC VARIATIONS

Approved by:

Dr. Saibal Mukhopadhyay, Advisor
School of Electrical and Computer
Engineering
Georgia Institute of Technology

Dr. Sudhakar Yalamanchili
School of Electrical and Computer
Engineering
Georgia Institute of Technology

Dr. Sung Kyu Lim
School of Electrical and Computer
Engineering
Georgia Institute of Technology

Dr. Arijit Raychowdhury
School of Electrical and Computer
Engineering
Georgia Institute of Technology

Dr. Hyesoon Kim
School of Computer Science
Georgia Institute of Technology

Date Approved: June 12, 2013

This work is dedicated to

My family

ACKNOWLEDGEMENTS

"Fear not, for I am with you; be not dismayed, for I am your God; I will strengthen you, I will help you, I will uphold you with my righteous right hand." Isaiah 41:10

First of all, I would like to thank God for giving me strength and wisdom in my life. I also would like to express my sincere gratitude to my research advisor, Dr. Saibal Mukhopadhyay. His optimistic attitude was great encouragement to me for completing my research. As not only my advisor but also my friend, he inspired me to explore technical challenges and encouraged me to overcome my difficulties.

I would like to thank Dr. Sudhakar Yalamanchili and Dr. Sung Kyu Lim for contributions and efforts in serving on my thesis reading committee members. I am also grateful to the other committee members, Dr. Arijit Raychowdhury and Dr. Hyesoon Kim, for insightful comments and suggestions. I would acknowledge the gratitude to my former research advisor, Dr. Joy Laskar. It was my great pleasure to work with him.

This work could not have been possible without the constant encouragement and support of the members of Gigascale Reliable Energy Efficient Nanosystem Laboratory at Georgia Tech. I am grateful to them for active discussions and collaborations.

To my parents, Byungdae Chae and Myungsoon Yoo, my parents-in-law, Kyungsik Park and Okhun Park, my sister, Gilsun Chae, and my sister-in-law, Jiyoung Park, I show my gratitude for their unconditional love and prayers. Especially, I would like to express my deepest love and gratitude to my wife, Jihee Park, and my sons, Juho Chae and Juhyung Chae, for all their endless love, encouragement, and support.

iv

TABLE OF CONTENTS

LIST OF TABLES

LIST OF FIGURES

LIST OF ABBREVIATIONS

CMOS	Complementary metal-oxide-semiconductor
RDF	Random dopant fluctuation
LER	Line-edge roughness
OTF	Oxide thickness fluctuation
V_{TH}	Threshold voltage
NBTI	Negative bias temperature instability
nMOS	n-channel metal-oxide-semiconductor
pMOS	p-channel metal-oxide-semiconductor
ABB	adaptive body biasing
AVS	adaptive voltage scaling
IC	Integrated Circuit
PVT	Process-voltage-temperature
3D IC	Three-dimensional integrated circuit
D2D	Die-to-die
WID	Within-die
TSV	Though-silicon-via
FF	Flip-flop
MSFF	Master-slave flip-flop
SAFF	Sense-amplifier-based flip-flop
LS	Level shifter
CVSL	Cascade voltage switch logic
RO	ring-oscillator

TAVS	Tier-adaptive-voltage-scaling
TABB	Tier-adaptive-body-biasing
FBB	Forward body bias
RBB	Reverse body bias
ZBB	Zero body bias
MC	Monte-Carlo
VCO	Voltage controlled oscillator
PLL	Phase-locked loop
DLL	Delay-locked loop
GM	Global modulator
LM	Local modulator
DM	Duty modulation
LTD	Latch with time-borrowing detection
CS	Clock shifter
CPG	Clock pulse generator
TDC	Time-borrowing detection collector
SPI	Serial peripheral interface
PTB	Programmable-time-borrowing
PLTD	Pulsed latch with time-borrowing detection
PTDN	Programmable-time-borrowing detection network
GPIB	General-purpose interface bus
TB-CS	Time borrowing and clock stretching
PTB-DCG	Programmable-time-borrowing and delayed-clock-gating

SUMMARY

Variability affects the performance and power of a circuit. Along with static variations, dynamic variations, which occur during chip operation, necessitate a safety margin. The safety margin makes it difficult to meet the target performance within a limited power budget. This research explores methodologies to minimize the safety margin, thereby improving the energy efficiency of a system. The safety margin can be reduced by either minimizing the variation or adapting to the variation. This research explores three different methods to compensate for variations efficiently. First, post-silicon tuning methods for minimizing variations in 3D ICs are presented. Design methodologies to apply adaptive voltage scaling and adaptive body biasing to 3D ICs and the associated circuit techniques are explored. Second, non-design-intrusive circuit techniques are proposed for adaptation to dynamic variations. This work includes adaptive clock modulation and bias-voltage generation techniques. Third, design-intrusive methods to eliminate the safety margin are proposed. The proposed methodologies can prevent timing-errors in advance with a minimized performance penalty. As a result, the methods presented in this thesis minimize static variations and adapt to dynamic variations, thereby, enabling robust low-power operation of digital systems.

CHAPTER 1

INTRODUCTION AND OBJECTIVES OF RESEARCH

1.1   Problem statement

Scaling of complementary metal-oxide-semiconductor (CMOS) devices have enabled a high level of integration and a fast switching speed in integrated circuits. As the feature size of a device reaches nanometer nodes, variability of device parameters is inevitably increasing [1]. The variability of CMOS devices is significantly affected by random dopant fluctuation (RDF), line-edge roughness (LER), and oxide thickness fluctuation (OTF). RDF, the variation in the number and the location of dopants, becomes dominant as the number of channel dopants decreases in scaled device and results in threshold voltage (V_{TH}) variation of a device. LER and OTF, which are caused by rough line-edge and silicon-oxide interface, become pronounced in small devices. Those variations contribute to variability in V_{TH} as shown in Figure 1.1 [2]. The increasing V_{TH} variations results in increased variability in circuit performance and leakage.

(a)   (b)
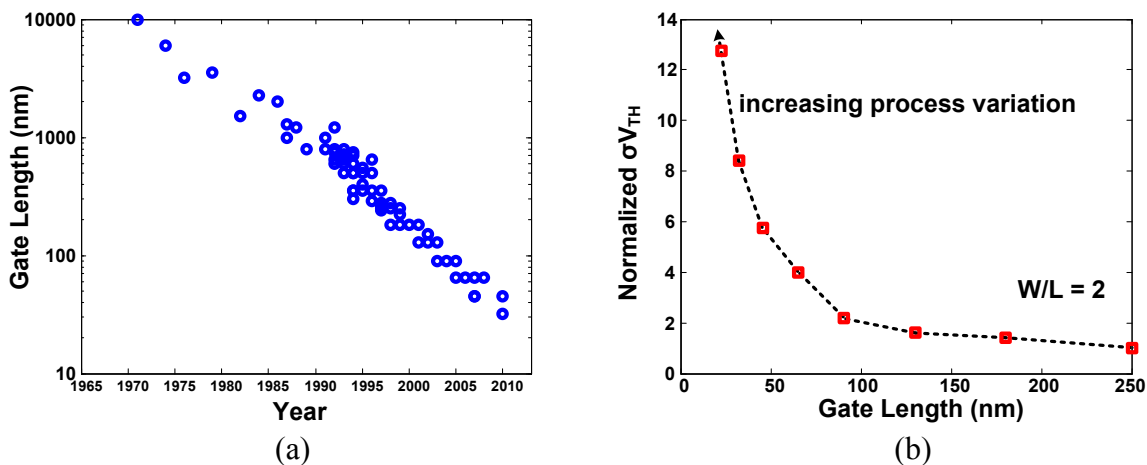
Figure 1.1: CMOS technology trend: (a) Device scaling. (b) V_{TH} variation.

1

Furthermore, the growing number of integrated devices in a chip and the fast switching speed increase the power consumption of a digital system as shown in Figure 1.2 [2]. The rapidly growing power consumption increases the dynamic variations, such as the voltage and the temperature variations. The dynamic variations added on top of the static variations, such as the process variations and the aging effects, significantly affect the speed of a circuit. As static and dynamic variations increase, it is becoming challenging to guarantee reliable operation of a digital system at the target frequency with the tight power budget [3]-[5].

(a)   (b)
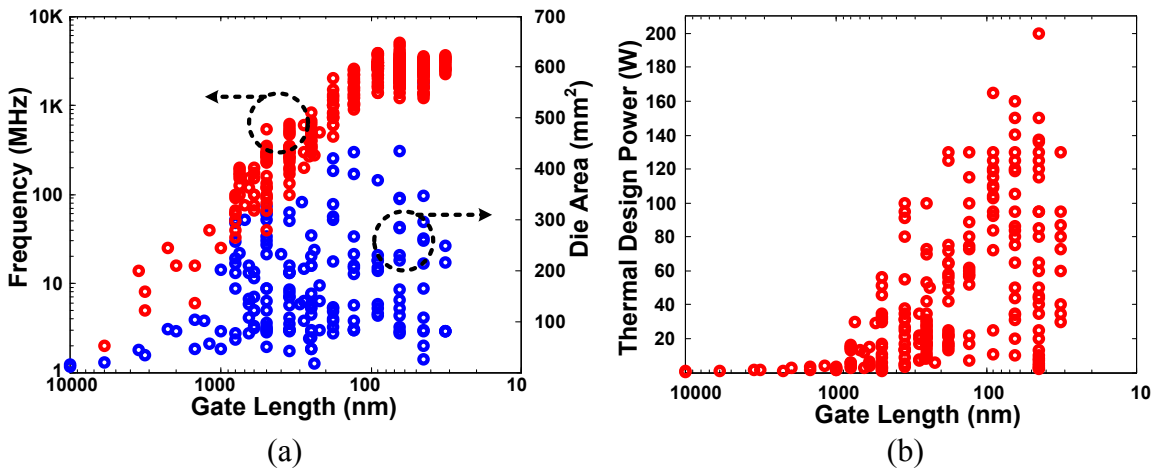
Figure 1.2: (a) Frequency trend. (b) Thermal design power trend.

1.2 Variations

The variations in the process parameters do not change after the chip fabrication. In other words, the process variation is not a function of time. Thus, this variation can be classified as a static variation. On the other hand, there are sources of variations that affect circuit performance as a function of time. An aging effect, a temperature variation, and a voltage variation are time-dependent variation sources. Even if the aging effect is a time-dependent variation source, it can be classified as a near-static variation due to its

very slow impact on circuit performance. Temperature and voltage variations, which are relatively faster than the aging effect, can be classified as dynamic variations.

Aging effects like negative bias temperature instability (NBTI) caused by interface traps in an oxide layer of a device slowly shift the threshold voltage of a pMOS transistor over a long time period. Aging effects slowly degrade performance of a circuit as shown in Figure 1.3. On the other hand, temperature variations affect the chip in the time scale of milliseconds or seconds. Temperature variations affect not only V_{TH} but also the mobility of carriers. Even though increased temperature reduces V_{TH}, it also reduces the mobility of carriers. Thus, increased temperature could increase or decrease a data-path delay according to which impact is more dominant. The relation between temperature and the delay is dependent on a technology and the operating voltage. Assuming normal temperature dependence between temperature and a data-path delay, behavior of temperature and a delay is shown in Figure 1.3. The relation between the operating voltage and a data-path delay is quite obvious and faster than other variation sources.
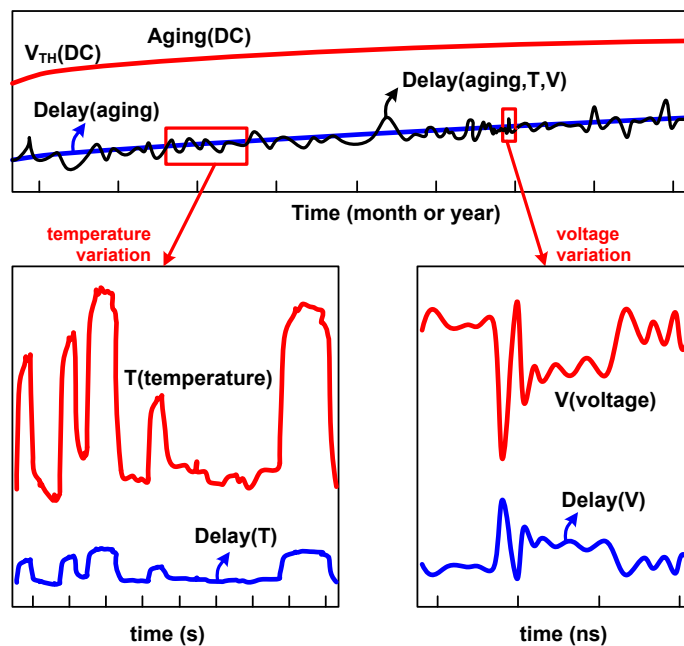
Figure 1.3: Time scale of aging effect, temperature, and voltage variations.

1.3   Safety margin under variations

Under variations like in Figure 1.4, the performance variability of a circuit increases. The traditional design approaches considering worst-corner case necessarily require excessive safety margin to ensure error-free operation of a circuit. The safety margins imply an increased operating voltage or a reduced operating frequency of a circuit. However, all worst-corner combinations are not likely to occur at the same time. Therefore, the safety margin considering all possible worst-corner cases, which is highly unlikely to occur, can lead to excessive power overhead or performance loss during normal operation. Not to lose the gain achieved by device scaling, minimizing the safety margin is a key challenge for low power and high frequency operation of a circuit.
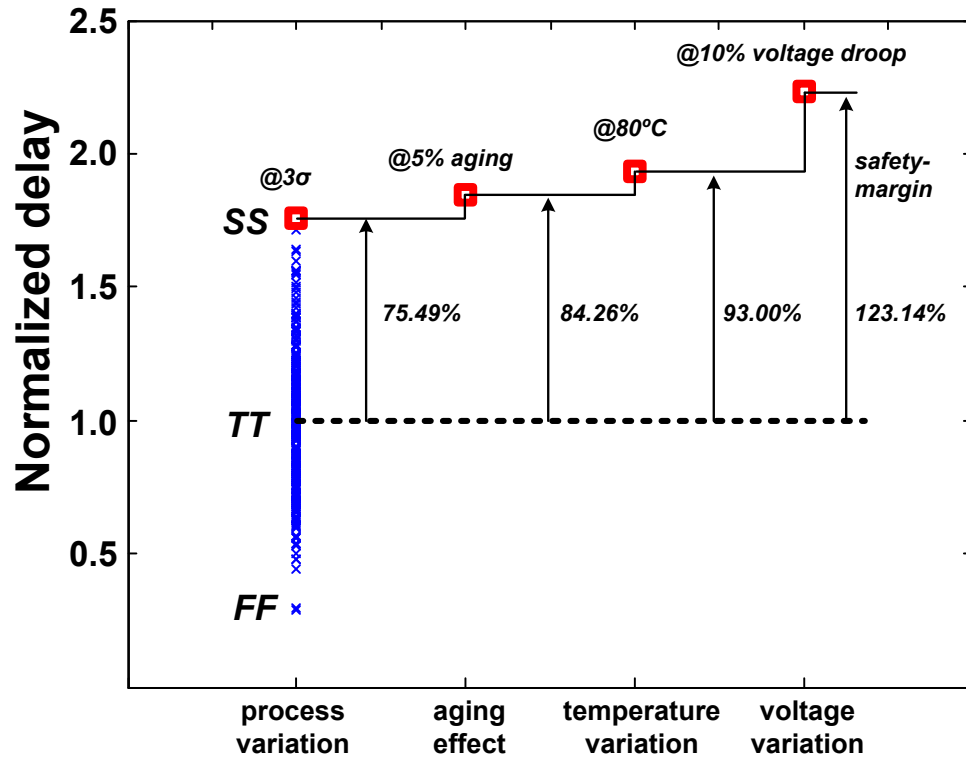
Figure 1.4: Increased safety margin under variations at a 45nm CMOS technology.

1.4   Thesis outline

The goal of this thesis is to develop robust design methodologies for low-power digital systems under static and dynamic variations. Increasing static and dynamic variations lead to excessive safety margins, which increase power overhead or performance loss. Thus, minimizing safety margins is a key challenge to achieving high performance under a power constraint and increasing variations. However, just minimizing safety margin without any adaptation technique to variations do not guarantee error-free operation of digital systems. Safety margins can be minimized by adaptive circuit techniques that compensate for static and dynamic variations.

There are three possible ways to reduce the safety margin under variation. First, the safety margin can be reduced by minimizing the effect of variations on circuit parameters. If the variation can be compensated, required safety margins also can be reduced. Second, adaptively adjusting operating conditions helps tolerate variations. Third, making a circuit error-tolerant under variations can also minimize the safety margin. Without any safety margin, a digital system could have timing errors. If the digital system can detect and manage timing errors, or prevent them, the system can operate with minimal safety margins.

This thesis considers above three approaches to overcome increasing static and dynamic variations. First, this work considers post-silicon tuning methods, which have been explored in prior works for 2D ICs, to compensate for the static process variation in three-dimensional integrated circuits (3D IC). 3D IC is a promising technology, which provides a high level of integration with high performance and low power by stacking different dies utilizing a through-silicon-via (TSV) technology [9]-[18]. Although 3D integration has shown the promise of improving power and performance of a system with the reduced footprint, a 3D IC can be significantly affected by variations [19], [27]. In chapter 3, this thesis focuses on applying post-silicon tuning and developing design methodologies to compensate for variations in 3D ICs.

5

Second, this thesis proposes adaptive clock and voltage generation techniques to compensate for dynamic variations. If a circuit can change the operating condition, such as clock frequency or supply voltage, it can overcome time-dependent variations. Thereby, safety margins for dynamic variations can be minimized. In chapter 4, methodologies for tolerating fast-changing variations are proposed.

Third, this work explores error-tolerant design techniques to eliminate the safety margin. Design methodologies in chapter 3 and chapter 4 are based on replica circuits. In chapter 5, timing-violation detection and error-prevention methodologies in real paths are explored. Previous adaptation techniques focus on preventing errors utilizing replica circuits. On the other hand, this approach focuses on preventing errors in real data paths without replica circuits. The replica-based approaches have two major limitations; mismatches between replica circuits and real data paths; and control speed from the noise sensing to the adaptation. If timing-errors can be recovered or prevented even after the error condition occurred, the safety margin is no longer required.

This thesis presents various solutions to minimize static variations and adapt to dynamic variations considering design types and variations types. As a result, the proposed approaches can minimize safety margins while maintaining robust operation, thereby achieving robust low-power operations of digital systems.

CHAPTER 2

RESEARCH TRENDS

2.1   Introduction

Overcoming static and dynamic variations is important for meeting a performance target with a reduced supply voltage. Without adaptive design techniques of compensating for variations, excessive safety margins are required. Excessive safety margins require considerable design efforts to meet target performance or significant performance loss to guarantee reliable operation. Since the corner-based design approaches consider the worst case conditions, for target performance under variations, the size of a circuit should be increased at the expense of higher power and cost. However, the worst-corner case occurs only when the process, the voltage, and the temperature are all in the worst corner at the same time. The probability that all the worst conditions occur simultaneously is very low. Therefore, under normal conditions, most chips are operating with excessive safety margins. Thus, minimizing safety margins is a key challenge to achieving high performance under increasing variations. Safety margins can be minimized by adaptive circuit techniques that compensate for static and dynamic variations.

Different variations occur in different time scales. First, process variation is determined after integrated circuit (IC) fabrication. Thus, it can be assumed to be static since it does not change over time while ICs are operating. Second, the aging effect degrades IC performance over a long time period, i.e., 1~3 years. Since this degradation of a device is very slow process, it can be classified as near static variations as shown in Figure 2.1. Third, the temperature variation is affected by the power consumption of ICs. The power consumption is strongly dependent on workloads of ICs. Significant change of

workloads necessarily leads to the variation in power consumption, which results in variation in heat dissipation. However, significant workload changes in the order of milliseconds or seconds. In addition, the thermal time constant of silicon-based ICs are in the order of milliseconds. As a result, the changing speed of temperature is relatively faster than the aging effect and can be classified as a slow-dynamic variation as shown in Figure 2.1. Fourth, the voltage variations, which are affected by power demands and the quality of the power delivery network, affect data-path delays significantly. It is a faster process than other variations and occurs in ns to μs order. Thus, the voltage variation is a relatively more difficult variation to tolerate compared to other variations due to its significant impact on delay and the fast changing speed.
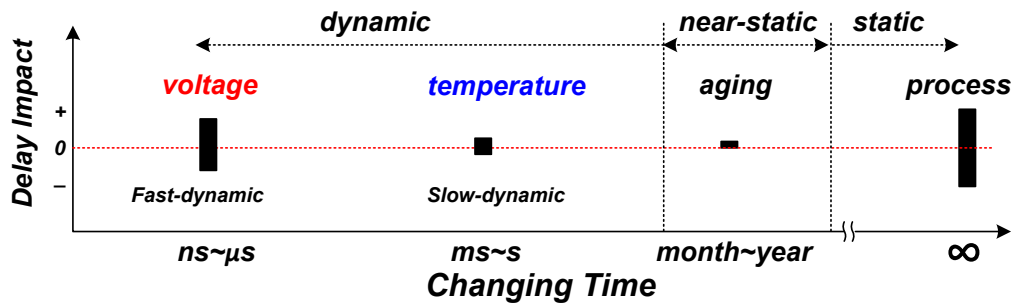
Figure 2.1: Speed and impact amount of variations.

Static and dynamic variations are classification based on the temporal behavior of the variations. The variations can be sub-categorized into local and global variations in terms of spatial behavior as shown in Figure 2.2. Local variations only affect local areas near the variation sources. Examples of local variations are within-die (WID) variations, local hot spots, and local voltage droops. Unlike the local impact of local variations, global variations affect the whole chip. Examples of global variations are die-to-die (D2D) variations, global temperature, and global voltage droops.

8
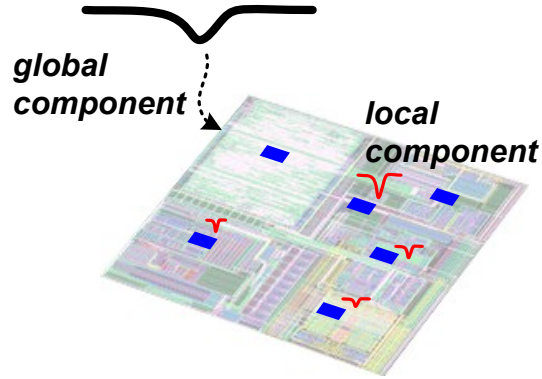
Figure 2.2: Local and global variation components.

2.2   Post-silicon tuning approach

Process-parameter variations result in variations in performance and power. WID variations cause mismatches in the transistor characteristics within a die. In addition, each die has different global device parameters. These parametric variations increase the performance variation. Because of the performance variation, some dies cannot be accepted because of either low performance or excessive power. The number of acceptable dies will decrease unless the frequency target reduces. In other words, increased process variations indicate either yield- or performance-loss.

Two major techniques are widely used to minimize performance variations. One technique is to apply different supply voltages according to the speed of a die [3], [39], [40]. If the die is slow, a high supply voltage is applied to make the die fast. On the other hand, if the die is fast, a low supply voltage is applied to make the die slow. This technique is referred to as adaptive-voltage-scaling (AVS). The other technique is to apply a non-zero body-to-source bias to modulate the threshold voltage of a transistor as shown in Figure 2.3 [4], [5]. A reverse body bias increases the threshold voltage and makes a die slow. On the contrary, a forward body bias decreases the threshold voltage of

a transistor and makes a die fast. This technique is referred to as adaptive-body-biasing (ABB). Thus, it is possible to control the transistor speed through AVS or ABB after chip fabrication. These post-silicon-tuning methods help compensate for the delay spread and eventually minimize performance variations.
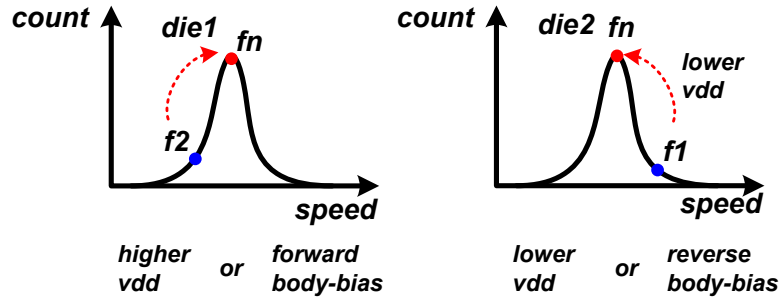
Figure 2.3: Concept of post-silicon tuning (AVS and ABB).

Post-silicon-tuning methods are widely used in 2D chips to minimize static variations, such as process variations and aging effects, which change over a long time period [6]. However, limited studies have been performed to understand the effect of variability and to develop post-silicon-tuning methodologies in 3D chips. This work evaluates the effectiveness of post-silicon tuning in 3D ICs. Then, a methodology for post-silicon tuning for 3D ICs is proposed.

2.3   *Non-design-intrusive dynamic adaptation*

An attractive approach is to utilize critical-path replica circuits of which delays are strongly correlated with the critical-path delays of a real-logic block as shown in Figure 2.4 [52]-[54]. When timing errors are likely to occur in replica circuits, the supply voltage or the operating frequency can be dynamically changed to prevent a chip failure. This replica-based approach increases variation tolerance of a circuit since it adaptively changes the operating condition of a circuit to prevent a chip failure. However, different

10

geographical locations of the actual circuits and replica circuits on a chip can result in different process-voltage-temperature (PVT) variations [63]-[66]. To compensate for a mismatch, an adaptive design based on replica circuits cannot totally eliminate safety margins. However, since this replica-based method is not an intrusive technique, any modification of the main circuit is not required. The critical challenge of this approach is to minimize the delay from sensing environmental variations to changing operating conditions to handle fast-changing variations. Because of this challenge, this method is useful for adapting a circuit to slow-changing global noise, which affects the whole chip. This thesis proposes a method for adaption to fast-changing variations with the replica-based approach, which requires no circuit modification.
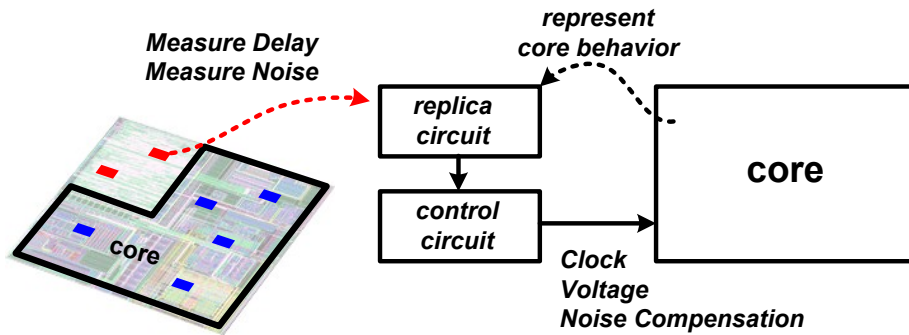
Figure 2.4: Concept of non-design-intrusive dynamic adaptation.

2.4   *Design-intrusive dynamic adaptation*

An alternative approach is to use in-situ error-detection and error-correction mechanisms to tolerate the variation while operating without safety margins [63]-[71]. Without any safety margin, voltage and temperature variations (i.e., the dynamic environmental variations) can cause timing errors. Thus, it is necessary to detect timing errors in the real data paths. If a system can recover from the detected errors, it can operate without any safety margin. Above all, in-situ-based approach can tolerate fast local noise because it detects and corrects errors in the real data paths. Thereby, this

11

approach can potentially eliminate the safety margin. However, the main circuit requires modification for implementing error detection and recovery circuits in the real data paths. Therefore, the in-situ-based approach is a design-intrusive technique. In addition, all error recovery methods incur additional power and performance penalties. Thus, if errors occur frequently, the penalty can become significant. If the penalty associated with error recovery can be reduced, the performance and the power of pipelined systems can be significantly enhanced [66]. Traditionally, an architectural replay, i.e., re-executing erroneous instructions, is used for error-recovery. Thus, the error-recovery mechanism becomes a platform-dependent solution if the architectural replay, which is embedded in a microprocessor, is used for error correction. Because of the increased penalty for error correction and the platform dependency, this approach cannot be used in general circuits. This research proposes a method for preventing timing errors under fast-changing variations with the minimized performance penalty in general circuits, such as state-machines and control circuits including feedback paths.
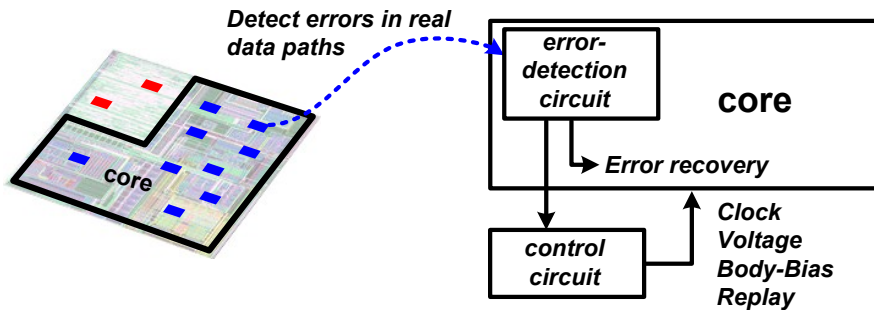
Figure 2.5: Concept of design-intrusive dynamic adaptation.

CHAPTER 3

POST-SILICON TUNING APPROACH

3.1　Introduction

The methodologies to modify parameters of ICs after the fabrication are called post-silicon tuning. Post-silicon tuning became more popular for digital and analog circuits in deeper submicron technologies to achieve the target yield or the target performance. The post-silicon tuning in analog circuits has a long history since analog circuits are very vulnerable to mismatches [6]. Even small mismatches in analog circuits can cause significant output offsets. Post-silicon tuning for analog circuits focuses on repairing mismatches of devices utilizing fuses or tunable capacitor/resistor bank arrays. In digital domains, various solutions for post-silicon tuning, such as AVS, ABB, and redundancy, have been explored. Prior-arts focused on solving variation problems in 2D ICs.

A three-dimensional integrated circuit (3D IC) is a promising technology, which provides a high level of integration with high performance and low power by stacking different dies utilizing through-silicon-vias (TSV) [7]-[18]. Although 3D integration has shown the promise of improving power and performance of a system with the reduced footprint, a 3D IC can be significantly affected by variations [17]-[19], [27]. From the process perspective, a 3D IC can be thought of as multiple separate chips fabricated in different wafers. In other words, when different dies are stacked, dies come from different lots and wafers. This wafer-to-wafer or lot-to-lot variation can lead to significant performance mismatch between different dies in a 3D chip. Therefore, in a 3D IC, both WID and D2D process variations contribute to within-chip variations as shown in Figure 3.1. Moreover, variations in resistance and capacitance properties of the TSV also add to

total path-delay variations in 3D ICs [19]. Therefore, it is necessary to develop methodologies to minimize variations in a 3D IC technology. Otherwise, performance gain achieved by stacking different dies can be lost.
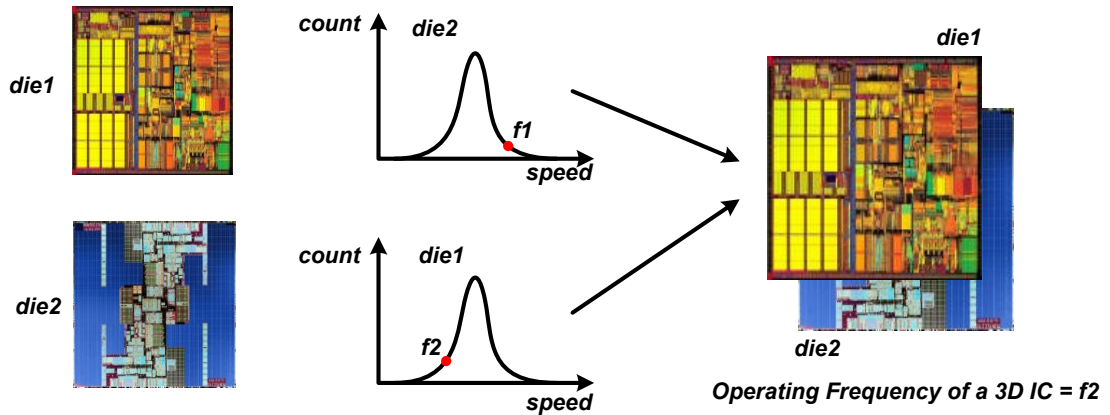
Figure 3.1: D2D variation issue in 3D ICs.

3.2   Variation challenges in 3D ICs

The variation in process parameters is a key challenge to performance or leakage-limited yield of designs in nanometer technologies [62]. Die-to-die (D2D) and within-die (WID) variations in process parameters can lead to significant chip-to-chip variations in the delay and the power of logic circuits. The post-silicon adaptation, such as voltage-scaling and body-biasing, can be used to improve parametric yield of a chip [3], [4]. The objective of post-silicon tuning is to tune the supply voltage or the body bias of a chip depending on the global process corner [3], [4]. The D2D variation in process is the collective effects of lot-to-lot, wafer-to-wafer, and within-wafer variations caused by different sources of manufacturing imperfections. For logic circuits where transistors are normally larger than minimum size devices, D2D variations can dominate over WID variations.

From the process perspective, a 3D chip can be thought of as multiple separate chips fabricated in different wafers. In other words, when the different dies are stacked,

the dies come from different lots and wafers. This can lead to significant variations between two dies in a 3D chip [9]. Therefore, in a 3D IC, both WID and D2D variations contribute to within-chip variations [10]-[13]. This is unlike 2D ICs, where the within-chip variation is determined only by WID variations. Further, variations in RC properties of the through-silicon-via (TSV) also add to total variations in 3D ICs [10]-[13]. It is necessary to develop methodologies to reduce the delay and leakage spread of 3D chips considering within-chip and chip-to-chip variations caused by D2D and WID variations.

Understanding and mitigating the effect of process variations on 3D ICs are evolving fields. Limited studies have been performed to model the effect of variability on 3D chips, to understand the effect of different physical-design choices on the variation characteristics, and to develop design-level methods to improve parametric yield [10]-[13]. Methods for process-corner-aware bonding of dies have also been studied to optimize yield [14]. However, such bonding approaches are primarily limited to die-to-die 3D bonding. In a wafer-to-wafer bonding 3D technology, it is difficult to achieve an optimal bonding configuration for all dies in a wafer [15]-[17]. This chapter explores two design methodologies for reducing variability in 3D ICs considering different design cases.

This work considers two design scenarios. First, two tiers are implemented with different independent clock networks. This design case includes processor-memory and processor-processor tiers with independent clock networks. This 3D integration scenario is referred to as a block-level 3D integration. Second, a functional block can be implemented in separate tiers with one 3D clock network. This scenario can be classified as a logic-level 3D integration. For the 3D design scenarios above, widely used adaptation techniques in 2D designs are considered in this chapter. Adaptive voltage scaling (AVS) and adaptive body biasing (ABB) are widely used techniques to offset D2D variations as the post-silicon tuning methodologies [3], [4]. In AVS, higher V_{DD} is assigned to a slower die (to improve speed), and lower V_{DD} is assigned to a faster die (to

15

save power) [3]. Effectiveness of AVS is studied for reducing logic delay variability in 3D ICs [27]. However, AVS for clock networks with multiple clock TSVs is challenging because all clock TSVs will require level shifters which will introduce additional source of delay variations (i.e., skew) and power overhead. The second approach is to use ABB, where forward body bias is applied to slow dies and reverse body bias is applied to fast dies [3]. ABB has a significant advantage over AVS for 3D clock network, as body biasing does not require different V_{DD} for each die. Hence, the signals between different dies can be interfaced without level shifters.

Considering the block level 3D integration, this thesis presents tier-adaptive-voltage-scaling (TAVS) as a methodology for post-silicon tuning for data paths in 3D ICs considering D2D and WID process variations. TAVS reduces data-path delay variability of 3D ICs by independently tuning supply voltages of different tiers. The circuit issues associated with the design of TAVS including level shifters are discussed. This methodology is developed for the case when

For the logic level 3D integration, this thesis presents tier-adaptive-body-biasing (TABB) as a methodology for post-silicon tuning for 3D clock networks in 3D ICs under D2D and WID process variations. TABB reduces skew and slew variability of 3D ICs by independently applying adaptive body biases to different tiers. Digital circuit techniques to sense D2D variations of pMOS and nMOS transistors are discussed.

3.3   Tier-adaptive-voltage-scaling for 3D ICs

This section *evaluates the possibility of post-silicon adaptation to* mitigate the effect of within-chip and chip-to-chip variation *and improve parametric yield of 3D ICs.* Tier-adaptive-voltage-scaling (TAVS) as a post-silicon tuning technique is proposed to reduce the spread in the delay distribution of 2D and 3D paths, and hence, that of 3D chips. The methodology of TAVS senses the process corner of individual tier (i.e., dies) in

a 3D chip and independently adapts the supply voltage of individual tiers to control the delay spread. The concept and design of TAVS is presented and impact of TAVS on delay distribution of 3D ICs is shown. This section makes the following contributions; 1) this study analyzes the effect of process variations on different types of critical paths in 3D design, namely, 2D critical paths contained in a single die and 3D critical paths that traverse between dies; 2) this study discusses efficient methods for voltage-level conversion for 2D and 3D paths to realize TAVS-based 3D design; 3) this study evaluates the effectiveness of TAVS considering different types of 2D and 3D critical paths. TAVS simulation results show 26-39% reduction in delay variability of 2D and 3D paths in 3D ICs.

3.3.1 Effect of die-to-die variation in 3D design

In this section, the impact of D2D variation on the delay distribution of different types of paths in a 3D design is analyzed. Note the D2D variation in 3D ICs contributes to within-chip variation i.e. different logic blocks and/or different segments of a path in a 3D design can come from different inter-die process corners. First, different types of paths that can exist in a 3D design are classified. The first type is *2D path* (or non shared paths) that are contained in a single die (does not cross the die boundary) like a 2D design (Figure 3.2). The second type is shared paths or *3D paths* which cross the boundaries of two dies as shown in Figure 3.2. In the 3D paths, the balanced (path2b) and the unbalanced (path2u) case are classified according to the partitioning of the paths between dies (i.e. TSV insertion point). The extremely unbalanced (path2us) case is a special case (Figure 3.2). First, the effects of variations on these different types of data paths are analyzed.
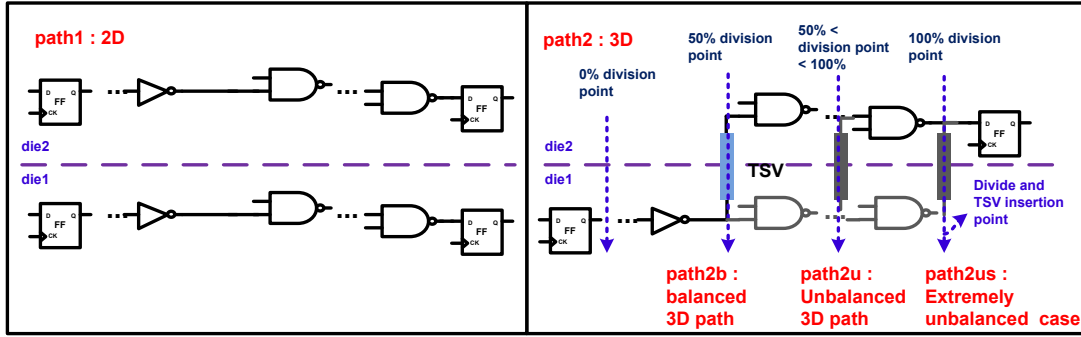
Figure 3.2: Path classification for 3D ICs.

3.3.1.1 *Non-shared 2D paths*

There are paths that reside only in one die. In this case, the path will be affected only by the WID and D2D variations of one die. The impact of variations on the delay of a two-tier 3D IC with 2D critical paths in each die is analyzed. The maximum delay of each die is determined by the most critical path of that die. This section focuses on a typical condition when the critical paths of two dies are designed for equal delay. Each die will have independent delay distribution of the critical path. If dies are selected randomly for stacking, the operating speed distribution of the 3D chip will depend on the maximum of two independent delay distributions as shown in Figure 3.3.
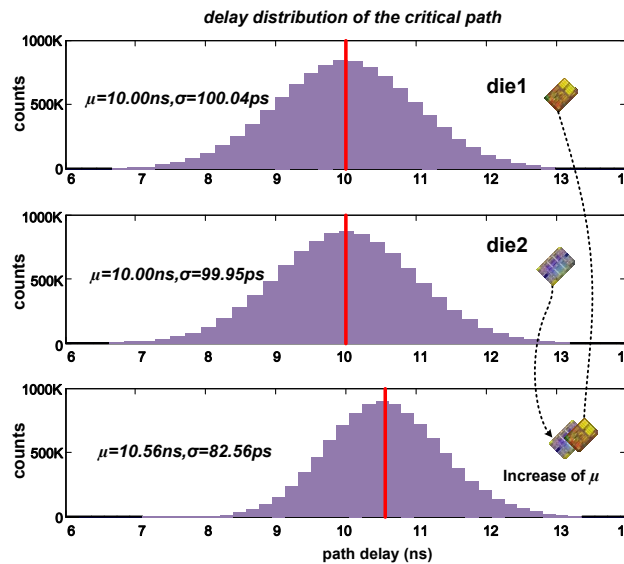
Figure 3.3: Process variation impact in 2D paths in 3D ICs.

3.3.1.2   3D paths

A 3D path is separated into different dies and segments of the path are connected through TSV. The case where the path contains only one TSV is analyzed. Different insertion points of the TSVs in a 3D path are considered as shown in Figure 3.2. First, TSV variation was excluded assuming equal standard deviation for threshold voltage variations of two tiers. In Figure 3.2, 0% division point indicates the case where the all logic gates in path are placed in the die2 and the signal source is a flip-flop (FF) in the die1. On the other hand, 100% division point means the case where all logics are in the die1 and the signal sink is a FF in the die2.

The reduced impact of D2D variation is observed when the logic gates in the path are separated into different dies. First, the process variation of two dies is assumed to follow independent normal random distribution with same standard deviations (Figure 3.4(a)). Since the uncorrelated D2D mismatches between the dies can offset each other, separating a path into different dies helps reduce delay spread. Hence, when the standard deviation of process variations of two dies are same, (a) 0% or 100% division point results in highest standard deviation for path delay, and (b) 50% division point (i.e., the evenly balanced case) results in the minimum standard deviation of path delay. In the analysis considering WID variations, WID variation also changes this minimum standard deviation point.

In 3D chips TSV variation will be introduced on top of D2D and WID variation. To observe the impact of TSV variation, the resistance and capacitance variation of TSVs are included, and variability of 3D paths is estimated (Figure 3.4(b)). The capacitance and the resistance of TSV are set to 35fF and 50mΩ, respectively [18], [19]. The σs of the capacitance and the resistance of TSVs are assumed to be 15%. Further, the delay spread is analyzed considering both device and TSV variability as a function of TSV insertion point. Under all insertion point, the TSV variability increases the delay spread of 3D paths (Figure 3.4(b)). In addition, the more balanced 3D paths showed the lower delay

spread even with the TSV variation. With the TSV variability, the unbalanced 3D paths can have higher variation than 2D paths. The most balanced 3D paths have minimum delay spread that can be smaller than 2D paths even with TSV variation.

Next, the scenario when standard deviations of process variations of the two dies are different is studied. The estimated delay variation for the 3D path with the scenarios when all logic is placed in either die 1 or die 2 is compared as shown in Figure 3.4(c). Higher D2D variation for die1 implies that variation of the 3D path delay is more strongly affected by D2D variation of the die1. As D2D variations in die 1 increase, the minimum standard deviation point of 3D path delay moves towards 0% division point. This is because a reduced portion of logic in the die1 decreases the influence of higher D2D variation of die 1 on the 3D path delay.

From the above observation it can be found that the variation aware 3D partitioning methods that aim to balance the nominal delay of the segments of critical paths in two dies help reduce the delay variability of 3D paths. Also, this optimal division point is a strong function of the relation between the standard deviations of the D2D variations of the two dies.

(a)   (b)   (c)
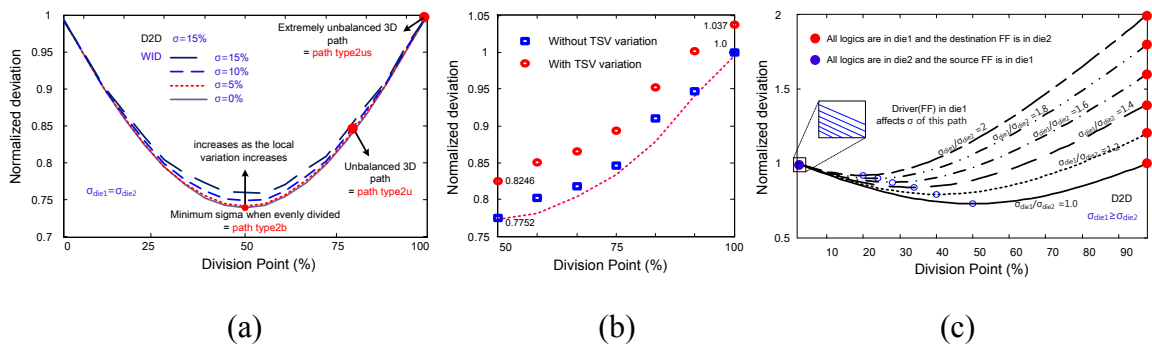
Figure 3.4: Standard deviation of delay variations in 3D paths considering different path division (a) neglecting TSV variations and assuming standard deviation (σ) for D2D variations in both dies same, (b) considering TSV variations (same D2D variations for two dies), and (c) considering different standard deviations of D2D variations for two dies.

3.3.2   Tier-adaptive-voltage-scaling methodology

In this section, the proposed tier-adaptive-voltage-scaling (TAVS) approach is discussed for post-silicon tuning of 3D chips. In a 2D chip, the adaptive voltage scaling can offset D2D variation of a chip with different voltage assignment. For a 3D chip, the adaptive voltage scaling needs to assign different voltage to each tier independently. This may cause different segments of a path (critical or non-critical) to reside in different voltage domains (i.e., different tiers) requiring level shifters within a path. The overall system architecture of the TAVS system with the on-chip regulator is shown in Figure 3.5. The proposed TAVS system considers independent supply domains for individual tiers controlled by on-chip voltage regulators. The high level system components include delay variation sensors, control logic, and voltage regulator. A delay-based sensor detects the process corner of individual dies. After power is on, the initial regulator output is nominal voltage. Under this condition, an enable-pulse input is applied to the delay sensor. Depending on the output of the delay sensor, the supply voltage is selected using the on-chip power regulator. After the output voltage of on-chip regulator is changed, the system can start normal operations. In this section, the key circuit components of the proposed system are discussed.
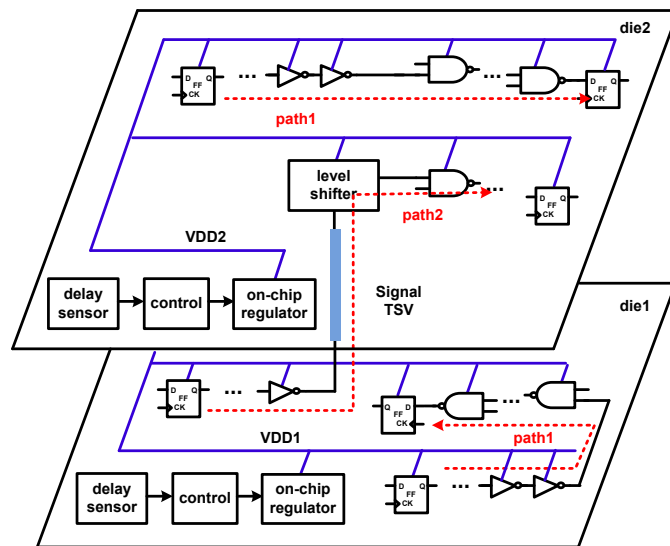
Figure 3.5: The system architecture of tier-adaptive-voltage-scaling.

3.3.2.1 *Delay variation sensor*

The first circuit component is the sensor to characterize the D2D variation. In this chapter, a ring-oscillator-based delay sensor is used to sense the D2D variation of a die. Frequency of a ring oscillator changes due to process variation and this signature can be used to detect the process corner of a die. According to the speed of gates, the generated clock frequency is different. If a counter is used to count the number of edges of the generated clock, the counter value indicates the speed of the logic gates. To detect D2D variations, the effects of WID variations need to be minimized. The effect of WID variation on the D2D delay sensor can be reduced by increasing the number of chains in the ring oscillator [20].

3.3.2.2 *Level shifter*

Level shifters are required within a 3D path to convert the different voltage levels. The level conversion is always performed in the receiver side of a TSV. The objective is to ensure that only one supply voltage domain exists within a die. This creates additional challenge as two different VDDs within one side of the TSV are not possible (either driver or receiver)

This chapter considers two different types of level shifters to achieve the above goals (Figure 3.6). The *level shifter Type1* (LS Type1) requires single input and single voltage and can be applied without the input or the supply constraints [21]. The entire circuits remain in the receiver side of the TSV and no design modification is required in the driver side. In the LS Type1, the diode-connected M0 transistor has voltage drop as much as threshold voltage (V_{th}). Thus the supply voltage level of the input buffer (inv0) is V_{DD2}-V_{th}. Therefore, the propagation delay of falling transition is slow when the single-ended level shifter is used. *Level shifter Type2* (LS Type2) is the modified cascade voltage switch logic (CVSL). The propagation delay of the CVSL is small since it has differential inputs. Thus, the LS Type2 is much faster than the LS Type1. However, since

the CVSL is a differential logic, the inverter should be placed in the other different voltage domain. It implies that two TSVs are required to convert voltage levels incurring additional area and power for the extra TSV.

In the spice simulation, the delay of the LS Type2 is less sensitive to different V_{DD} conditions compared to the LS Type1. The power dissipation associated with the level shifter, which is designed to achieve a target delay ~50ps is estimated. Table 3.1 summarizes the estimated power of the driver (inverter) and the TSV. Since introducing the LS Type2 incurs much higher power overhead, the LS Type2 should be carefully introduced to control power overheads.
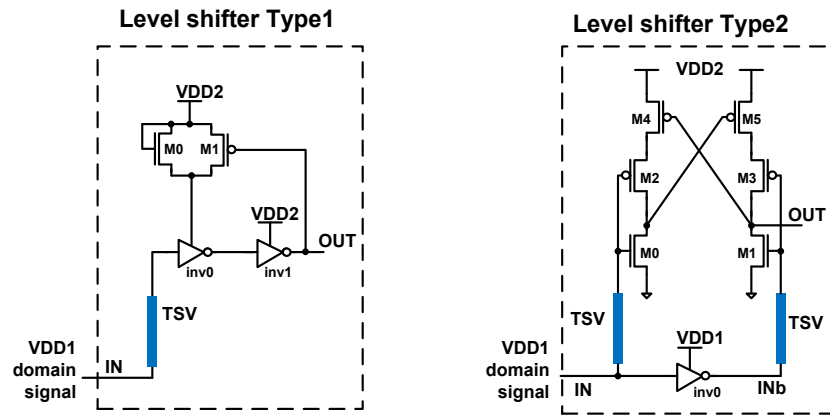
Figure 3.6: Circuit diagrams of level shifters.

Table 3.1: Power analysis.

Power overheads of level shifters (500MHz, 1V, and α=0.5).			
	Total power	LS power	Overhead
Driver + TSV	11.77uW	-	-
Driver + TSV + LS Type1	11.30uW	2.06uW	1.59uW
Driver + TSV + LS Type2	20.16uW	2.35uW	10.74uW

3.3.2.3   *Methodology for level shifter insertion*

The discussion in the previous sub-section shows that the LS Type2 introduces more power and area overhead but less delay penalty. On the other hand, the LS Type1 reduces power/area overhead but incurs additional delay penalty. All 3D paths (i.e., paths with a TSV) do not have equal delay and are not equally timing critical, but all of them will require level shifters for TAVS compatibility. The delay criticality of the 3D paths can be considered to preferentially insert the LS Type1 or the LS Type2. If the 3D path is not timing critical, the LS Type1 can be used to minimize the area and the power overhead (Figure 3.7). However, if the 3D path is timing critical, the LS Type2 is recommended as it significantly reduces the delay overhead. Finally, if a path is totally unbalanced (like the path Type2us) the receiver end of the TSV directly terminates in a flip-flop (Figure 3.7). In this case, it is proposed to convert the flip-flop itself to a level converting flip-flop to reduce the delay overhead of level shifters. A sense-amplifier-based flip-flop (SAFF) is a good solution for level shifting flip-flops [22]. With the SAFF, voltage scaling can be applied without level shifters in the extremely unbalanced paths.
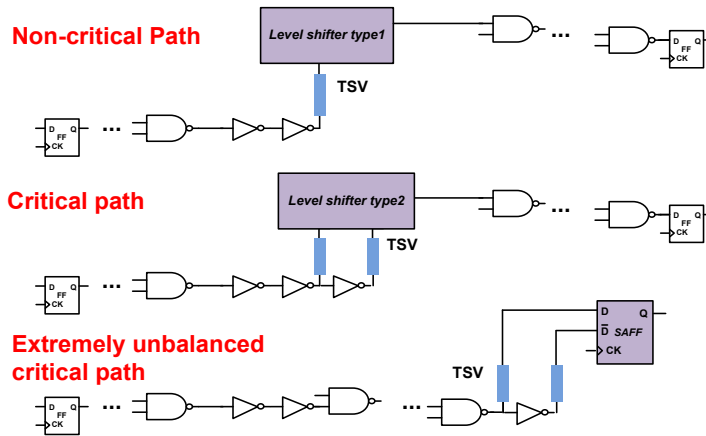
Figure 3.7: Path-delay-based insertion of different types of level shifters.

3.3.3 Simulation results

The test system was simulated in a predictive 45nm technology [23]. The behavior of the power regulator was modeled with Verilog-A. The outputs of the regulators were restricted to three voltage levels (0.9V, 1V, and 1.1V). For generic analysis of the proposed TAVS, a statistical analysis framework (instead of focusing on a specific design examples) was considered. First, different types of critical paths (i.e., 2D critical paths and 3D critical paths) are assumed to exist in a 3D design. Further, both single-ended (LS Type1) and differential (LS Type2) level shifters for 3D critical paths are considered to study the delay overhead. Next, D2D and WID variations in threshold voltage of the devices are considered to study the overall functionality and performance of TAVS system. For the analysis, standard deviations of D2D and WID in threshold voltage, and RC variations in TSVs are all considered as 15%.

3.3.3.1 *Statistical analysis of voltage assignments*

First, the statistical behavior of the voltage assignments for different tiers and different chips are analyzed. 1000 Monte-Carlo simulations are performed, and D2D and WID variations are assigned to different dies for designs in tier 1 and tier 2. Then, they are randomly bonded. Simulation of the proposed TAVS architecture was performed using SPICE. First, the statistical variations in the sensor outputs are monitored. As shown in Figure 3.8, different sensor outputs of each tier, which indicate different D2D corners, were obtained. Next, the control logic uses this sensor output and interacts with the power regulator to generate different voltage assignments for different tiers.
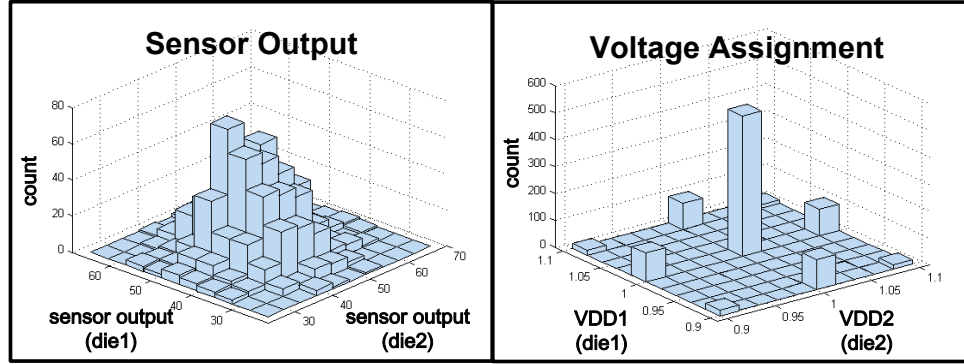
Figure 3.8: The statistical analysis of the sensor output (left) and voltage assignments (right) for different tiers and different chips.

3.3.3.2   *Analysis of delay variation in different paths*

The impact of D2D and WID variations in V_{TH}, TSV variations in different types of paths, and the effect of TAVS are analyzed. The process variations in the level shifters are considered. Figure 3.9 summarizes the mean and standard deviations ($\mu+3\sigma$) of different types of path delay distributions. The statistics were generated considering 3D designs composed of 2 tiers with appropriate supply voltages after TAVS as shown in Figure 3.8. With TAVS, the mean delay of 2D critical paths reduces marginally, but delay spread reduces significantly (~34%). For balanced 3D paths with intermediate level shifter, the mean delay increases due to the delay of the level shifters. In particular, inserting the level shifters only (without TAVS) results in higher mean and standard deviations of delay. The mean increase is more with single-ended (LS Type1) compared to differential (LS Type2) level shifters. However, the delay spread reduces significantly in both cases with TAVS compared to the case without level shifters. With level shifters and TAVS, the mean delay increase (compared to no TAVS) is limited to 5.9% and 3.1% with LS Type1 and LS Type2, respectively. The reductions in standard deviations are ~36% in both cases (compared to no TAVS case). For highly imbalanced 3D paths, TAVS and SAFF provide maximum advantage. Without TAVS, the imbalanced paths suffer significantly from D2D, WID, and TSV variations. TAVS results in significant (~39%)

26

reductions in the delay spread. A SAFF results in a lower spread with almost no change in the mean delay for extremely unbalanced paths. Figure 3.9 summarizes the observations on different types of paths and TAVS.
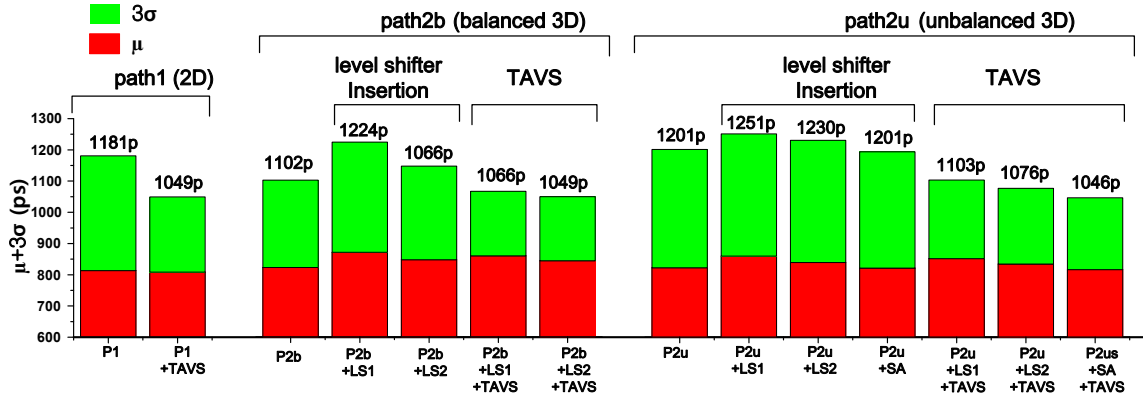
Figure 3.9: Simulation results with TAVS in different path types.
* P1=path1 (2D path), P2b=balanced path2 (3D path), P2u=unbalanced path2 (3D path), and P2us=extremely unbalanced path2 (3D path).
* LS1 =LS Type1, LS2=LS Type2, and SA=SAFF.

3.3.3.3   *Power and area overhead analysis*

The effect of TAVS on leakage and dynamic power distribution is analyzed. A statistical analysis is performed considering a design with 100K NAND2 gates in each tier. The process corner and voltage assignments obtained from the MC simulations discussed in Figure 3.9 are used for power estimates. TAVS marginally reduces both leakage and dynamic power spread (Figure 3.10).

The power and the overhead associated with TAVS and the level shifters are analyzed. Based on previous studies (e.g., [8]), it is considered that the two tiers of 100K NAND2 gates are connected using 1000, 2000, and 3000 TSVs. The maximum (when all TSV paths are replaced with LS Type2) and minimum (when all TSV paths are replaced with LS Type1) power and area overheads are computed for each case. The NAND2 gate power was estimated considering an average of fanout-of-4 load and 10fF of interconnect

27

capacitance. The estimated power overheads are shown in Table 3.2. To estimate the area overhead, the area of each die is evaluated considering 100K NAND2 gate ($1.8772\mu m^2$ per gate based on [23] and predictive 45nm node), and additional 30% of area for routing and power network [26]. The area of level shifters is estimated from the layout. The estimated maximum and minimum area overheads (compared to a TSV and a driver) due to the LS Type1 ($2.964\mu m^2$) and the LS Type2 ($1.976\mu m^2$) with an additional TSV including keep-out zone ($16\mu m^2$) are also shown in Table 3.2 [24]. The area overhead caused by the delay sensor ($107.47\mu m^2$) is 0.04%. Although the on-chip regulator incurs the area overhead (depending on the current demand of a chip), it helps reduce the voltage droop. This relaxes the constraints on the off-chip regulators and on-chip decoupling capacitors. It also enables fast dynamic voltage-frequency-scaling due to fast voltage transition [25].
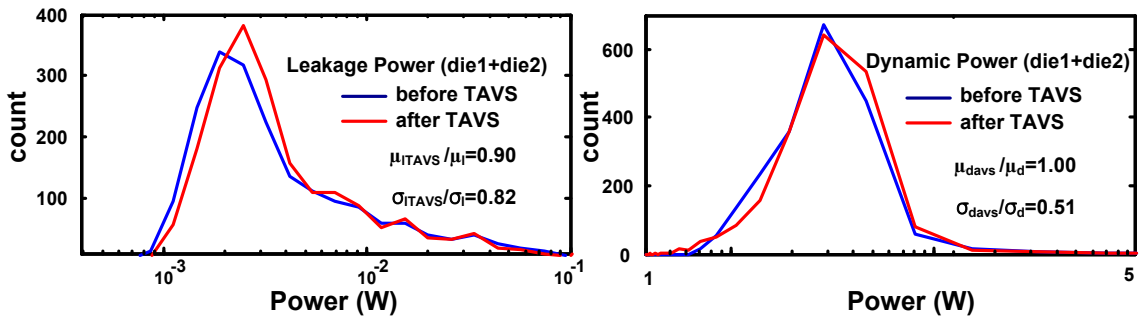
Figure 3.10: The impact of TAVS on leakage (left) and dynamic (right) power distribution.

Table 3.2: Analysis of power/area overhead.

Estimation of power and area overhead considering a 200K NAND2 gate design (100K in each tier) in 45nm nodes and different # of TSVs				
	Power Overhead		Area overhead	
# of TSVs	Minimum	Maximum	Minimum	Maximum
1000	0.11%	0.72%	1.14%	6.91%
2000	0.21%	1.44%	2.15%	13.024%
3000	0.32%	2.17%	3.04%	18.47%

3.4   Tier-adaptive-body-biasing for 3D ICs

The performance and the functionality of digital circuits depend on variations in logic delays and clock skews. The clock skew is defined as the difference between arrival times of the clock signal at different flip-flops. A higher clock skew worsens performance and/or robustness of a design. In 2D ICs, WID variations change the delay difference between various branches of the clock tree, leading to increased clock skews. The D2D variation changes the delay of the entire clock tree and, hence, does not affect the clock skew significantly. On the contrary, clock skews in 3D ICs are affected by both D2D and WID variations as both of them lead to within-chip variations.

The history of variation-aware 3D clock network design is short. Zhao et al. investigated the TSV random effects on clock skew uncertainties and analyzed the impact of WID and D2D process variations on 3D clock performance [34], [36]. The experiments indicated that a 3D clock network using multiple TSVs is able to decrease the clock skew variations by using fewer buffers and shorter interconnects. In addition, Xu et al. [38] proposed a statistical clock skew model for a regular 3D H-tree considering the WID and D2D variations in buffers. The use of clock TSV redundancy in a 3D clock network for fault-tolerant design has been explored [38].

This section analyzes the effects of D2D and WID variability on the clock skew in a 3D clock tree and presents tier-adaptive-body-biasing (TABB) – a post-silicon tuning method to reduce clock skew variations in 3D ICs. A system architecture is presented to independently sense the process variations in p-channel metal-oxide-semiconductor (pMOS) and n-channel metal-oxide-semiconductor (nMOS) devices using on-chip-delay-based sensors and adapt the body bias of the nMOS/pMOS devices of each tier to mitigate the impact of process variations. The effectiveness of the approach is demonstrated through statistical simulations considering D2D and WID variations on example 3D clock trees with different number of TSVs in a predictive 45nm node. The body bias tuning helps mitigate the effect of tier-to-tier process shifts and reduce clock

skew variations. The clock slew variation is also reduced as the separate body biasing for nMOS and pMOS transistors compensate the V_{TH}-skew between nMOS and pMOS transistors. Moreover, it is shown that TABB helps reduce variations in power of clock network and reduces the delay variability for logic paths. The application of ABB to reduce clock skew/slew, dynamic/static power, and logic path delay variations is a unique contribution of this research.

3.4.1 Analysis of 3D clock network under variations

3D clock trees are generated and used in the study using the synthesis method presented by Zhao et al. [34]. Given a set of clock nodes (=clock inputs of flip-flops) distributed into two dies and the clock source, the goal is to build a single tree that connects all the nodes to the source so that the skew and the total power consumption are minimized. TSVs are used to connect the nodes in different dies. The IBM r4 benchmark design that has 1000 clock nodes is used. The location and the input capacitance of clock nodes as well as the RC parasitic of clock wires, TSVs, and buffers are given as input parameters. The input capacitance of clock nodes in this tree varies from 30-60 fF. All design and simulations are performed considering a predictive 45nm technology [23]. The various design/simulation parameters for devices, wires, and TSVs are shown in Table 3.3. Three different types of 3D-clock networks were designed with 1 (Type1), 10 (Type2), and 100 (Type3) TSVs to observe the 3D clock skew variations according to D2D variation as illustrated in Figure 3.11(a), (b), and (c), respectively. Each die size is 10mm x 10mm. In the clock network Type1, each die has a complete clock network which is connected at a clock source through a single TSV. The clock network Type2 and Type3 have multiple TSVs and has a main clock network in die1 (a complete 2D network) and sub-clock networks in die2. The sub-clock networks in die2 are connected through the clock TSVs from the branches in the middle of the main clock network in die1. The

Type2 has 10 TSVs and Type3 has 100 TSVs, where the size of sub-clock networks in Type3 is much smaller than those in Type2. Hence, the network latencies of the 100 sub-clock networks in Type3 are much shorter than that of the 10 sub-clock networks in Type2; the clock latency in die2 is the highest for Type1.

Table 3.3: Parameters used in simulation.

Parameters	Description	
Process Model	45nm NCSU PTM model [23]	
Threshold Voltage (V_{TH})	nMOS: $V_{TH} = 0.471V$	pMOS: $V_{TH} = -0.423V$
Wire	r = 0.1 Ω/μm, c = 0.2 fF/μm	
TSV	RC π model : $R_{TSV} = 50$ mΩ, $C_{TSV} = 15fF$ ($C_{TOP} = 7.5fF$, $C_{BOTTOM} = 7.5fF$)	
[D2D σ,WID σ] (V_{TH}, wire, and TSV)	[5%, 15%], [10%, 10%], [15%, 5%]	
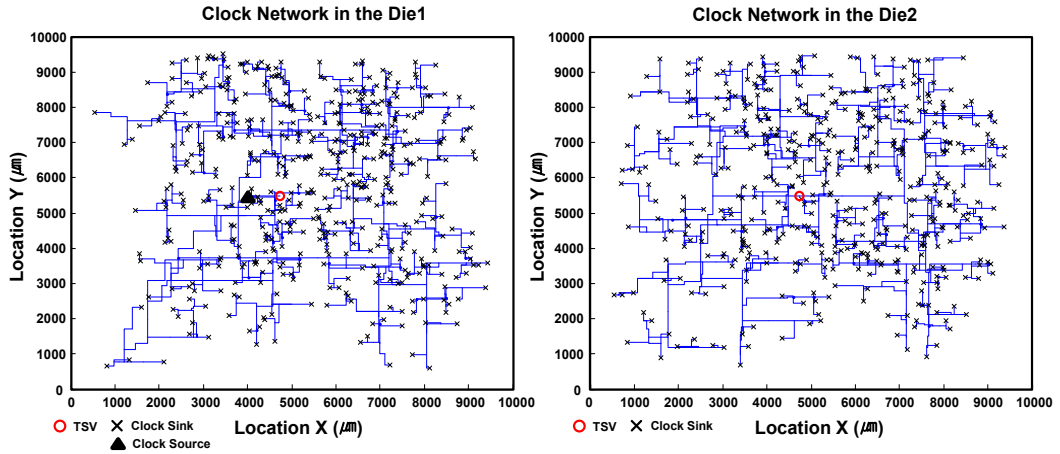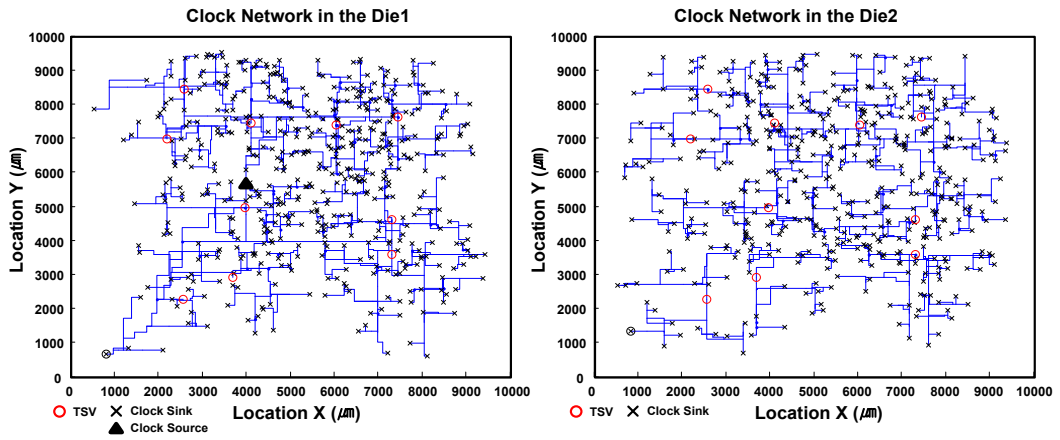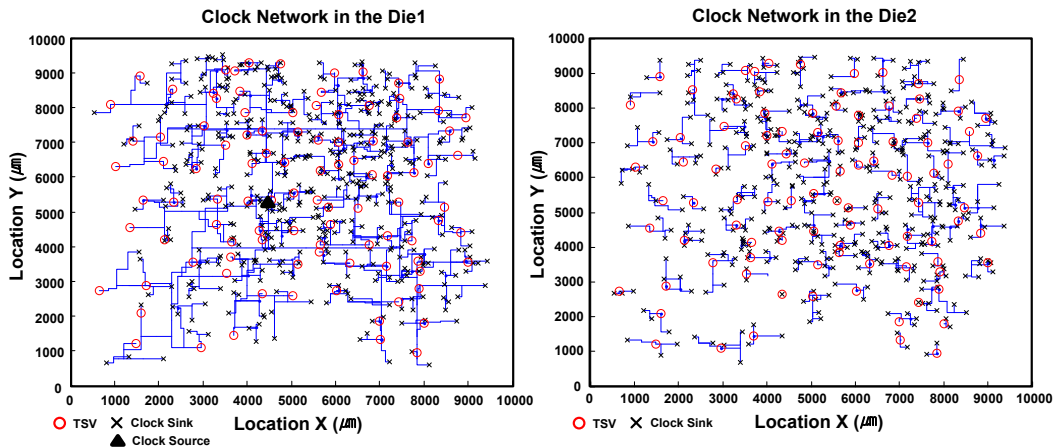
Figure 3.11: Three different types of 3D-clock networks: (a) Type1 (1 TSV); (b) Type2 (10 TSVs); (c) Type3 (100 TSVs).

The baseline values of clock skew, which are computed under no process variations, are shown in Figure 3.12. From Figure 3.12(a), it can be found that 2D skews are independent of each other in the clock network Type1. On the other hand, 2D skews are similar to each other in the clock network Type2 and Type3. Since the sub-clock networks in die2 of Type2 and Type3 are connected from the branches of the main clock network of die1, the clock skew performances of sub-clock networks in die2 are affected by the clock skew performances of the main clock network in die1.

(a)

(b)   (c)
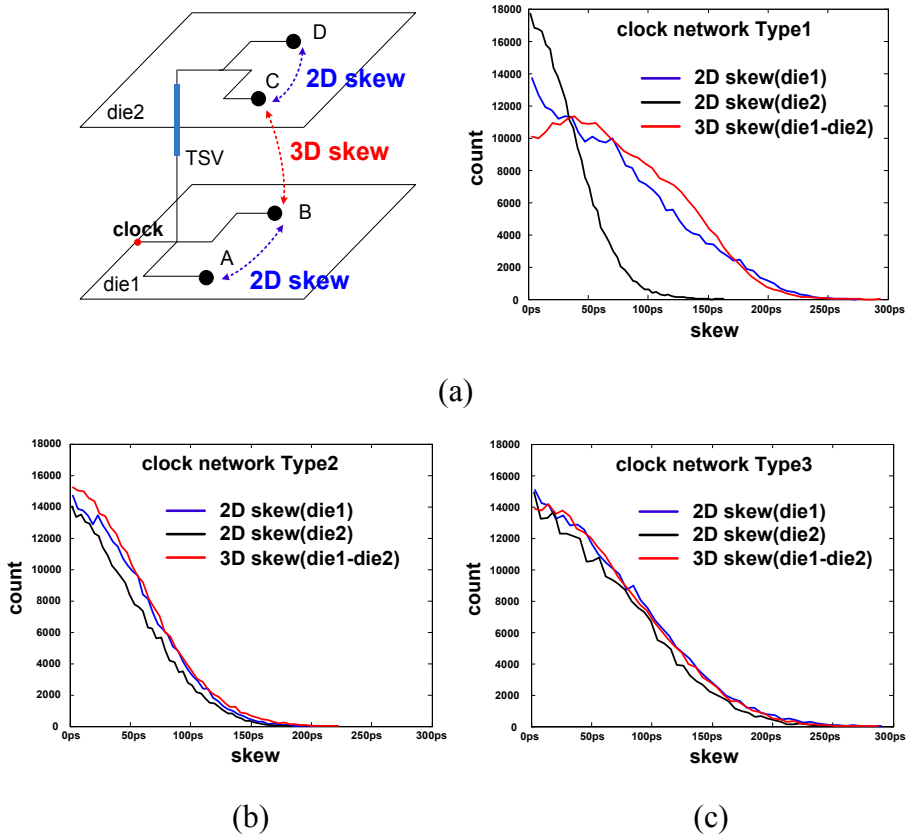
Figure 3.12: Skew histogram: clock skew base line without process variations of (a) the clock network Type1, (b) Type2, and (c) Type3.

The clock network latencies of various clock sinks in die1 and die2 are shown in Figure 3.13 (not considering variation), and a correlation coefficient (ρ) between the latencies of die1 and die2 is calculated. As expected from the preceding discussion, the

33

clock network Type1 has the lowest ρ (0.1727). On the other hand, in the clock network Type2 and Type3, the sub-clock networks share the common path with the main clock network. Hence, the correlation between skew of die1 and die2 is much higher. The correlation is the highest for Type3 as it shares the longest common paths with the main clock network in die1. From this result, it can be conjectured that the skew performance of the main clock network becomes more important as the number of clock TSVs increases.

(a)

(b)

(c)
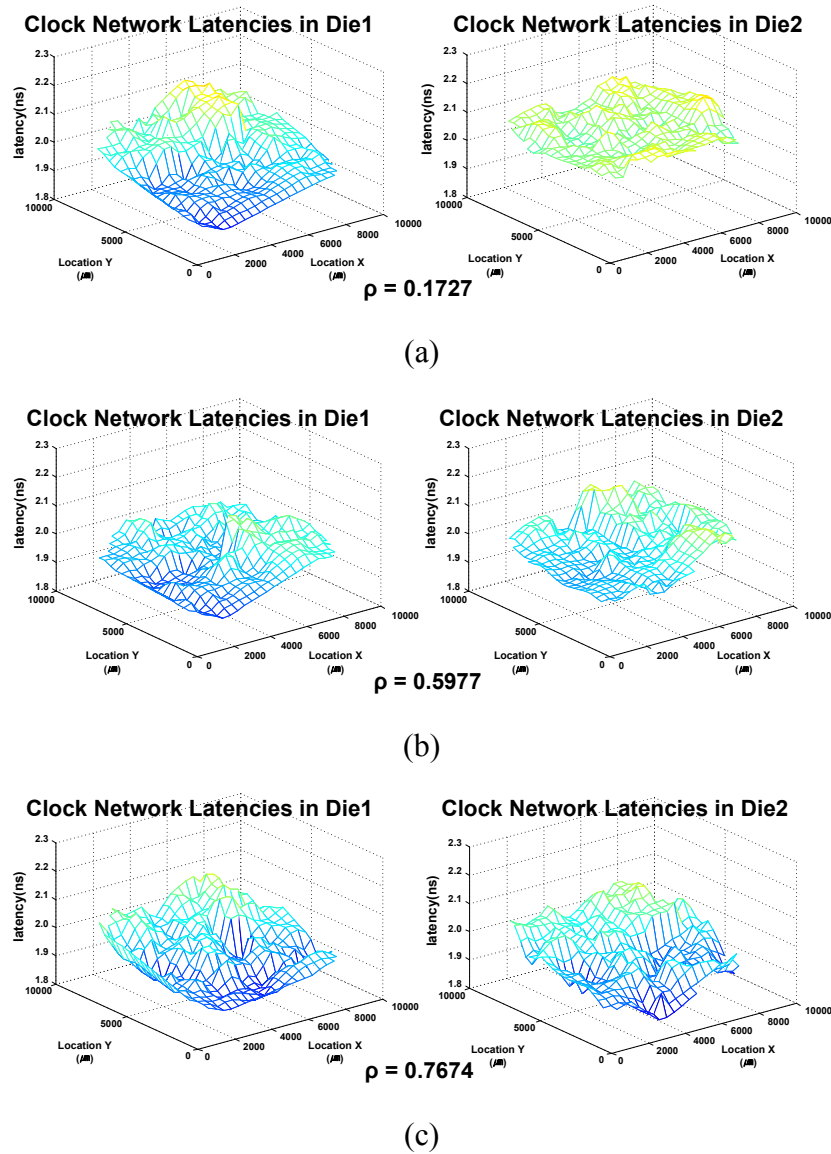
Figure 3.13: Correlation coefficient (ρ) between the latencies of the die1 and the die2 for (a) the clock network Type1, (b) Type2, and (c) Type3 not considering process variation.

Figure 3.14 illustrates the skew variability in the clock network Type1, Type2, and Type3 for different D2D and WID variability. In terms of 2D skew variation, all clock network types show the same trend. As the WID variation becomes stronger, 2D skew variation increases. From the results, it is concluded that WID variation is a dominant factor that decides the level of the 2D skew variation. The clock network Type1 showed extremely high 3D skew variation even under the low D2D variation (5% WID variation). Since the clock network Type1 in the die1 does not have a common path with the clock network in the die2, it showed the worst 3D skew variation. In addition, as the impact of D2D variation gets stronger, 3D clock skew variations of the clock network Type1 and Type2 increase. It implies that the D2D variation strongly impacts skew variations of the 3D clock network. However, as the number of clock TSVs increases (as the common clock path gets longer), the impact of D2D variation on skew variation becomes weaker as illustrated in Figure 3.14 – it is observed that 3D skew variation is maximum for Type1 and minimum for Type3 clock networks. As the impact of D2D variation decreases, the impact of the WID variation on 3D skew becomes observable. For example, the variation in 3D skew and 2D skew are comparable for the clock network Type3 when the D2D variation is weak; as the D2D variation increases the 3D skew variation dominates the 2D skew variation. In summary, an excessive number of clock TSVs reduces 3D skew variations, at the expense of additional area overhead for TSVs and the test clock routing for separate die test. In addition, it could also cause yield problems due to the TSV yield. More number of TSVs could lead to a higher possibility of failure in the clock network. If the D2D variation can be compensated, possible performance loss can be minimized even with a low number of clock TSVs.
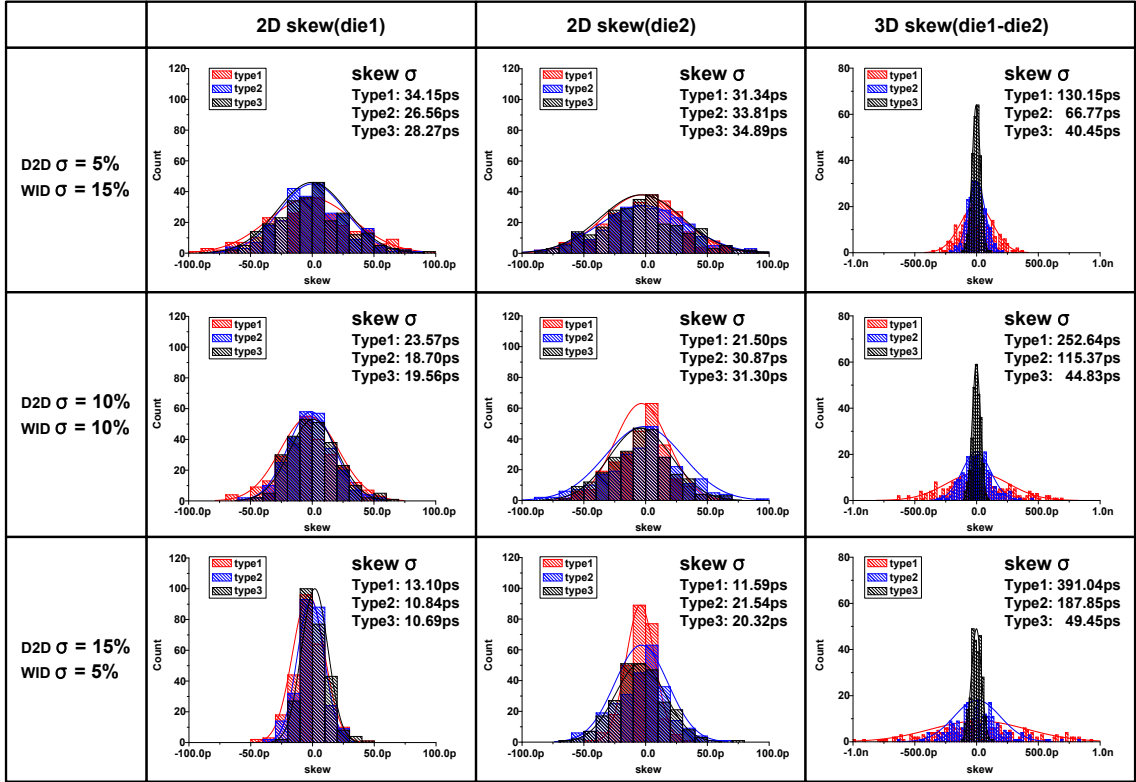
Figure 3.14: 2D and 3D skew distribution of specific points in the clock network according to different variations.

3.4.2 Tier-adaptive-body-biasing

Tier-adaptive-body-biasing (TABB) is proposed to compensate for the D2D variation and reduce 3D clock skew. The basic approach is to detect the global variation in the threshold voltage in each die. Forward body bias (FBB) is applied to a slow die to reduce V_{TH} and improve performance, while reverse body bias (FBB) is applied to increase V_{TH} to make a fast die slower. Independent body-bias levels are required to compensate for the V_{TH} shifts in nMOS and pMOS.

3.4.2.1 *System architecture*

The system architecture of TABB is shown in Figure 3.15. Each tier includes sensors to independently detect the threshold voltage shifts in nMOS and pMOS devices.

The variation sensors are enabled during power-up, and based on their outputs, a voltage regulator (body-bias regulator) changes the body voltages for nMOS and pMOS transistors in each tier separately. Note that all nMOS devices in a tier receive the same body bias and so do all pMOS devices in a tier. In this section, an off-chip power management IC is assumed to generate the body-bias voltages. The body bias range for nMOS and pMOS transistors is bounded within +0.3V and -0.3V, respectively. The limiting factor of FBB is the increased sub-threshold leakage current as well as the potential for forward-bias current through the body-to-source diode. The limiting factor of RBB is the increase in the short channel effect and the higher junction tunneling current in nanometer technologies. Further, two ABB options are explored. First, both FBB and RBB are considered. However, RBB is only possible when the voltage regulator can provide a negative voltage for nMOS transistors and a voltage higher than V_{DD} for pMOS transistors. Since generating a negative voltage or a voltage higher than V_{DD} is more complex (specifically, for on-chip generators), the option of using only FBB and nominal or Zero-Body-Bias (ZBB) is considered.
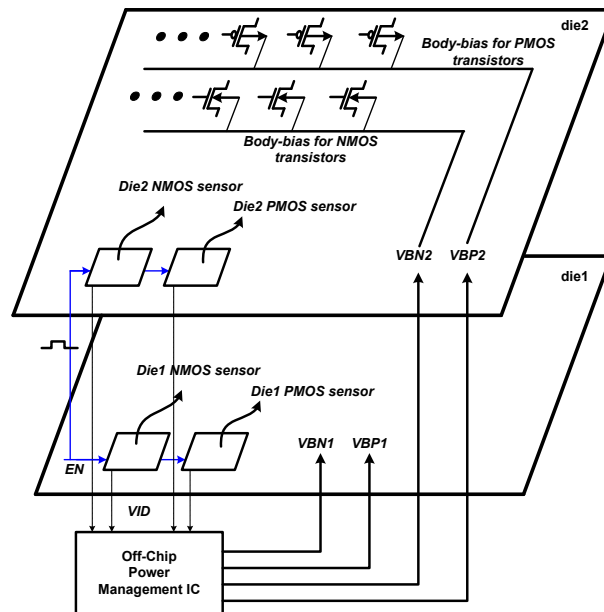
Figure 3.15: The tier-adaptive-body bias (TABB) system.

3.4.2.2 *D2D variation sensor*

A D2D variation sensor based on the principle of ring-oscillator (RO) type sensors is proposed in this research. The frequency of a ring oscillator changes due to process variations, and this signature can be detected using a counter. A RO type sensor can be easily implemented with digital components. The outputs are also digital and hence, can be easily utilized in digital systems [42]-[47]. The effects of WID variations can be minimized by increasing the number of chains in the ring oscillator, which helps average out the random WID across the stages [27]. However, in the tier-adaptive-body-biasing, it is required to independently detect the D2D variation of nMOS and pMOS devices. Since the delay of a RO is affected almost equally by nMOS and pMOS transistors, it is difficult to determine V_{th} shifts in nMOS and pMOS devices separately. This could result in an incorrect assignment of nMOS and pMOS body-biases, resulting in a reduced effectiveness. Further, in a clock network, a larger difference between the effective strengths of nMOS and pMOS devices can worsen the clock slew rate. Iizuka et al. have proposed an effective all-digital method to measure the performance variation of nMOS and pMOS devices separately by counting the number of pulses vanishing to 0 or 1 in a buffer ring [47], [48]. However, this method requires additional calculation process to solve equations for obtaining the final results. The method proposed by Zhang [49] for characterizing rising and falling time of standard cells includes analog circuits and complex measurement procedure.

In this section, the RO type D2D sensor is modified to sense the delay variation of nMOS and pMOS transistors separately without post calculation process, complex detection process or sophisticated analog circuits (Figure 3.16). The nMOS variation sensor is composed of the inverters with a pull-down network with stacked long-channel nMOS (Wn/Ln) transistors and a pull-up network with a single pMOS transistor (Wp0/Lp0). When the enable signal (EN) is high, the nMOS variation sensor oscillates with a frequency that is a strong function of the speed of nMOS transistors. This is

because due to the higher stack height, the fall time through the pull-down network is more dominant than the rising time. For the pMOS variation sensor, the inverter is composed of a pull-up network with stacked long-channel pMOS (W_p/L_p) transistors and a pull-down network with a single nMOS transistor (W_{n0}/L_{n0}). In this case, the rising time through the pull-up network is higher, and hence, the pMOS variation dominates the frequency.
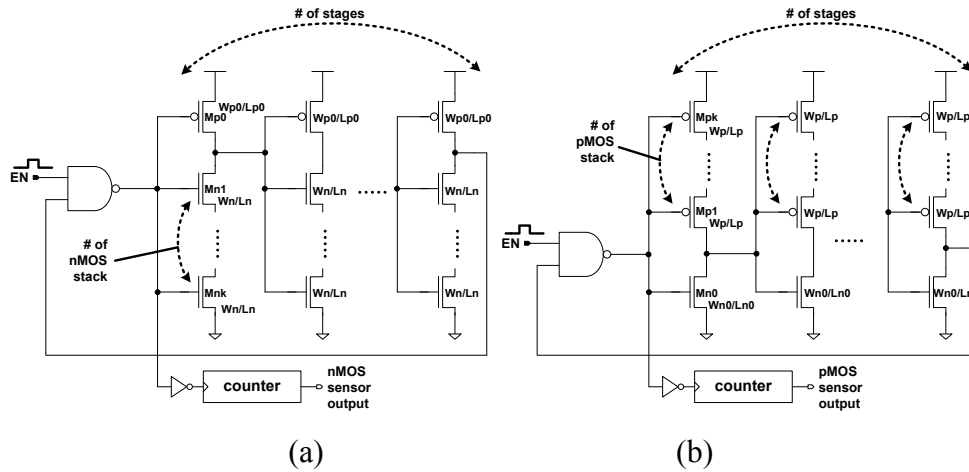
Figure 3.16: The modified RO-based (a) nMOS and (b) pMOS variation sensors.

Figure 3.17(a) shows the correlation between the nMOS speed and the sensor output, which increases with an increase in the nMOS channel length and the stack height. As shown in Figure 3.17(c) for the nMOS sensor, at A, the measured correlation factor was 0.280 with a short channel length (50nm) and one transistor stack. At B, with a long channel length (250nm) and 2-transistor nMOS stack the correlation factor increases to 0.915. Likewise, Figure 3.17(b) shows that a higher channel length and stack height of pMOS transistors increases the correlation between the pMOS process corner and the sensor output. From A to B in Figure 3.17(b), the correlation factor increases from 0.69 to 0.918. The correlation factor can be further increased by increasing the number of stages. Next, the size of pull-up pMOS in the nMOS variability sensor and the size of the pull-

down nMOS in the pMOS variability sensor are optimized to improve the correlation factor. For the nMOS variation sensor, if the pMOS transistor is too small, the pull-up delay becomes high. Thus, the pMOS speed introduces noise at the sensor output. On the other hand, when the size of the pMOS transistor is too large, the contention between pull-down and pull-up network becomes high. This also degrades the sensitivity of the total delay to nMOS process corner. A similar explanation holds for the pMOS variation sensor.

(a)   (b)

(c)
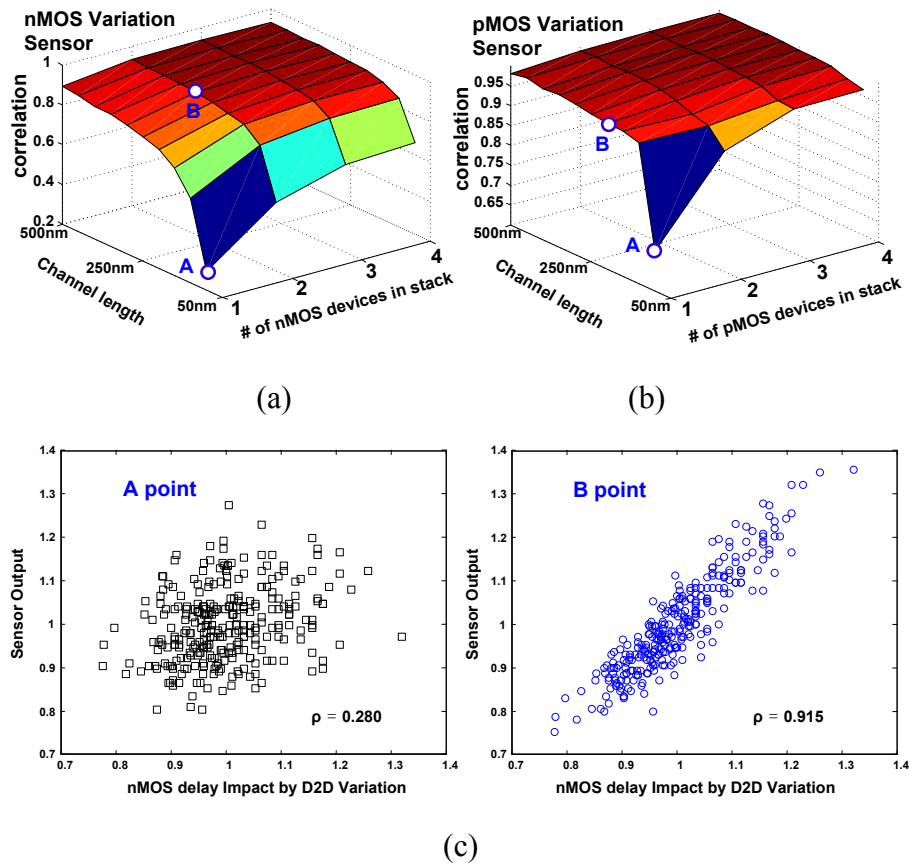
Figure 3.17: The correlation between the normalized nMOS or pMOS delay impacted by D2D variation and the normalized output of (a) the nMOS sensor and (b) the pMOS sensor according to the channel length size and the transistor stack; and (c) the detail correlation analysis for nMOS sensor at points A and B.

3.4.3 Simulation results

This section presents statistical simulation results to demonstrate the effectiveness of TABB. Monte-Carlo (MC) simulations were conducted for the clock network Type1, Type2, and Type3. The simulations also include 3 different combinations of D2D variations and WID variations: 1) when [D2D σ,WID σ] are [5%, 15%], it indicates a process of higher WID variations than D2D variations; 2) when [D2D σ,WID σ] are [10%, 10%], it implies a process with equal WID variations and D2D variations; and 3) when [D2D σ,WID σ] are [15%, 5%], it indicates a process of higher D2D variations than WID variations. For each MC simulation point, nMOS and pMOS variation sensors generate digital codes for the global nMOS and pMOS process corners. The body-bias levels for each tier are selected accordingly. Figure 3.18 shows a summary of the outputs of pMOS and nMOS variation sensors for the case of 15% WID variation and 5% D2D variation.

(a)

(b)
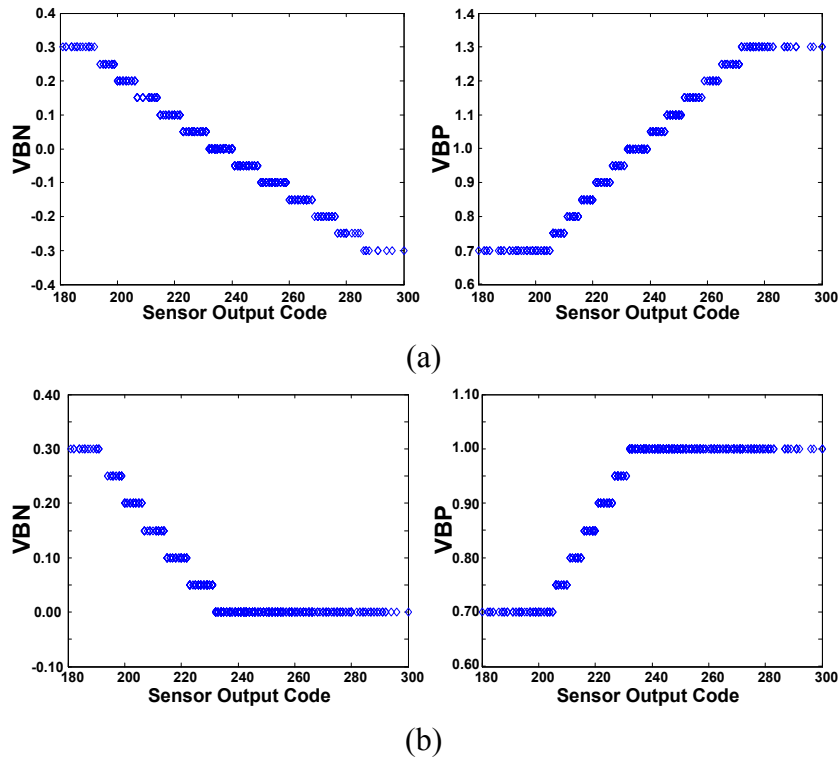
Figure 3.18: The body-bias assignments according to the sensor outputs of the pMOS and the nMOS variation sensors considering 15% WID variation and 5% D2D variation with 50mV resolution with (a) FBB/RBB and (b) FBB/ZBB.

The scenarios of (i) both FBB and RBB application (Figure 3.18(a)), and (ii) only FBB and ZBB applications (Figure 3.18(b)) are considered. According to the sensor outputs, different body biases are applied with 50mV resolution. Note that this resolution is well-within the capabilities of common voltage regulators (e.g., 6mV~12mV resolution [25]). Figure 3.19 shows the histogram of body bias assignments of die1 and die2 considering FBB/RBB (in Figure 3.19(a)) and FBB/ZBB (in Figure 3.19(b)) for the above example.
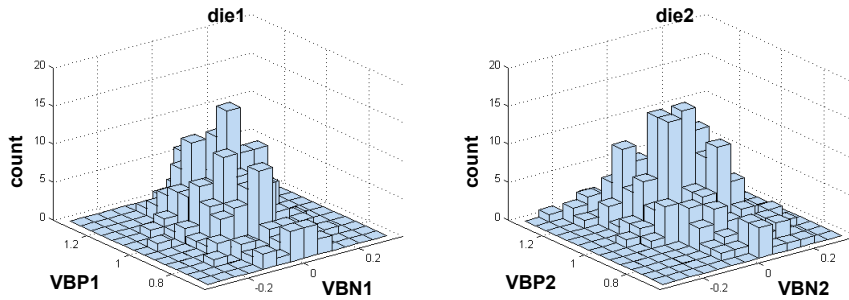
(a)
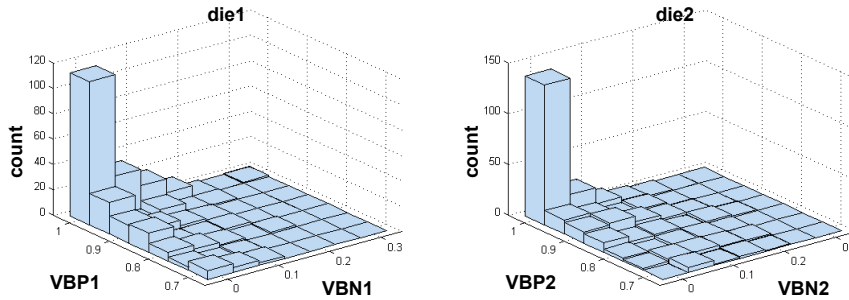
(b)

Figure 3.19: The histogram of the body bias assignments of the die1 and the die2 considering (a) FBB/RBB and (b) FBB/ZBB with 15% WID and 5% D2D variation.

3.4.3.1   *Effect of TABB on the clock skew variation*

With different body biasing conditions (without TABB, TABB with FBB/RBB, or TABB with FBB/ZBB), The trends of the mean, max, and standard deviation (σ) of clock skew in the clock networks are observed while changing D2D σ and WID σ. Observations for the clock network Type1, Type2, and Type3, are summarized in Figure 3.20, Figure 3.21, and Figure 3.22, respectively.

3.4.3.1.1 Effect of TABB on 2D skew

Higher WID variation increases the variability in 2D skew. However, even without any TABB, the effect is generally weak. Note that the impact of WID variations on 2D clock skew can be further reduced if the size of clock driver transistor increases. Generally, the buffers in clock network are designed with transistors that are larger than minimum-sized. When TABB is applied with FBB/RBB, it is observed that a marginal reduction in the mean skew, but comparably larger reduction in the standard deviation in skew and the maximum skew. TABB is more effective in reducing the mean, the standard deviation, and the maximum 2D skew when the D2D variation becomes higher. This is because the effect of the WID variation is more severe with worse global V_{TH} corners, and D2D variation compensation with TABB helps reduce 2D skew variations. Further, it is observed that TABB with only FBB gives marginally better benefits for 2D skew than TABB with FBB/RBB. This is because the effect of the WID variation on 2D skew is stronger for slow (high V_{TH}) dies (slow dies have higher delay sensitivity than fast dies). Since FBB compensates for variations in slow dies, FBB can be more effective in reducing 2D skew σ.

3.4.3.1.2 Effect of TABB on 3D skew

Without TABB, the D2D variation strongly affects 3D skew. A higher D2D variation results in a significant increase in the mean, the standard deviation, and the

maximum skew. As TABB reduces the D2D variation, it helps reduce the mean, the maximum value, and the standard deviation of 3D skew significantly. As expected, the effectiveness of TABB is stronger when the D2D variation is larger. TABB with FBB/RBB is more effective in reducing 3D skew compared with TABB with only FBB. This is because using both FBB and RBB results in a better compensation of the D2D variation than FBB alone. The advantage of using both FBB/RBB is more pronounced under higher D2D variations. However, this observation is reversed when the maximum 3D skew of clock network Type3 is considered [Figure 3.22(c)]. The reason is discussed in the next section.

3.4.3.1.3 Effect of TABB on different types of clock network

TABB shows a consistent effectiveness for different types of clock networks. Different clock networks showed similar results for 2D skew performance. As explained earlier, the characteristics of 2D skew in die1 and die2 are very different for the clock network Type1. TABB has a similar impact on 2D skew for both dies in Type1. For the clock network Type1, 3D skew variations due to D2D variations dominate 2D skew variations in each die. TABB with RBB/FBB significantly reduces 3D skew variations, and hence the overall skew variations in the network Type1. Due to this factor, TABB is most effective for the clock network Type1, which has only one TSV. As the number of TSVs in the clock network increases, however, the effectiveness of TABB reduces and the least impact is observed for the clock network Type3 (100 TSVs). This is because in the network Type3, the sub networks in the die2 have the longest common path with the main clock network in the die1. This causes the clock skews in the two dies to become more and more correlated and primarily determined by the skew variations in the main clock network in the die1. Therefore, the effectiveness of TABB reduces as the adaptive body biasing for the die1 only becomes important. It is also observed that variations in 2D skew and 3D skew become comparable. For the clock network Type3, FBB/ZBB

44

achieved higher reduction in skew variations. Since the clock network Type3 has small sub-networks in the die2 (the clock sub-networks in the die2 have the maximum shared clock path with the main clock network in the die1), it is affected less significantly by D2D variations than the clock network Type1 and Type2. As the D2D variation impact gets weaker, the WID variation shows a stronger impact on skew performance. Thus, FBB/ZBB could achieve a higher gain than FBB/RBB since making path delay shorter help reduce delay variation. In summary, FBB/RBB reduces skew variations more when the skew variation is a strong function of the D2D variation. On the other hand, FBB/ZBB achieves a higher gain if the clock skew is impacted more by the WID variation.
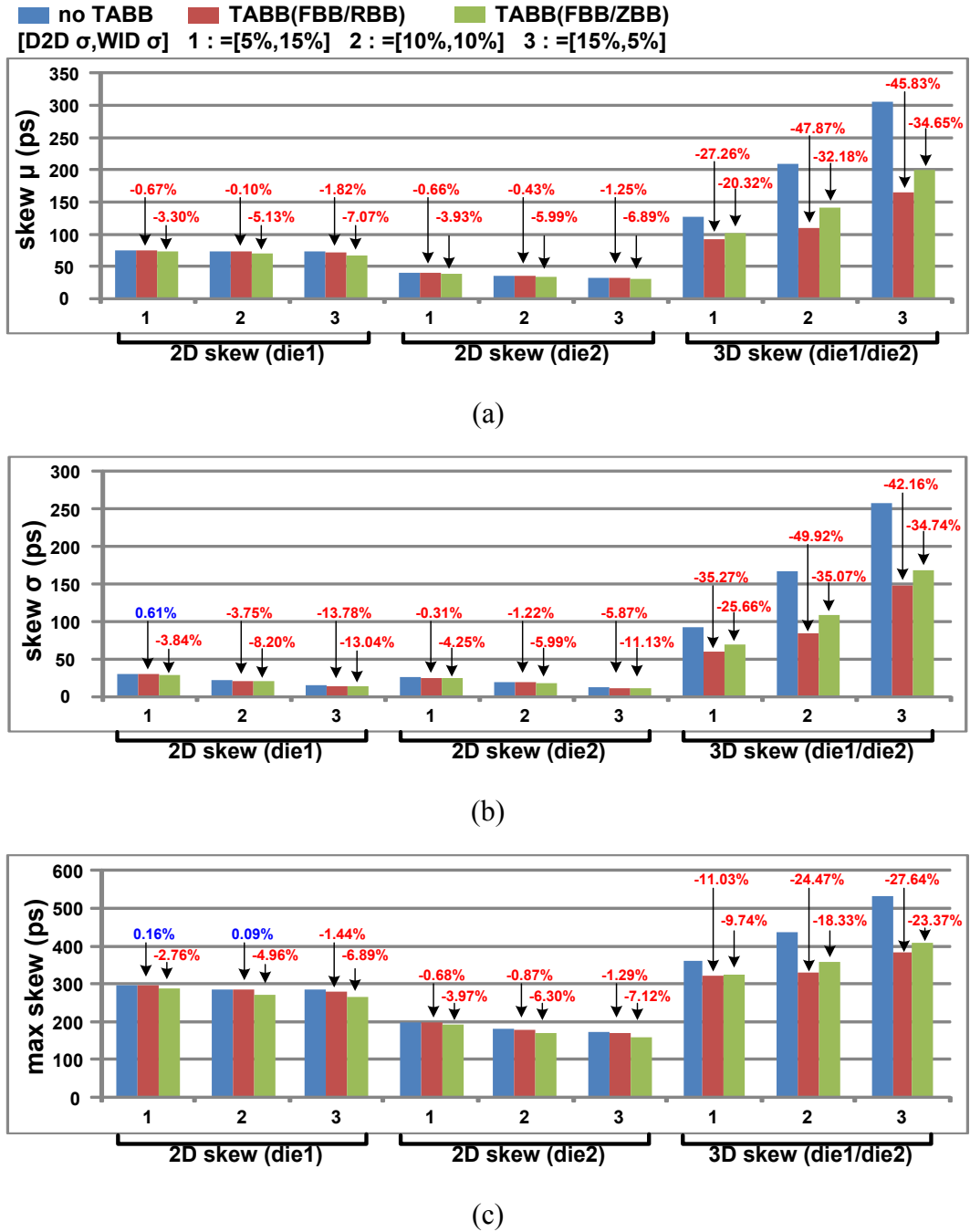
Figure 3.20: Results of TABB on the clock network Type1 considering D2D and WID variations: (a) mean skew; (b) skew variation; (c) max skew.
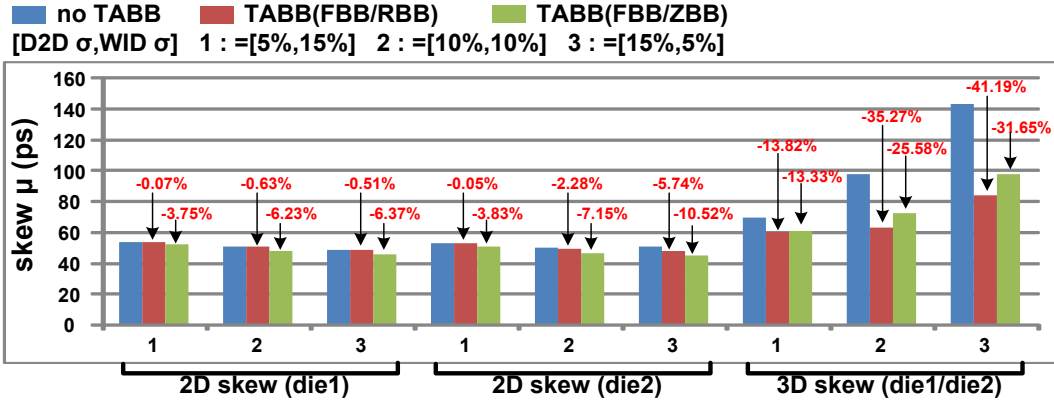
(a)
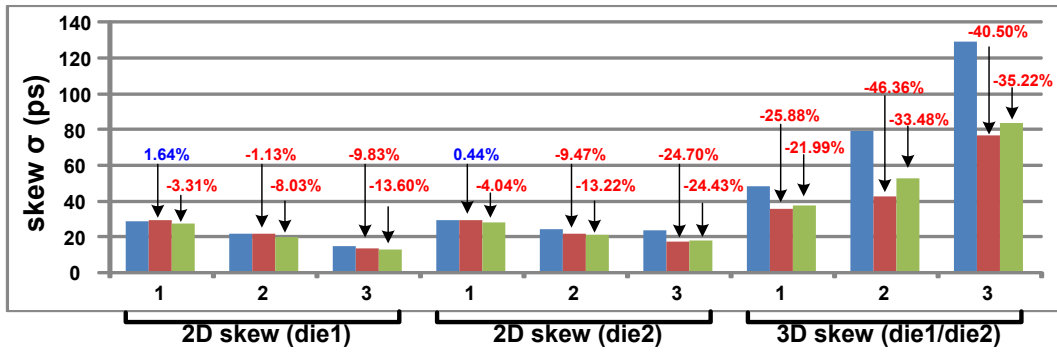
(b)
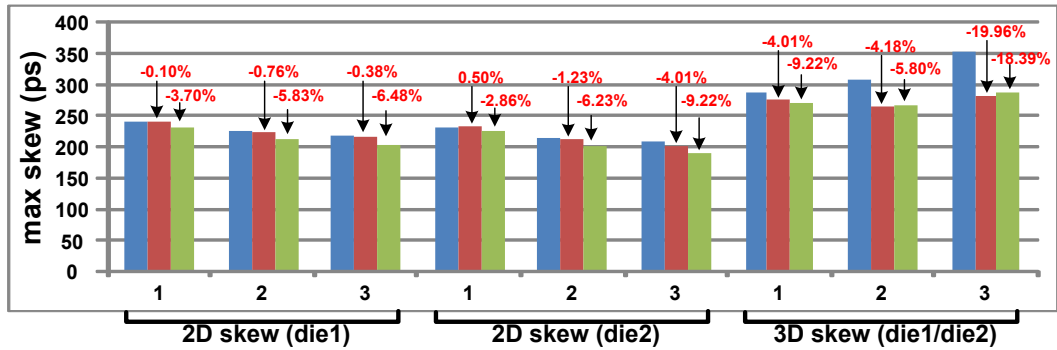
(c)

Figure 3.21: Results of TABB on the clock network Type2 considering D2D and WID variations: (a) mean skew; (b) skew variation; (c) max skew.
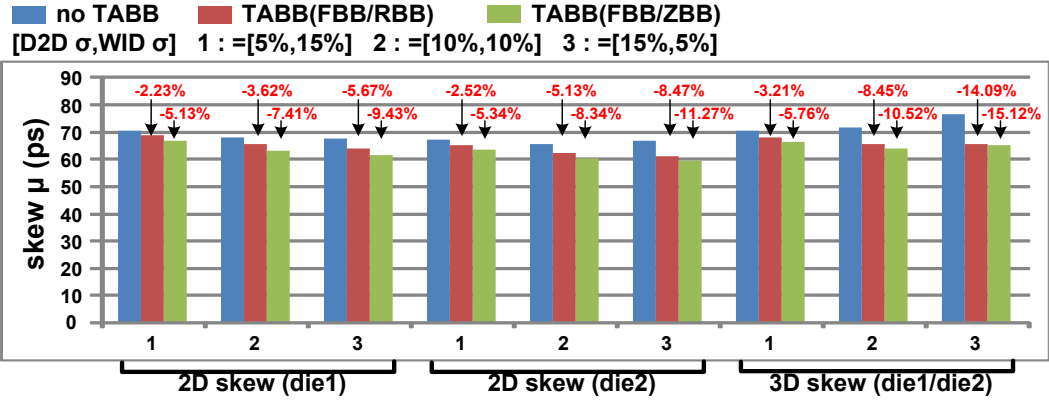
(a)
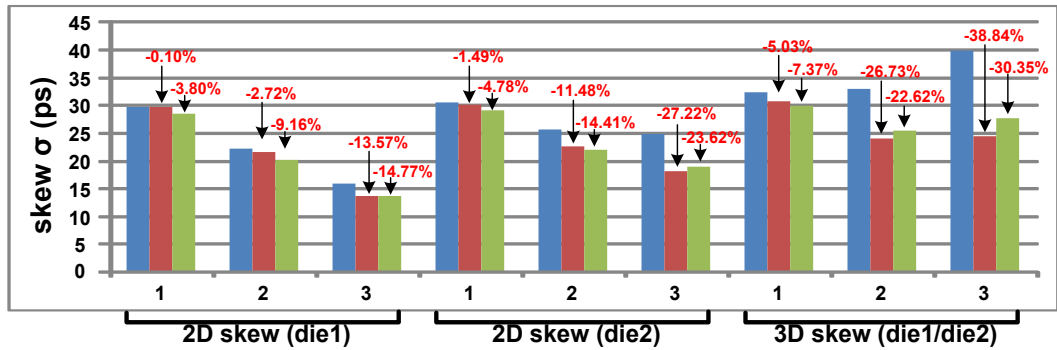
(b)
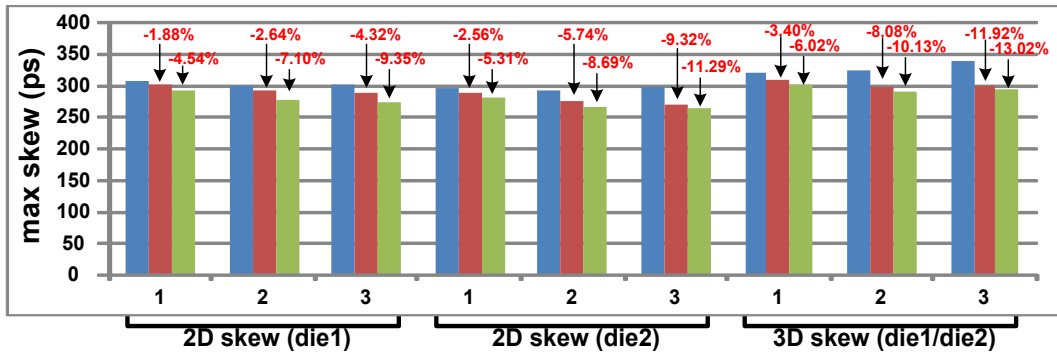
(c)

Figure 3.22: Results of TABB on the clock network Type3 considering D2D and WID variations: (a) mean skew; (b) skew variation; (c) max skew.

3.4.3.1.4 Effect of TABB on clock-slew rate

The effect of TABB on the variability in clock slew rate is studied. Figure 3.23(a) shows the clock slew rate according to different threshold voltage variations (ΔV_{THN} and ΔV_{THP}) of nMOS and pMOS transistors. It can be observed that there exist significant variations in the clock slew rate depending on the process shifts, even when the opposite V_{TH} shifts in pMOS and nMOS variations result in similar clock network latency (i.e., minimal skew). As shown in Figure 3.23(b)-(c), FBB/RBB or FBB/ZBB can effectively reduce the variations in the clock slew rate. It implies that applying separate body bias to nMOS and pMOS transistors helps better compensate variations for circuit parameter like clock slew rate, which are sensitive to V_{TH}-skew. Reducing the clock slew rate variation is important as slew can significantly impact the timing characteristics (i.e., setup time and hold time) of flip-flops.

$$\qquad\text{(a)}\qquad\qquad\qquad\qquad\text{(b)}\qquad\qquad\qquad\qquad\text{(c)}$$
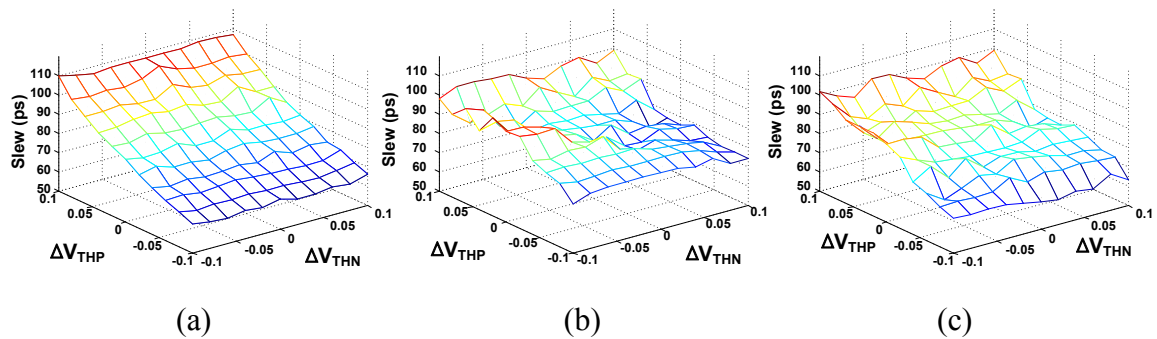
Figure 3.23: (a) Clock slew rate without TABB; (b) clock slew rate with FBB/RBB; (c) clock slew rate with FBB/ZBB according to V_{THN} and V_{THP} skew.

3.4.3.2 *Effect of TABB on overall performance*

The results in the previous sections show that TABB reduces the mean, the standard deviation, and maximum values of 2D and 3D skew under D2D and WID variations. However, as the body of all devices in clock buffers and logic gates are shared, TABB also affects delays of data paths. This is particularly true for nMOS devices

(assuming non-triple well process). Hence, it is needed to consider the impact of TABB on logic paths as well. This research evaluates the effect of TABB on two 2D data paths (the whole path is only in a die) and one 3D data path (the data path occupies two dies and uses 5 TSVs) of the 3D design. For data path, the absolute delay is important. Thus, D2D variation increases the delay variation of both 2D and 3D logic paths (Figure 3.24).

(a)

(b)
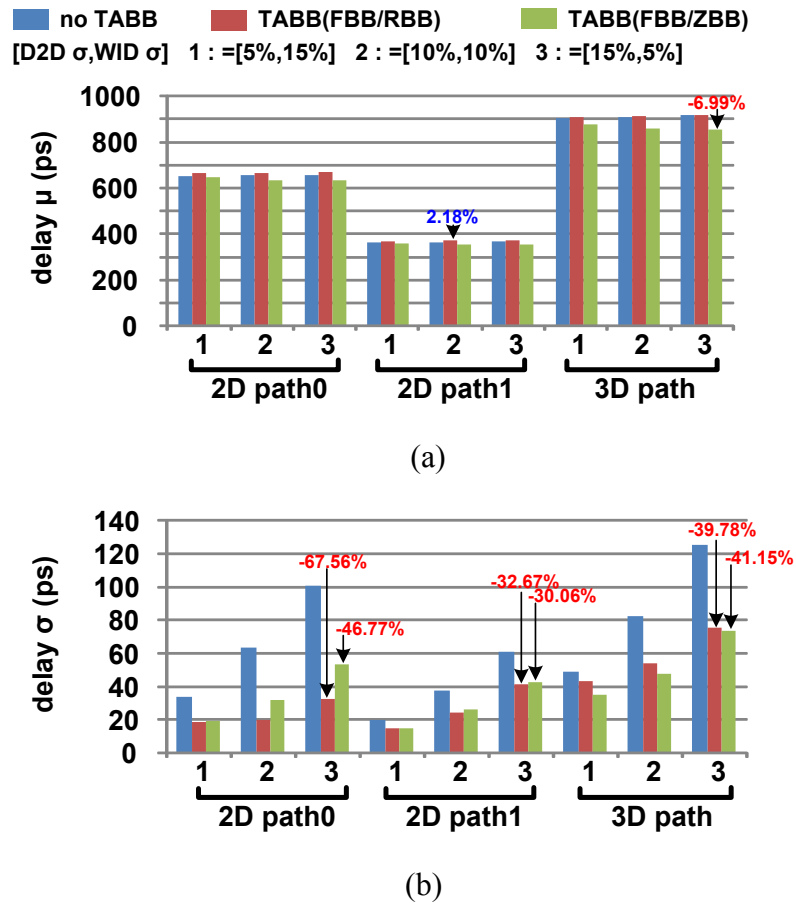
Figure 3.24: Results of TABB (FBB/RBB or FBB/ZBB) of the data paths (two 2D paths and one 3D path) according to D2D and WID variations: (a) mean delay; (b) delay variation.

Further, it is observed that the delay σ/μ of 3D path was smaller than 2D paths. This is because the independent D2D variations of two dies can partially offset each other, thereby reducing the overall delay variations [27]. TABB with FBB/RBB significantly reduces delay variation but has a marginal impact on the mean delay. The reduction in the

50

delay spread is less when TABB with only FBB is considered. Both 2D and 3D data paths experience a significant reduction in delay variation with TABB. In summary, TABB reduces variability in both clock skews and logic path delays, thereby significantly reducing the chip-to-chip variability in the performance of 3D ICs.

3.4.3.3   *Impact of TABB on area and power of clock network*

In the TABB architecture, power overhead of the sensors can be neglected since nMOS and pMOS variation sensors are activated only once during an initial boot-up sequence. However, it is needed to carefully analyze the impact of TABB on the power overhead of clock and logic paths. In case of FBB/ZBB, since FBB/ZBB causes slow logic gates to switch faster, it could help reduce short circuit current, which occurs when both the pMOS transistor and the nMOS transistor are on. A faster transition reduces the time when the pMOS and the nMOS transistors are both on. On the other hand, FBB increases the sub-threshold leakage current as well as the potential for forward-bias current through the body-to-source diode. In overall, the mean power overhead with FBB/ZBB was 0.47% ~ 0.49% of the total clock network power. With RBB/FBB, the average power consumption was reduced by 1.45% for all clock network types as shown in Figure 3.25(a). Although FBB could increase the average power, RBB helps reduce the excessive leakage current. Thus, in case of the total power (dynamic and leakage power), RBB/FBB reduced the mean total power of clock networks slightly. The variation in total power, on the other hand, reduces significantly (~40.59%) if TABB with FBB/RBB is used. This is because FBB increases the total power for slow dies, and RBB decreases the total power for fast and leaky dies. Thus, FBB/RBB reduces the total power variation down to 40.59%. On the other hand, FBB/ZBB decreases the total power variation by 9.62% only. Since FBB/ZBB works only for slow dies while FBB/RBB works for both slow dies and fast dies, FBB/RBB reduces power variation more. Further, as the total

51

power variation is significantly affected by the D2D variation, the reduction is higher when the D2D variation is dominant.
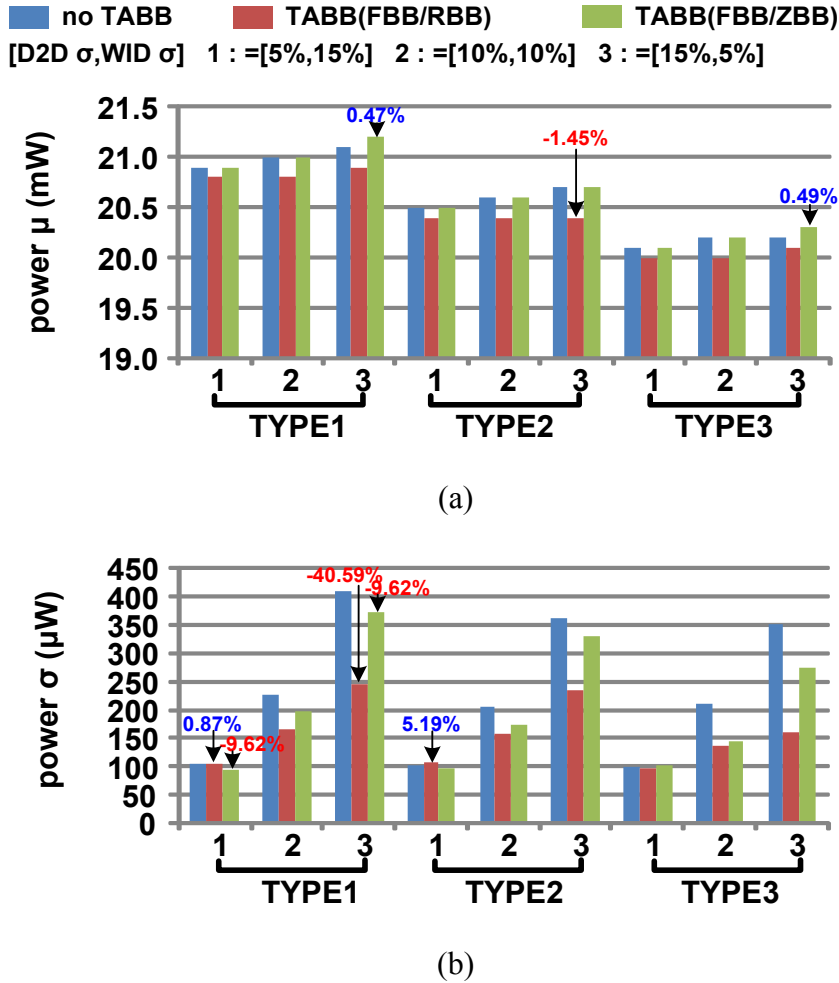
Figure 3.25: Results of TABB on the clock power considering D2D and WID variations: (a) mean power; (b) power variation.

The layout areas of nMOS and pMOS variation sensors are $178.8\mu m^2$ and $152.7\mu m^2$, respectively. The size of the sensors becomes negligible as the chip size gets bigger. Assuming a local sensor in a 1 mm^2 local area ($1000\mu m$ x $1000\mu m$), the area overhead from sensors becomes 0.033%. Because the current in the transistor body is at least two orders of magnitude smaller than the supply current, the cost of body bias routing is significantly less than the power grid [3]. Previous works have reported that the

area overhead of body bias routing is less than 2% of the total chip area. The area overhead was estimated from a test layout as shown in Figure 3.26. TAP cells for separate body contacts (substrate and n-well contacts) and routing was inserted at every 30μm. The feasible width of a TAP cell considering a 45nm DRC design rule is 0.35um, from which the area overhead can be estimated considering body contacts and routing. The estimated overhead is measured to be 1.17%.

The measured power consumptions of the nMOS and the pMOS sensors are 24.78μW and 26.93 μW, respectively at typical conditions (1.0V supply and 27ºC temperature). The overhead of the power consumption is 0.49% of the clock network Type1 power at 1.0V supply, 27ºC temperature, and 100MHz clock input. Considering logic power, this overhead will become much smaller. In addition, this power overhead can be negligible since the sensors operate only one time at the initial operation.
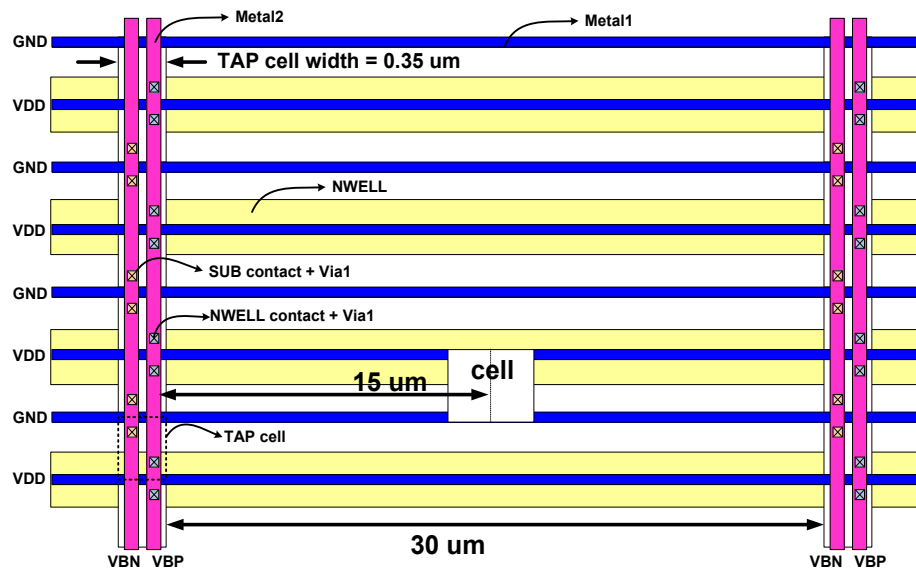
Figure 3.26: Layout overhead considering adaptive body biasing.

3.5   *Summary*

As the 3D technology matures, variation-tolerant design methodologies for 3D ICs will continue to be an important challenge. This research explores design methodologies for applying post-silicon tuning techniques to 3D ICs. This thesis presented TAVS as a methodology for post-silicon tuning to reduce delay variability of 3D ICs by tuning supply voltages of different tiers. The analysis results show that TAVS can improve the delay distribution of both 2D and 3D critical paths. TAVS can be beneficial for 3D ICs, which have separate functional blocks with different clock networks in each tier. Considering the case when a function is separated into different tiers with a one clock network, design methodologies for TABB are proposed. TABB helps perform post-silicon tuning of 3D clock trees to reduce variability. TABB can minimize skew and slew variability of 3D ICs by applying adaptive body biases to different tiers. The analysis results show that TABB can improve the system performance by reducing variability in clock skew and slew rate as well as logic path delay. TABB is effective in reducing the clock skew variability in all types of 3D clock network, but the effectiveness varies mainly based on the number of TSVs used. The maximum effectiveness of TABB is observed for clock networks designed with fewer TSVs.

CHAPTER 4

NON-DESIGN-INTRUSIVE APPROACH

4.1   Introduction

With increasing process and environmental variations in deep-submicron technologies, meeting performance specifications with limited power budget becomes a critical challenge [52]-[54]. The traditional worst-case corner based design introduces "safety margin" (e.g., operating at lower frequency or higher voltage) to tolerate variations. Having safety margin, although helps tolerate variations, leads to appreciable performance loss or power overhead [52]. This has led to investigations in adaptive design methods that compensate for detected [56]-[61]. An attractive approach is to utilize critical path replica circuits whose delays are strongly correlated with the critical path delays of the actual logic block [54]. Based on the delay of the replica circuits, operating condition, i.e., clock frequency and supply voltage, can be adaptively changed dynamically. The main purpose of this dynamic adaptation is to minimize the safety margin considering time-variant variations. To change the clock frequency or supply voltage adaptively depending on the dynamic environmental noises, detection of dynamic variations should precede the operating condition change. However, if any noise is detected, it implies that variation has already occurred. Thus, under dynamic variations, safety margin is required to make a circuit operate without any error. The extent of required safety margin is dependent on the speed of noise and the control time from the noise detection to the adaptation. As a result, fast detection and adaptation is the main focus for minimizing safety margin under dynamic variations.

This chapter presents two circuit techniques based on replica circuits for adaptation to time-dependent dynamic variations, such as supply voltage, temperature

variations, and aging effects. First, this chapter presents method to adapt to fast transient supply noises by modulating the system clock and the local clock. The proposed method enables direct clock modulation from the replica circuits and hence, allows within-a-cycle frequency modulation. As a result, it enables fast clock adaptation to fast transient noises and minimizes the safety margin for supply noises. Second, a methodology for generating a supply voltage level that is used as the reference voltage for on-chip regulators is presented. The voltage reference is the target level at which a circuit can operate without timing errors. The proposed adaptive voltage generator provides a cost-effective on-chip solution to minimize the voltage guard band under process variations, aging effects, and temperature variations. Additionally, the proposed work can generate a target voltage at a given target frequency. It implies that automated dynamic-voltage-frequency-scaling (DVFS) can be achieved considering dynamic variations.

4.2   Adaptive clock modulation

In digital systems, power supply noises (IR and Ldi/dt) affect logic path delays requiring careful characterization of the timing uncertainties [55]. Higher timing and/or voltage margins are required to ensure error free operation considering the worst-case power supply noise [56]. But higher margins reduce average performance and limit voltage scalability. Therefore, tolerance to transient supply noise is a major challenge to achieving higher performance at a low voltage while ensuring error-free operation [57]-[59].

Modulation of the clock frequency only during noise events can provide better average performance while preventing timing errors [58]-[61]. Kurd et al. have proposed to sense voltage droops and modulate the clock frequency by controlling the voltage-controlled oscillator (VCO) [58]. However, the response time is limited by the round-trip delay from noise sources to the VCO. Further, as the adaptation is performed at the clock

source only, the clock is not adapted against local droops. The alternative approaches employ clock stretching mechanisms in the clock buffers without changing the clock source to exploit clock-data compensation phenomenon [59]. Jiao et al. have proposed phase modulation in a VCO to effectively match the clock phase and the data path delay change [60]. However, if the clock source is not changed, stretching is followed by clock period contraction, which can have negative impact unless changes of the clock phase and the data path delay are matched. In addition, modulation is performed only in response to the first droop noise not DC and local noises since the modulation is coupled with global AC noises. In general, modulating the clock frequency by sensing the voltage droop is an indirect approach as the correlation between the critical path delay and the transient voltage droop is not accurately captured. Therefore, modulating the clock frequency using a delay sensor based on critical path replica circuits is more direct and accurate method to track the impact of noise on timing [61]. However, the delay through the sense-and-correct control loop makes it difficult to adapt to fast (cycle-by-cycle) local noise.

To address the preceding challenges, this research presents an all-digital adaptive clocking method to prevent timing errors under global/local supply noise. The proposed all-digital global modulator (GM) and local modulators (LM) *integrate the critical path replica within the modulator,* instead of using the replica as a sensor, to directly generate global/local clocks with periods determined by the replica delay (Figure 4.1). The GM modulates the input (PLL) clock to generate the system clock (CK_G) with a range of discrete frequencies; and the LM modulates CK_G in a limited but continuous frequency range to generate the local clock (CK_L). The replica based direct approach ensures the clock period accurately tracks delay variations in the critical path due to supply noise. The integration of the replica within the modulator reduces the delay of the sense-and-adapt loop facilitating adaptation to both fast and slow transient noise. The key features of the proposed approach are: (i) fast (within a cycle) adaptation of clock to protect

57

against dc and transient noise (1st, 2nd, and 3rd droops); and (ii) adaptation against both local (close to the critical path) and global (chip level) noise.
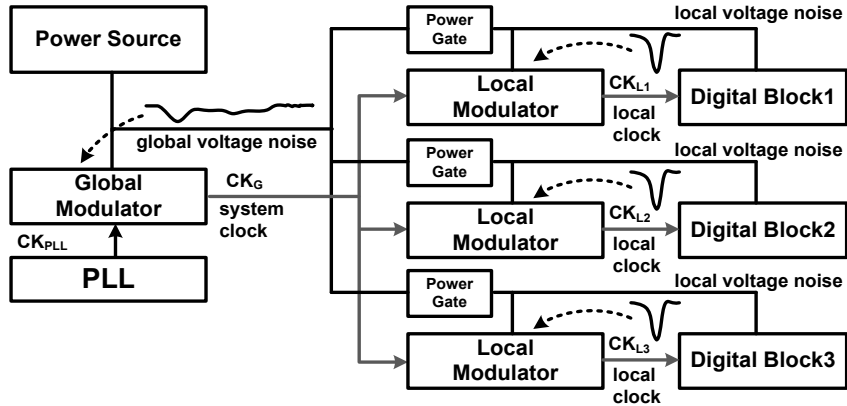
Figure 4.1: Overview of the proposed clock modulation approach.

4.2.1 Clock modulation methodology

4.2.1.1 *Global modulation*

The GM uses two identical replicas that are activated alternatively (Figure 4.2). The basic idea is to generate CK_G directly from the replica with a period (T_{CKG}) determined by the replica delay (T_p). The timing diagram of the operation is illustrated in Figure 4.3 with the key events marked with numbers (1 to 6). AR is set only after the delay (T_P) of one activated replica (S01 or S11 is set). (1) If AR is set and CK_{PLL} is low, EN is set to generate a clock pulse (CKS). (2) CKS pulse triggers rising edge of CK_G and, in turn, toggles S00 and S10 (de-activates one replica and activates the other replica). (3) This de-activation of one replica clears AR. The activated replica starts propagating the high signal. (4) S0h or S1h, the intermediate node of the replica, is set first after a propagation delay of T_H ($< T_P$). The rising edge of S0h or S1h generates a pulse (DP) which clears CK_G, i.e., the rising edge of S0h or S1h results in the falling edge of CK_G and determines the duty of CK_G. (5) After the replica delay (T_P), AR is set again and the

58

rising edge of CK_G is generated. Thus, the clock period (T_{CKG}) tracks Tp. (6) If T_P increases due to supply noise, T_{CKG} increases as well. The control granularity of T_{CKG} depends on the clock period of CK_{PLL} (T_{PLL}) as it defines the sampling time points for AR. A higher input clock frequency results in a finer grain control at the expense of increased power dissipation in the modulator. The duty of CK_G can be changed by programming the delay (T_{DT}) in DP path. T_P is also variable for compensating mismatches between the replica and the real critical path delay by changing the delay (T_{M1}) in AR path.
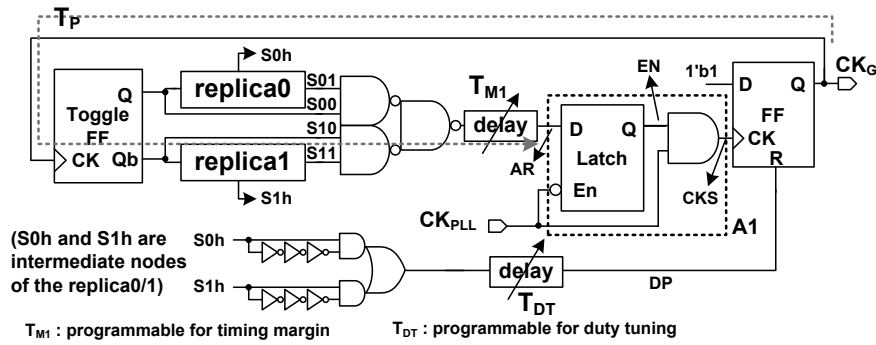
Figure 4.2: Block diagram of the global modulator.
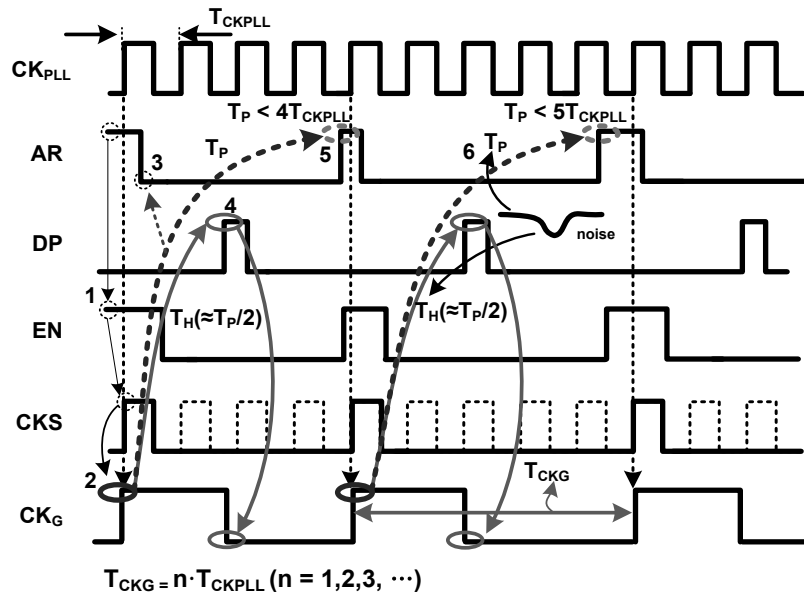
Figure 4.3: Timing diagram of the global modulator.

4.2.1.2 *Local modulation*

The basic structure of the LM is similar to the GM (Figure 4.4). The operation of the LM depends on the duty modulation window (T_{DM}). T_{DM} is the time difference between CK_G and CK_D. T_{DM} can be changed by programming the delay chain in CK_D path. If T_{DM} is 0 [clock gating mode or duty modulation (DM) off mode], the LM gates the input clock pulse when the increased replica delay is greater than the input clock period (Figure 4.5(a)). If T_{DM} is not 0 [duty modulation (DM) on mode], the local clock pulse (CK_L) is generated only when the critical path delay is smaller than $T_{CKG}+T_{DM}$ (Figure 4.5(b)). Otherwise, the input clock pulse (CK_G) is gated. However, if T_P is between T_{CKG} and $T_{CKG}+T_{DM}$, the clock duty is modulated and the effective clock period is changed. To prevent a false glitch at CK_L, the propagation delay from CK_L to AR reset (CK_G-to-CK_L delay, the toggle flip-flop delay, and-or gate delay, and the delay of the programmable margin) is designed to be higher than T_{DM}.
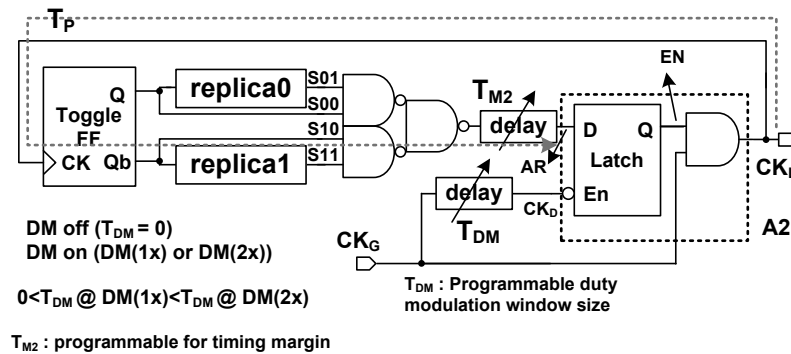
Figure 4.4: Block diagram of the local modulator.

DM off (Clock gating mode)

$T_P > T_{CKG}$

$T_{CKL} = T_{CKG}$ or $2 \cdot T_{CKG}$

(a)

DM on (Duty modulation mode)

$T_P < T_{CKG} + T_{DM}$

$T_P > T_{CKG} + T_{DM}$

$T_{CKL} \leq (T_{CKG} + T_{DM})$ or $T_{CKL} = 2 \cdot T_{CKG}$

(b)
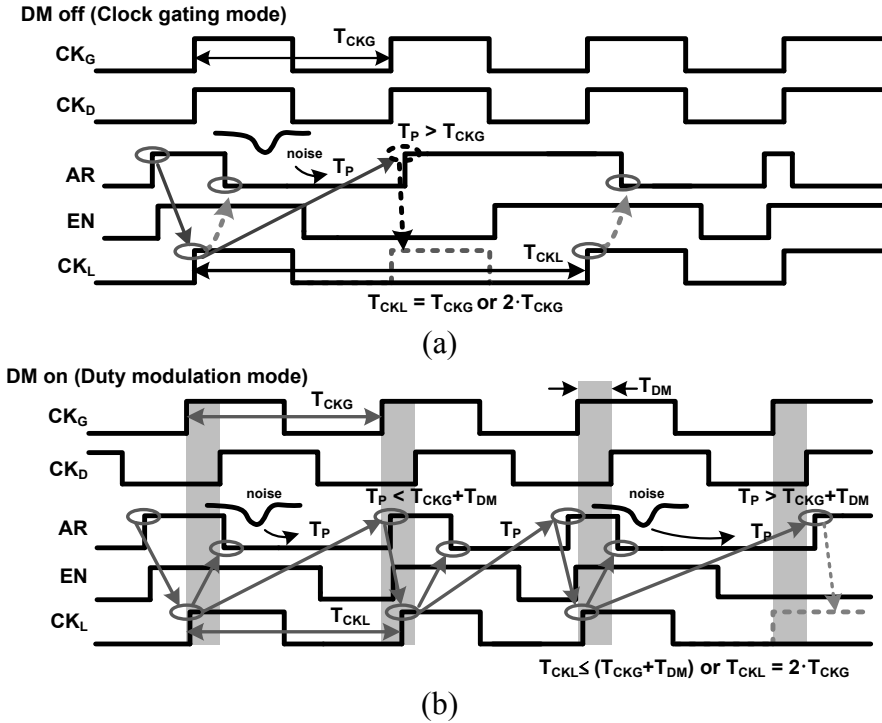
Figure 4.5: Timing diagram of the local modulator: (a) DM off and (b) DM on.

4.2.1.3 *Design considerations*

As T_P approaches $n \cdot T_{PLL}$ in the GM and $n \cdot T_{CKG}$ (DM off) or $n \cdot T_{CKG} + T_{DM}$ (DM on) in the LM, the latches used for clock gating circuit in modulators could have metastable condition. The metastability can incur timing variations in the rising edge of the output clock (CK_G and CK_L). Although it is impossible to eliminate metastability, the possibilities of metastable conditions are reduced by using Schmitt-trigger and sense-amplifier based latches, both of which have high gains, in the GM and the LM (Figure 4.6). The metastable point of the sense-amplifier is designed to be lower than the logic threshold of the Schmitt-trigger. Even if the metastability occurs in the sense-amplifier, the output of the Schmitt-trigger can filter out the signal lower than the logic threshold of the Schmitt-trigger. The intermediate level (near the metastable voltage) of clock is therefore unlikely to propagate through the clock network. Nonetheless, the rising edge of CK_G and CK_L can be delayed due to metastability in A1 and A2 when the critical path

delay is close to the generated clock period. This delay, although introduces jitters in the current cycle, effectively extends the current clock period which is beneficial for timing margin in data paths. The next clock period is also controlled to become higher than the replica delay in that period as the replica circuits are activated based on the current clock edge and the next rising edge of the clock is determined by the delay of that activated replica circuit. In summary, even if the current clock edge is delayed due to metastability, timing errors are prevented in both the current and next clock cycle. However, the clock edge uncertainty can lead to challenges in synchronizing different blocks operating with different LMs and require additional synchronizers.

Figure 4.6: Clock gating circuits (A1 and A2 block).

4.2.2 Test chip and measurements

A test chip is implemented in 130nm CMOS to validate the adaptive clocking scheme as shown in Figure 4.7. The design includes a voltage controlled oscillator (VCO), a serial peripheral interface (SPI), control registers, a frequency counter, an error counter, 5-stage test pipelines, and a noise injector. The noise injector is comprised of nMOS transistors, which draw instantaneous current from the power supply and incur

voltage noises in the supply when an enable pulse is applied as shown in Figure 4.7. The VCO generates CK_{PLL}, which is used for the input clock of the GM. The frequency of the VCO is controlled by the external VCO control voltage (V_{CTRL}). The output of the GM is used for the input clock of the LM. The LM generates the local clock for the test pipeline. The different modes, namely, DM(1X) and DM(2X), represent different duty modulation window (T_{DM}) and are determined by the programmable delay chain in CK_D path that indicates the delay between CK_G and CK_D. In this design, T_{DM} for DM(1X) corresponds to 6-inverter-chain delay and T_{DM} for DM(2X) corresponds to 10-inverter-chain delay for duty modulation. The performance of the test pipeline with clock modulation was measured utilizing the frequency counter while injecting supply noise at different injection frequencies.
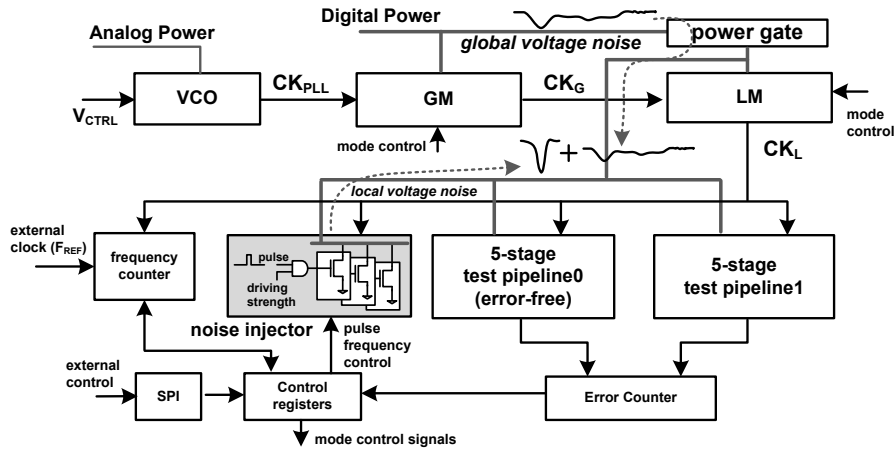
Figure 4.7: Block diagram of the implemented system.

4.2.2.1   *Effect of DC voltage variation*

Figure 4.8(a) shows the measured clock frequency generated by the GM in different supply voltages (LM was turned off) to observe the ability to adapt frequency with the DC voltage change. It can be observed that the GM automatically generates the output clock frequency at which the test pipeline can operate without timing errors over a

wide voltage range (0.74V~1.3V). Within the voltage range of the frequency transition i.e. when T_P is almost equal to $n \cdot T_{PLL}$, two different clock frequencies are observed [Figure 4.8(b)]. As shown in the frequency transition region in Figure 4.8(b) (zone marked A in Figure 4.8(a)), it is observed that small variation in T_P can make T_{CKG} either 10ns or 11ns. Since two different clock frequencies are found, the effective clock frequency is defined as: $F_{EFF} = 1/T_{EFF} = F_{REF}N_{CNT}$, where F_{REF} is the external input clock (100KHz) and N_{CNT} is the counter value of the frequency counter. Thus, F_{EFF} can be calculated in 0.1MHz resolution.

Figure 4.8(c) shows the measured effective clock frequency generated by the LM with GM off according to DC voltage change with the direct input clock (100MHz). When DM is off, two different frequencies (100MHz or 50MHz) are observed at the frequency transition region. When DM(1X) is on, the effective frequency slowly reduces to 50MHz as the supply voltage reduces. Although the replica circuit delay is higher than the input clock period, the LM with DM on modulates the clock period by reducing the clock duty within duty modulation window (T_{DM}). Since the rising clock edge is determined by the delay of replica circuits, the rising edge of the clock will keep delayed within the DM window. Eventually, the clock pulse will be gated. Because of this behavior, the measured effective clock frequency changed discretely like a step according to the number of the gated clock pulses. When DM(2X) is on, the effective frequency changed more slowly than DM(1X) mode.
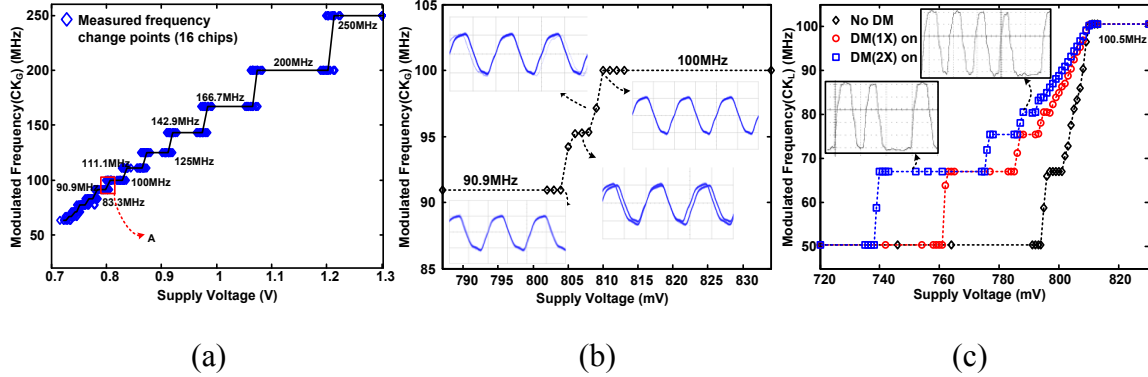
Figure 4.8: Measured frequency modulation results of the GM and the LM under DC voltage shift; (a) clock modulation of the GM; (b) the effective clock frequency of the GM at the frequency transition region; (c) the effective clock frequency of the LM at the frequency transition region.

The above observation is further clarified in Figure 4.9, which shows the characteristics of the duty modulated clock. Figure 4.9(a) shows waveforms of the duty modulated clock [DM(1X) mode] at voltages around the frequency transition region. At 812 mV supply, the output clock frequency is the same with the input clock frequency to the LM. As the supply voltage decreases further (~800mV), the clock frequency is modulated by modulating the clock duty. Reducing the voltage further (~790mV) eventually causes the AR signal to be set outside of the duty modulation window resulting in gating of a clock signal. The duty modulation amount is limited by T_{DM} and if the duty continues reducing in successive cycles eventually clock is gated as in Figure 4.9(a). If the voltage is reduced further (~784mV) clock gating becomes more frequent. The frequency characteristics of the duty modulated output clock are summarized in Figure 4.9(b). The 100MHz clock frequency can be observed around frequency transition region (790mV~810mV). Below 780mV, 100MHz frequency disappears and the duty modulated clock determines the maximum frequency. The minimum clock frequency is higher than 50MHz in the frequency transition region as the clock is gated after clock duty modulation as shown in Figure 4.9(a).

65

(a)   (b)
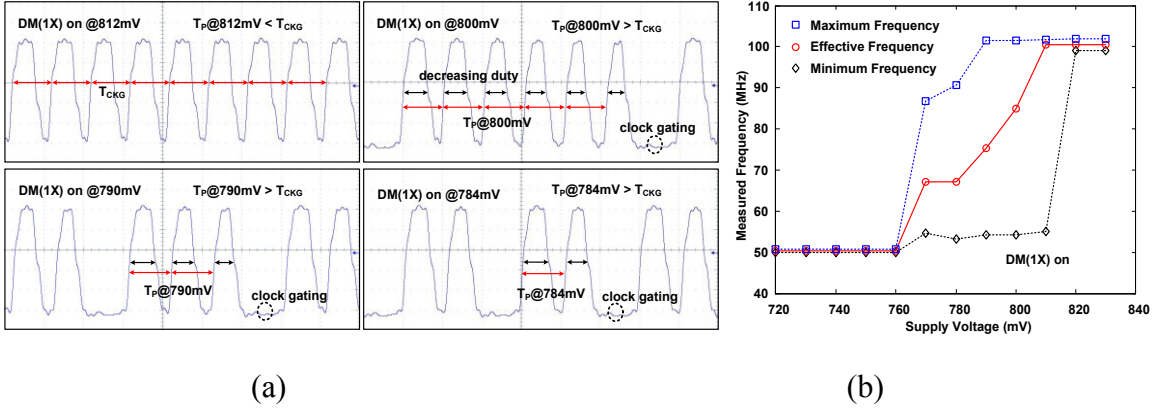
Figure 4.9: Characteristics of the duty modulated output clock of LM with DM(1X) on at low-operating voltage: (a) measured output waveforms of the LM with DM(1X) on near the frequency transition region and (b) The measured maximum/minimum frequency and the effective frequency.

4.2.2.2   *Effect of transient supply noise*

Figure 4.10 shows the measured clock and supply waveforms, which demonstrate operations of the GM and the LM under transient supply noise. Figure 4.10(a) shows the measured waveform of CK_L, which is modulated to 100MHz by the GM and the LM at 0.81V supply without noise injection. The effective frequency (F_{eff}) is calculated from the frequency counter value. Figure 4.10(b) shows the frequency modulation of the GM under transient noise. The output clock period is changed from 10ns to 11ns in the presence of the supply noise. The modulation results of the LM (DM off) is shown in Figure 4.10(c). With DM off, the LM modulates the output clock period from 10ns to 20ns. When both the GM and the LM (DM on) are on, frequency modulation effect by the GM and the duty modulation effect by the LM can be observed as shown in Figure 4.10(d). When DM is on, the duty modulation looks like increasing clock jitter, which is not random like normal jitter but controllable and correlated with the replica path delay variation. Since $T_{DM(2X)}$ is larger than $T_{DM(1X)}$, wider duty modulation window is observed at DM(2X) mode than at DM(1X) mode. The result of reduced clock duty with

66

controllable amount (duty modulation window) increases the clock period within a limited range.
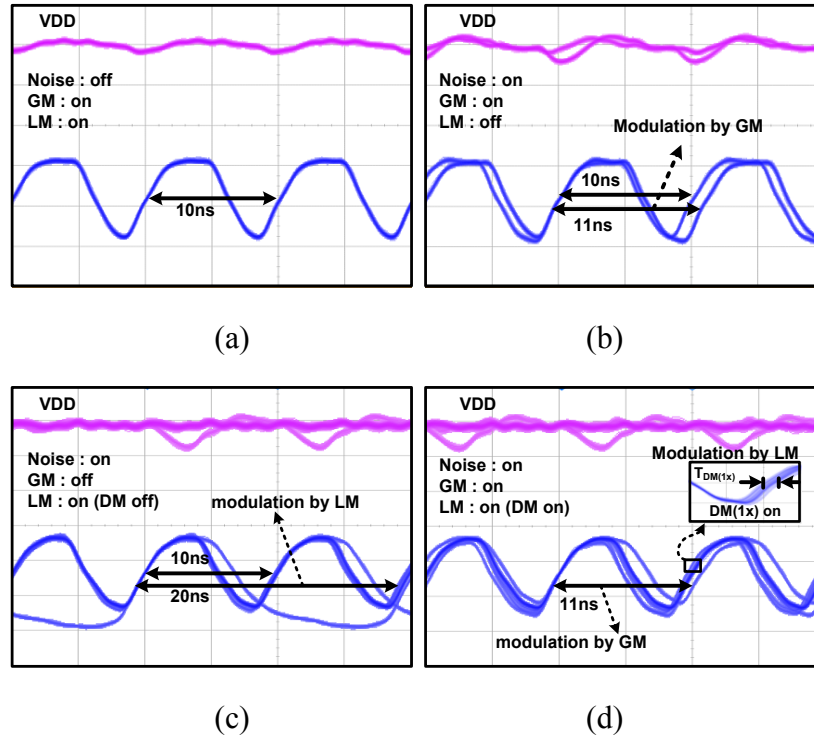
Figure 4.10: Measured waveforms of the modulated clock: (a) without noise; (b) only GM on; (c) only LM (DM off) on; (d) both GM and LM (DM on) on with noise.

Figure 4.11 shows the measured performance of the test pipelines under noise injection. In this measurement, the noise injection per cycle is varied. Timing errors are measured using the error counter to detect the failure of the pipelines. Although, the transient noise is injected locally, the injected noise results in a transient global noise as well. Since the GM is close to the power source and the test pipeline is close to the noise source, power noise at the GM is lower than that at the LM (Figure 4.11(a) inset). Hence, although the GM modulates the system clock, it could not prevent timing errors in the pipeline due to local noise as shown in Figure 4.11(a). As the LM is placed near the pipeline, it modulates the clock in response to local noise and prevents timing errors even at the highest noise injection frequency Figure 4.10(c) and Figure 4.11(b)). However,

with the DM off (clock gating mode), the pipeline operates at reduced F_{eff} (Figure 4.11(b), the GM off). Turning the DM on significantly increases F_{eff} as illustrated in Figure 4.11(b). With both the GM and the LM (DM on) on, F_{eff} is improved further as the GM modulates the system clock in response to global noise reducing the probability of the local clock gating (Figure 4.10(d) and Figure 4.11(c)). Note with both the GM and the LM on, the timing errors are prevented even under transient noise. With a direct clock input, the measured maximum frequency was 93.3MHz under noise injection. The measured F_{eff} with the proposed modulation [GM+LM(DM on)] reaches 100MHz when injection frequency is equal or less than 1/5. Thus, the proposed clock modulation method increases performance by 7.2% while maintaining correct operation of the pipelines under supply noise. The measured power consumptions of the GM and the LM at 0.81V are 56μW and 46μW, respectively. The die-photo and the characteristics of the implemented test chip are shown in Figure 4.12. The key feature of the proposed design in comparison to existing works in the area of clock modulation in response to supply noise is illustrated in Table 4.1.
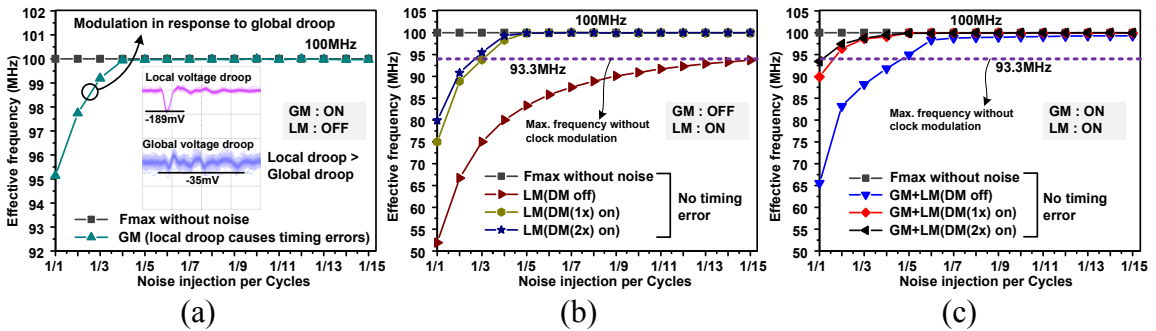
Figure 4.11: Measured effective frequency under global and local supply noise: (a) only GM on; (b) only LM on; (c) GM and LM on.

Technology		130 nm
Voltage		1.30 ~ 0.74V
Frequency		250 ~ 66.7MHz
Area	GM	5070 um²
	LM	3990 um²
Power	GM (100MHz out)	56.0 uW @0.81V,1GHz input
	LM (100MHz out)	46.4 uW @0.81V,100MHz input
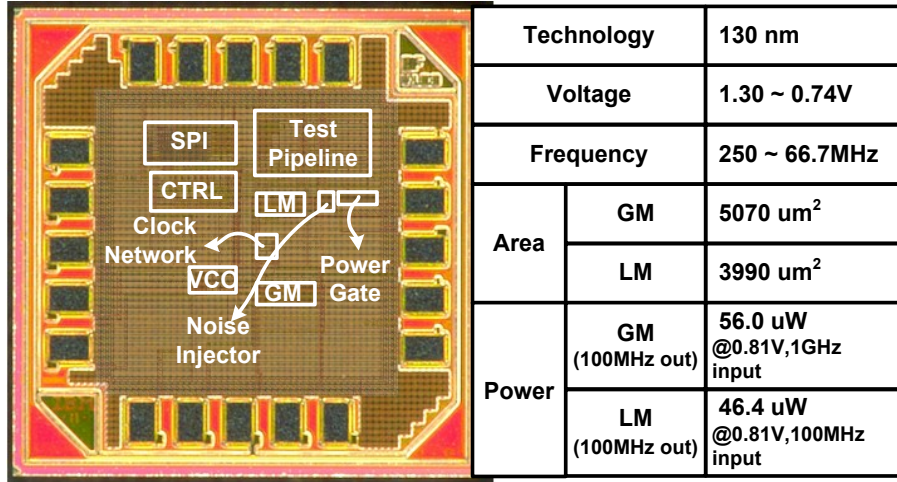
Figure 4.12: The die-photo and characteristics of the chip.

Table 4.1: Comparison of prior works.

	[58]	[59]	[60]	[61]	This work
Global power noise	AC,DC	AC (first droop)	AC, DC	AC, DC
Local power noise	no	no	no	partially	yes
Control speed	slow	slow	slow	>1.5 cycle	within 1 cycle

4.3   *Adaptive bias-voltage generation*

Minimizing power consumption of digital systems in mobile applications is quite challenging due to increasing variations, such as process, voltage, and temperature. In addition, a recent research trend is moving towards on-chip voltage regulation to explore benefits of multiple voltage domains, fast dynamic voltage frequency scaling (DVFS), good supply noise reduction, and cost effectiveness [89]. This section proposes a feasible solution considering above-mentioned technical challenges.

A system requires a voltage guard-band to operate at the target frequency without any errors due to variable factors. An increased voltage guard-band considering worst-corner cases can lead to unnecessary power overhead. If the extent of variations is unknown, there is no way but to add the maximized guard-band considering all possible worst scenarios even though it is least feasible. Assuming the extent of static variations can be detected, a supply voltage level to compensate for the detected variation amount can be applied, and the target performance can be achieved. In addition, if supply voltage can be adjusted only at the detection of dynamic variations, additional voltage overhead considering dynamic variations can be removed. This technique is called adaptive voltage scaling (AVS). Thus, AVS is becoming popular since it can reduce the system power applying not a fixed voltage but an adaptive voltage required for a circuit to operate a target performance. However, voltage assignment is a still challenging problem. AVS works assuming a supply voltage is known for a target performance considering all variations. In addition, providing an on-chip voltage reference is an important issue needs to be solved considering the on-chip voltage regulators. Providing external voltage references for multiple on-chip voltage regulators is costly and inefficient for variation compensation. Deciding an appropriate voltage level for a target frequency considering DVFS is also important feature for on-chip voltage regulators.

Previous works explored methodologies to decide a supply voltage for a target performance considering variations [64], [86], [88]. There are two ways—open-loop and

70

closed-loop method—to find the target voltage [86]. First, open-loop method requires a delay detector circuit and a pre-characterization process. After the evaluation of the delay of a circuit, proper voltage to compensate for the delay variation can be pre-characterized and be stored in a table. Depending on the delay variation detected, proper voltage can be found from the already constructed table. Since the target voltage can be found directly from the sensor output value, target voltage can be found quickly. However, it requires a matching process between the delay sensor and the real critical paths and the pre-characterization process to construct the voltage table. In addition, the number of table should be increased depending on the different frequencies, which a circuit can operate for dynamic voltage frequency scaling (DVFS). Second, closed-loop method requires a feedback loop from delay sensing to voltage control. Adjusting the voltage until the target delay is met, the target voltage can be found through the feedback [64], [86]-[88]. The main benefit of this method is that the pre-characterization process is not required and it works at different frequency targets without additional circuits, though it requires iteration to reach the target voltage. However, finding the target voltage based on the behavior of real circuits [64] could interrupt the real operation of the circuits. In addition, the closed loop system necessarily requires careful design considerations for loop stability. Furthermore, the fast acquisition and the area-efficiency are also important design factors.

The main objective of this research is to develop a cost-effective stable bias-voltage generator that can provide fast generation of a target supply voltage at a given target frequency while not interrupting the operation of real circuits considering on-chip voltage regulators.

4.3.1 Target voltage generation methodology

The objective of this research is to implement a closed loop solution, which can find the operating voltage of a circuit for a target frequency under static and dynamic

variations as shown in Figure 4.13. The target voltage is used as a reference voltage for on-chip regulators [89] to apply the adaptive supply voltage to the load circuits. The direct generation of bias-voltage can be beneficial compared to all digital methodologies. First, designers do not need to consider quantization errors. Since the output is not digital but analog, unnecessary voltage margins due to quantization errors can be included in the supply voltage level. Second, the proposed approach can reduce the design burden in an on-chip voltage regulator. The quantization errors necessitate a voltage regulator with multiple offsets and fine grains (i.e., 12.5mV voltage resolution). The design overhead considering programmability of the on-chip voltage regulators can be quite high. Third, the on-chip voltage reference generation makes external voltage references unnecessary. Thus, the cost for providing external voltage references and required analog pins can be saved.
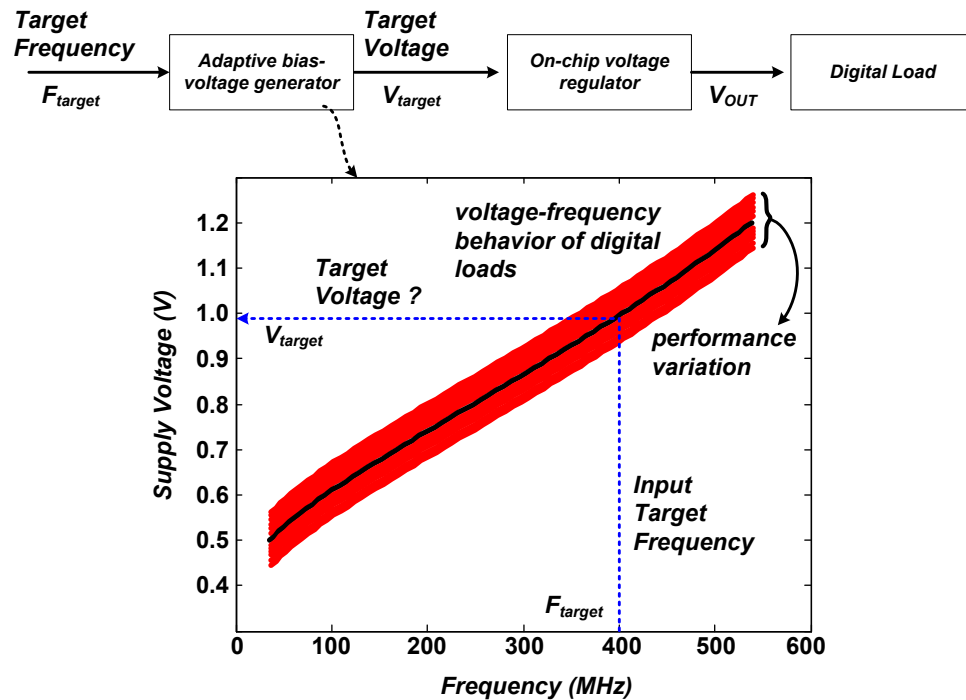
Figure 4.13: Generation of a voltage at the given target frequency.

4.3.1.1   *Adaptive voltage generation methodology*

The overall adaptive voltage reference generator is comprised of a delay comparator, a tunable delay line, a charge pump, a loop filter, and a power stage as shown in Figure 4.14. The overall system generates a reference voltage (V_{REF}) at which the circuit can operate with the input reference clock frequency (CK_{REF}). The output delay of the tunable delay line is compared with the input reference clock (CK_{REF}). If the delay of the delay line (T_D) is smaller than the target delay (T_{REF}), DN pulse is set to decrease the voltage at VC node as shown in Figure 4.14. As a result, VDL and V_{REF} increase. The increased VDL affect TD, which decreases. On the other hand, if T_D is higher than T_{REF}, UPn pulse increases the voltage at VC node, and hence, VDL and V_{REF} decrease. This iterative process finds the target voltage, V_{REF}, to make T_D equal to T_{REF}. Total operation is exactly same as a delay-locked loop (DLL).
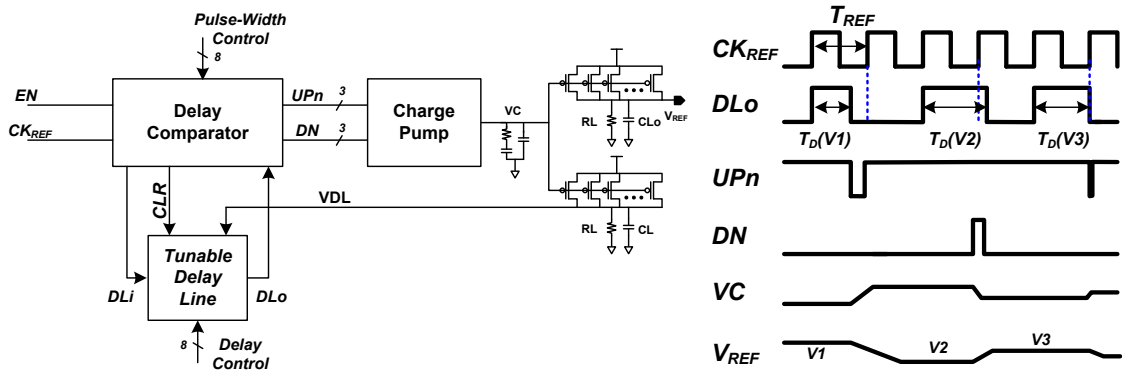
Figure 4.14: Block diagram of the adaptive voltage generator.

4.3.1.2   *Circuit Implementation*

This section discusses circuit details of major components of the voltage reference generator.

4.3.1.2.1 Delay Comparison

The block diagram of the delay comparison block is shown in Figure 4.15. EN is a signal to start delay measurement of the tunable delay line. The rising edge of CK_{REF} sets ST, which is used to set FF1 and FF2, and consequently PL1 and PL2 are set to high. PL1 signal is used as the input of the tunable delay line as shown in Figure 4.16. This PL1 activates the tunable delay line. Then, the delay line starts propagating high signal, which is again fed back to DLin pin. Since the delay line operates at lower voltage than the delay comparator block, it requires a level shifter. However, DLin generates RP1 to clear PL1. As a result, the pulse width of PL1 is affected by the delays of the delay line and the level shifter. After a one clock period of CK_{REF}, EN is cleared, and hence, ST is also cleared. Consequently, pulse generator (PG2) generates a reset pulse (PR2), and PL2 is cleared. As a result, the pulse with of PL2 signal is equal to the clock period of CK_{REF}.

Figure 4.15: Block diagram of the delay comparator.

Figure 4.16: Operational waveform of the adaptive voltage generator; (a) voltage down; (b) voltage up.

The pulse width of PL2 (PW2) is determined by the clock period of CK_{REF}, and the delay of the delay line (PW1) determines the pulse width of PL1. If PW1 is smaller than PW2, it implies the delay of the delay line needs to be increased to be matched to PW2.

4.3.1.2.2 Tunable delay line

Implementing a real critical path is a not practical method since it is not a scalable solution. On the other hand, tunable delay line is a programmable method with a good scalability. However, it requires a matching process between the real critical paths and the tunable delay line. This research includes the tunable delay line, which is shown in Figure 4.17. This work includes a special delay line, which has a clear input (CLR). If the CLR is cleared, the internal node values of the delay line are all cleared. The benefit of this reset scheme of the delay line is shown in Figure 4.18. The main technical issue of DLL is harmonics locking. As shown in Figure 4.18, when the delay of the delay is too high,

75

the DLL architecture cannot detect this harmonics locking problem. To prevent this issue, complex control circuits are required. This work proposes a delay line with a reset scheme. If the input to the delay line is cleared, the internal nodes of the delay line are all cleared after a fixed delay amount ($T_{CK}+\Delta T$). Thus, the possible erroneous propagation greater than or equal to $2T_{CK}$ can be cleared.

The level shifter in Figure 4.17 is used for voltage level conversion and delay compensation at low voltage. This level shifter is the part of the delay comparator.
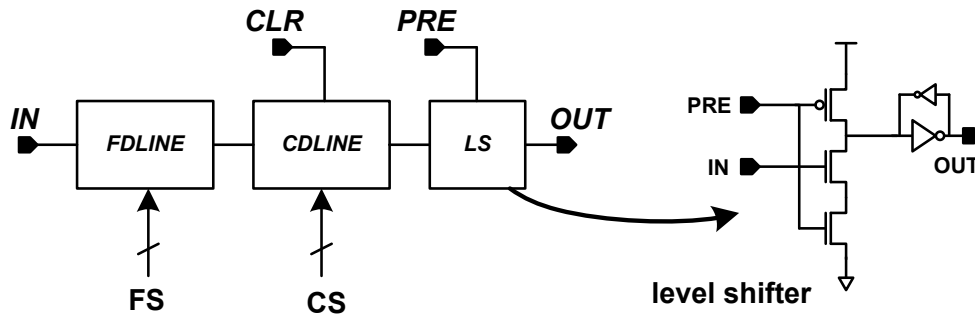
Figure 4.17: The delay line architecture and the level shifter.

(a)   (b)
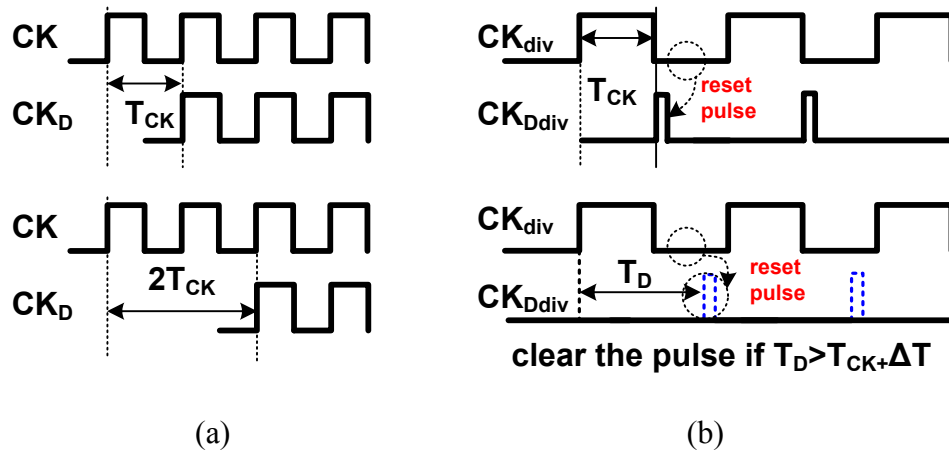
Figure 4.18: Concept of delay line with reset to prevent harmonics lock; (a) harmonics lock case (b) delay line with reset.

If VDL (the supply voltage of the delay line) is low, the delay mismatch between the delay line and the real critical paths can increase as shown in Figure 4.19. At low voltage, the delay difference between the delay line and the critical paths can become negative as shown in Figure 4.19(b). However, the propagation delay of the level shifter also increases as the voltage of delay line decreases. As a result, the increased delay of the level shifter at low voltage adds to the delay of the delay line, and the mismatch at low voltage can be compensated with the level shifter as shown in Figure 4.19(d).
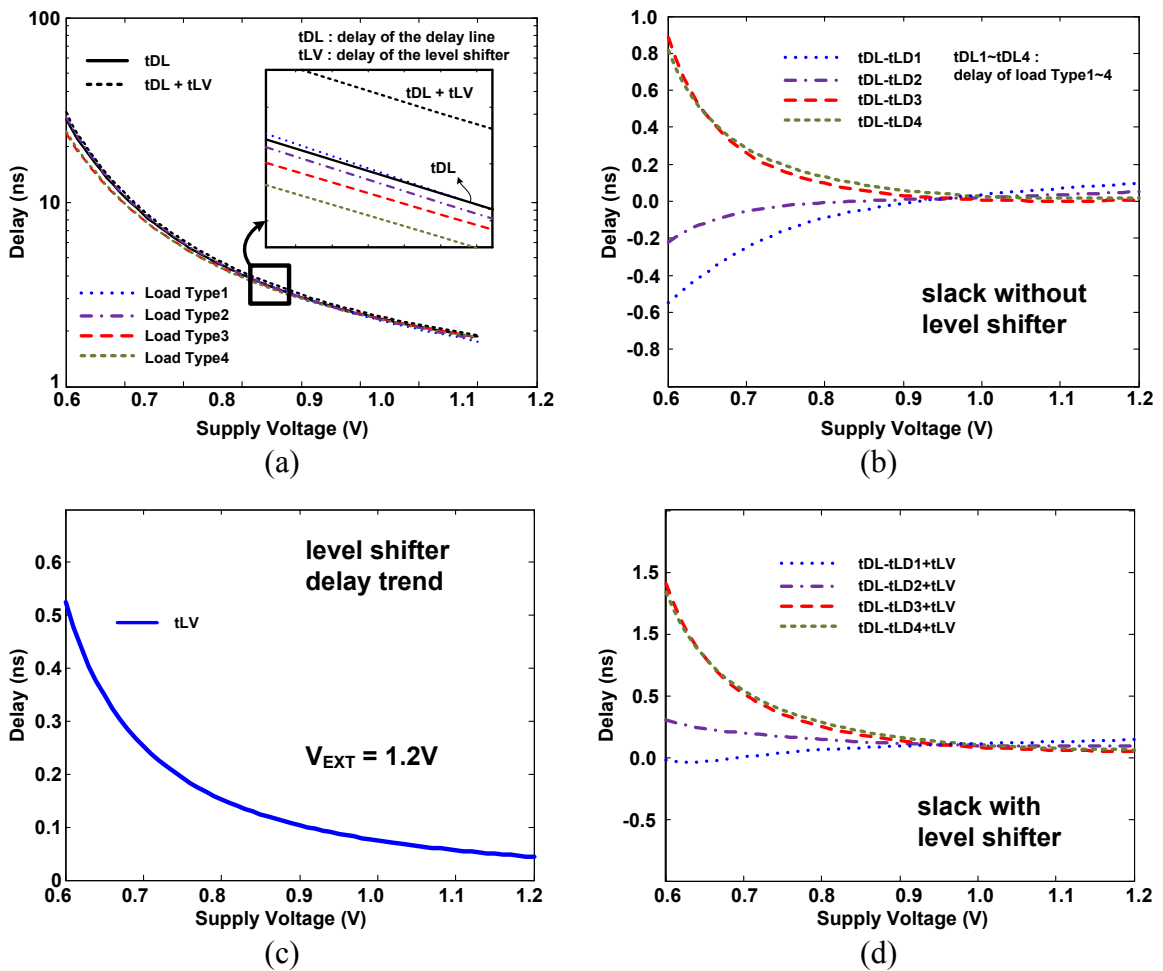
Figure 4.19: Delay compensation with a level shifter; (a) delay versus supply voltage; (b) delay mismatch according to supply voltage; (c) level shifter delay; (d) compensated mismatch.

4.3.1.2.3 Power stage

The proposed system includes two identical power stages. One power stage is used to provide the voltage for the tunable delay line (TDL). The load capacitance of the VDL node is small in this design. It moves the dominant pole at the power stage towards higher frequency, which allows better stability and higher bandwidth of the loop. Instead, it can create voltage noises at VDL, which is not appropriate for a voltage reference. Thus, this work proposes shadow power stage, which creates clean voltage reference as shown in Figure 4.20. Furthermore, it is possible to drive a heavy capacitive load (C_{EXT}) without interrupting the feedback loop. The external capacitive load is isolated from the feedback loop.
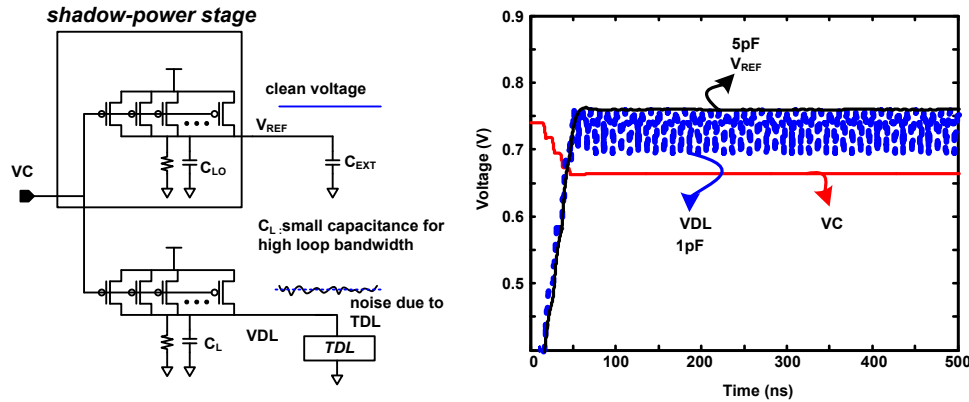
Figure 4.20: Power stage architecture.

An additional benefit of the shadow-power stage is automatic safety margin in V_{REF} generation. Since the power stage includes the current of the delay line, V_{REF} has an offset as much as the current of the delay line. It means this offset will increase in proportion to the current of the delay line. Since the current of the delay increases in proportion to the input reference clock, higher offset voltage in V_{REF}, higher safety margin, is generated. In higher clock frequency, voltage droop in the power network can increase. Thus, higher safety margin is required considering higher voltage droop at

78

higher operating frequency. The shadow-power stage automatically guarantees this automatic compensation for voltage droops at high operating frequency.

4.3.2 Simulation results

This section presents simulation results of adaptive voltage generator under static and dynamic variations. The design is implemented with a 130nm CMOS technology. In addition, automatic voltage generation according to the input clock change is shown. It implies the proposed circuit can enable a system to operate with fast and automatic DVFS.

4.3.2.1 *Process variation*

The MC simulation results with static process variations are shown in Figure 4.21. With a fixed supply voltage (0.95V), the normalized frequency ranges from 0.8 to 1.2 due to process variations. Thus, the operating frequency of the chips should be 0.8 considering the yield. It means a performance loss for most cases. On the other hand, the performance of a circuit with the adaptive voltage generator varied from 1.01 to 1.08. To meet the performance target (higher than 1), the operating voltage should be increased from 0.95V up to 1.1V. The average voltage of the adaptive supply was 0.974V. On average, 0.126V (1.1V-0.974V) voltage guard band is required considering process variations without adaptive supply voltage. The proposed work achieved 85.58% reduction in the standard deviation. From the simulation results, it can be found that the overhead comes from the worst corner can be compensated.
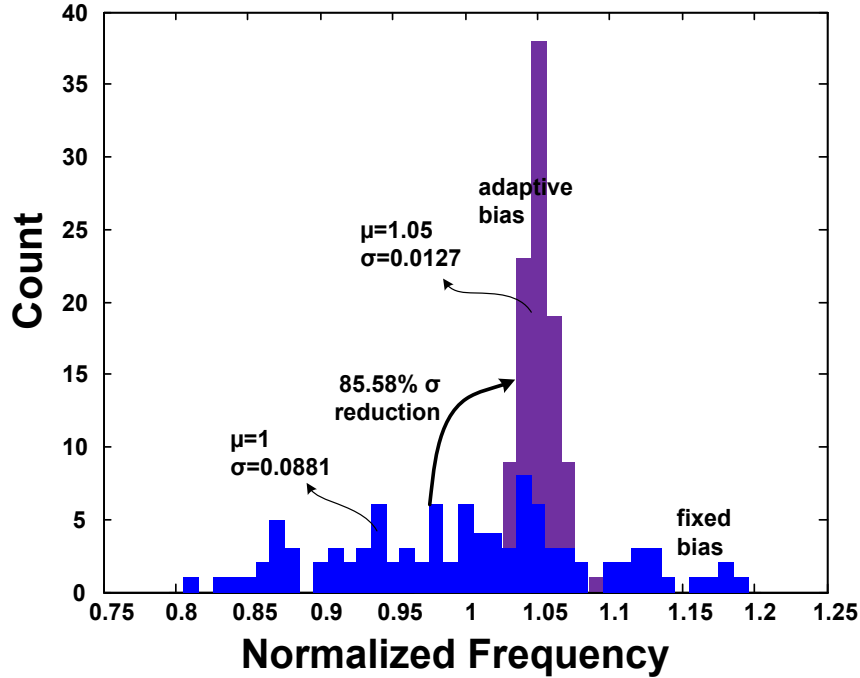
Figure 4.21: Performance variation under process variation.

4.3.2.2   *Aging effect*

To emulate the NBTI aging effect, the body bias of pMOS transistors are increased gradually. The pMOS body bias higher than the supply voltage creates a reverse body-bias condition and increases V_{TH} of pMOS transistors. As a result, the delay of critical paths will degrade slowly. The maximum frequencies of different critical paths are shown in Figure 4.22(a). Depending on the path types, the degradation ranged from 20.13% to 24.13%. The adaptive voltage level according to delay degradation is shown in Figure 4.22(b). As a result, the delay variation of critical paths with adaptive voltage generator ranged from 0.99% to 3.12%. The results imply that the aging impact on delay up to 24.14% can be minimized since the adaptive voltage generator find the voltage continuously to compensate for the delay degradation. As a result, a voltage guard band considering the aging effect can be reduced. In this test case, the required voltage guard band considering delay degradation up to 24.14% is 60mV.
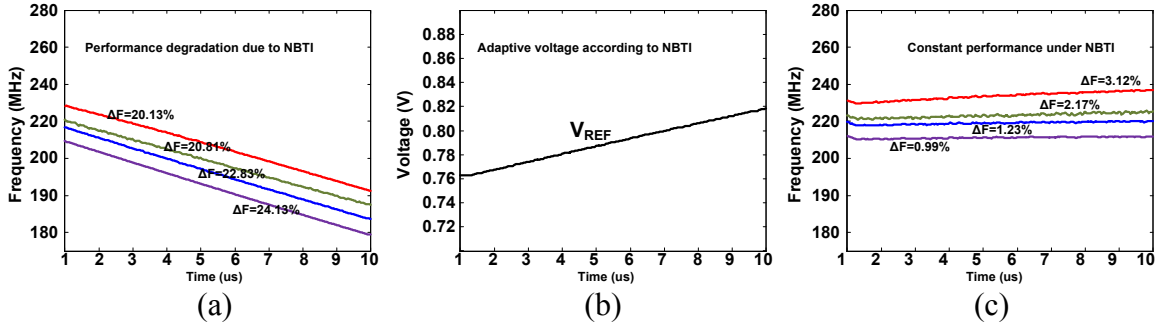
Figure 4.22: Generation of a voltage at the given target frequency; (a) performance variation under aging; (b) adaptive voltage change; (c) compensated performance.

4.3.2.3 *Temperature variation*

The simulation was conducted varying the temperature from -40℃ to 120 ℃ as shown in Figure 4.23. The performance variation under the temperature variation at 0.95V supply voltage was 20.62%. With the adaptive voltage reference, the performance variation was within 2.13%. The generated voltage reference at 120 ℃ was 1.042V. It implies 95mV voltage guard band is required without adaptive voltage reference considering the worst temperature corner.
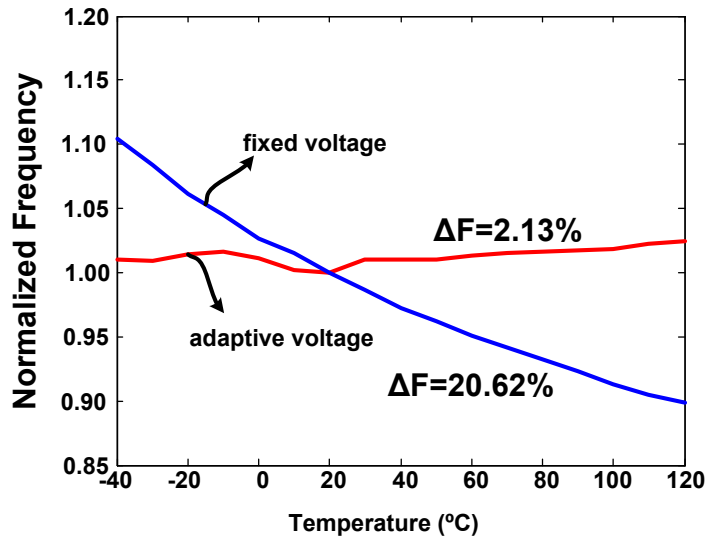
Figure 4.23: Temperature compensation.

4.3.2.4   *Dynamic voltage frequency scaling*

The automatic DVFS is one of the main benefits of the proposed adaptive voltage generator. As shown in Figure 4.24, the V_{REF} adaptively changes to make the critical paths operate above the target frequency. In addition, at high operating frequencies, different types of load circuits have higher frequency margin, which indicates higher frequency margin or voltage margin. Considering voltage droops at high clock frequencies, increased voltage margin helps preventing possible timing errors.

(a)   (b)
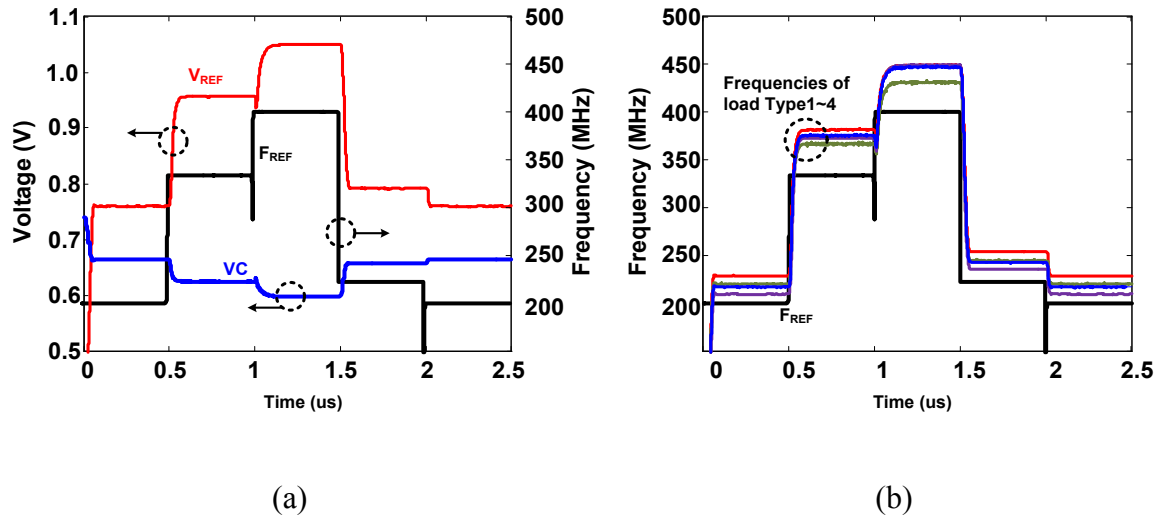
Figure 4.24: DVFS simulation; (a) voltage change according to input frequency change; (b) automatic DVFS.

4.4   *Summary*

This chapter presented two replica-based approaches to adapt to static and dynamic variations. First, this research presents an effective way to prevent timing errors by modulating the system clock and the local clock in response to DC and transient supply noise. The direct clock modulation from the replica circuits allows within-a-cycle frequency modulation which enables fast clock adaptation to fast transient noises. The measurement results demonstrate that a pipeline employing the proposed all-digital clock modulation can operate reliably over a wide operating voltage range even under transient

supply noise. Second, the proposed work explores a DLL-based method to find a target operating voltage for a target frequency. The benefit of the DLL-based approach is simple and stable loop control. The possible harmonics-locking problem associated with the DLL scheme is solved by the proposed delay line with a reset signal. The delay line with a level shifter provides automatic delay-mismatch compensation at low voltages. The proposed shadow-power stage provides stable feedback loop even with a heavy capacitive load. In addition, this shadow-power stage benefits providing an adaptive safety margin considering high voltage droops at input high frequency. The proposed adaptive voltage generator provides a solution to minimize the voltage guard band under process variations, aging effects, and temperature variations. An additional key benefit is an automatic DVFS feature. Most of all, the proposed solution is effective for on-chip regulators.

CHAPTER 5

DESIGN-INTRUSIVE APPROACH

5.1   Introduction

A digital system without safety margins necessarily can have functional failures under dynamic variations. Thus, if the system can detect the errors and recover from the errors, it can operate without any safety margin. Since this methodology detects the errors in situ (in the real data paths), it obviates the need for replica circuits and makes safety margins unnecessary. Instead, it requires modification in real circuits to implement error detection and correction methods. However, there are two approaches for resolving timing errors. One approach is to stall the pipelines by gating the clock to allow propagation of the correct data when errors are detected [63]. However, this method has a strict control-time requirement (i.e., control time from the error detection to the clock gating circuit) [64]. Hence, it cannot be applicable to high performance microprocessors. An alternative approach for error recovery mechanisms is architectural replay [65]-[70]. In microprocessors, the erroneous operation can be re-performed by flushing the pipeline and re-executing the instruction (architectural reply). Since an architectural replay is an embedded function in microprocessors (i.e., it is like an operation in the case of a branch misprediction), it has no limitation in operating frequency of microprocessors. However, the architecture replay can only be used in microprocessors and not for generic circuits. In addition, this error recovery method can incur significant power and performance penalty for flushing the pipelines and re-executing instructions when the erroneous operations are detected. Furthermore, it is required to change the operating condition (i.e., increasing the voltage or reducing the frequency) to prevent errors in the next try since the same instructions are executed again.

This chapter presents two error-prevention techniques to minimize performance penalty associated with managing timing errors. Those two techniques are platform-independent solutions, which are applicable to general circuits. The first solution is an error-prevention technique with a performance penalty less than a clock cycle. It utilizes time-borrowing and clock-stretching (TB-CS) techniques. However, this solution has a strict control time requirement. Thus, it is difficult to apply the first solution to high performance applications (i.e., operating at high frequencies). The second solution utilizing programmable-time-borrowing and delayed-clock-gating (PTB-DCG) is presented for the better trade-off between the control time requirement and the performance penalty. This solution allows the relaxed control time requirement, thereby achieving high frequency operations.

5.2   *Time-borrowing and clock-stretching*

This chapter presents a method to prevent the timing errors in advance to improve tolerance to delay variations in logic stages in a pipelined system with a minimized performance penalty (less than a clock cycle) while operating the system at a clock period less than the critical path delay. The approach couples the concept of time borrowing with innovative circuit techniques to prevent timing errors [71]. The time-borrowing is a well-known concept in pipelines designed with pulsed-latches or soft-edge flip-flops where valid signal transition is allowed even after the clock edge (during the limited transparent time period) resulting in propagation of correct values to the next stage [72]-[74], [76]-[81].

This section presents timing error prevention using time borrowing and clock stretching to enable design with low safety margin. For a target operating voltage, the pipeline with the proposed approach can operate at a clock period less than the critical path delay without causing any timing error. Hence, the pipeline can have better

performance for a given power. The critical paths are the ones that are most likely to fail under PVT variations or aging. The proposed approach prevents errors in the critical paths when they are activated and hence, helps tolerate dynamic variations in the delay of a logic stage for a given input frequency. Compared to architecture replay, the proposed approach is more general and can be applied to non-microprocessor pipelines also. Compared to clock gating based error recovery, the proposed approach has a lower performance penalty (fraction of a clock cycle), which can be significant when critical path activation probability is high. Finally, unlike error detection and correction, the proposed approach guarantees minimum system performance.

5.2.1 Methodology for prevention of timing error

In this section, the underlying methodology of the proposed effort is discussed. Consider a two-stage pipeline as shown in Figure 5.1. In Figure 5.1(a), if the critical path delay [clock-to-Q delay (T_{CK-Q}) + logic delay (T_{P1}) + setup time (T_{SETUP})] is greater than the clock period (T_{CK}), the negative time slack causes timing failures in the pipeline. If pulsed latches are used in the pipeline as shown in Figure 5.1(b), the pipeline can have more flexible timing budget [17]. A pulsed latch has time-borrowing characteristics, and this property makes the timing requirement relaxed. Because of this time-borrowing behavior, the pulsed latch can sample the correct data as long as the path delay is less than the sum of the clock period and time-borrowing window ($T_{CK} + T_{BW}$). However, the borrowed time (i.e., $T_{CK-Q} + T_{P1} - T_{CK}$) is added to the path delay of the next stage. In the next stage, if the increased total path delay [$=(T_{CK-Q} + T_{P1} - T_{CK}) + T_{D-Q} + T_{P2} + T_{SETUP}$, where T_{D-Q} is the data-to-Q delay of the latch, and T_{P2} is the logic delay of stage 2] is greater than the sum of the clock period and time-borrowing window ($T_{CK} + T_{BW}$), the pulsed latch in the next stage cannot sample the correct data D3 as shown in Figure 5.1(b).

Therefore, the pulsed latch with a limited time-borrowing widow can prevent timing failures in one stage but cannot in the following stage.
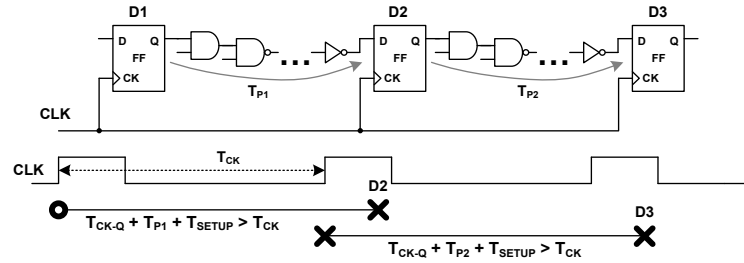
(a)
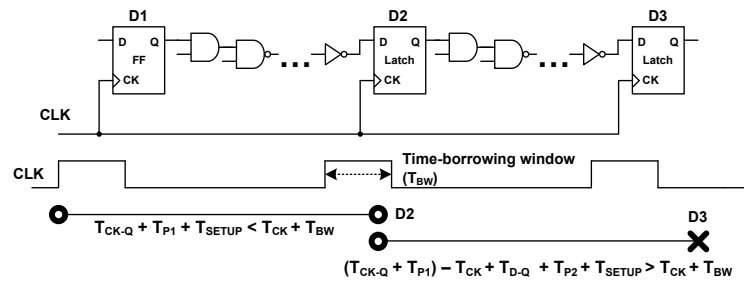
(b)
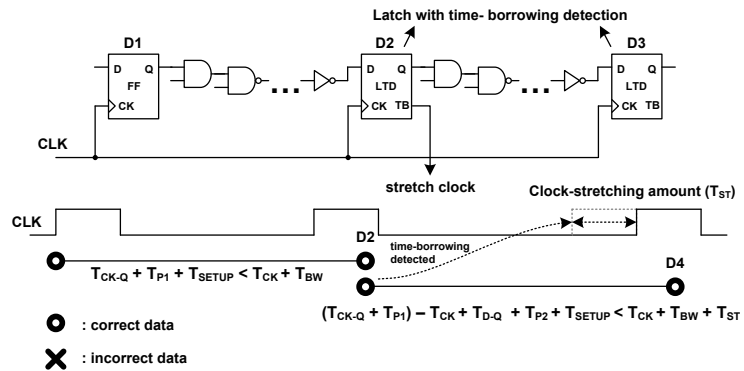
(c)

Figure 5.1: The conceptual operation of the pipeline with (a) the flip-flops, (b) the pulsed latches, and (c) the LTD with clock stretching.

The preceding scenario can be avoided if the increased path delay is resolved by stretching the clock period to prevent possible timing errors in the next pipeline stage. This approach is illustrated in Figure 5.1(c). In the clock-period-stretching process, the

input clock frequency to the system is not changed, but the period of the internally generated clock is changed dynamically at every clock cycles. The proposed approach uses a special latch, hereafter, referred to as the pulsed latch with time-borrowing detection (LTD), only at the timing critical paths of all pipeline stages. The LTD operates as a pulsed latch where the pulse width defines the time-borrowing window (T_{BW}). The occurrence of the critical-path transition within T_{BW} is defined as a *time-borrowing event*. The LTD allows time borrowing in the current stage when critical paths are activated and generates a detection signal. The proposed LTD detects time borrowing and generates a time-borrowing detection (TD) signal in the presence of time borrowing. Based on the TD signal, the clock period is stretched by T_{ST}. Thus, the pipeline can guarantee the correct operation using clock stretching as long as the increased total path delay [$=(T_{CK-Q} + T_{P1} - T_{CK}) + T_{D-Q} + T_{P2} + T_{SETUP}$] is less than $T_{CK} + T_{BW} + T_{ST}$. As a result, the design with the LTDs and the clock stretching concept can prevent possible timing errors with the elastic clock control.

To guarantee correct operation of a pipeline with the proposed timing error prevention scheme, the timing requirement for the worst case is given by:

$$T_{CK-Q} + \max(T_{Pn}) + T_{SETUP} < T_{CK} + T_{BW}, \qquad (5.1)$$

where $\max(T_{Pn})$ is the maximum logic delay considering all pipelined stages. The input clock period and the stretched clock period are defined as T_{min} and T_{max}, respectively. In this work, time borrowing window (T_{BW}) and the clock stretching amount (T_{ST}) are given by:

$$T_{BW} = T_{ST} = T_{max} - T_{min}. \qquad (5.2)$$

T_{BW} and T_{ST} are generated from the multiple clock phases. T_{BW} and T_{ST} are defined as 1/4 or 1/8 of the input clock period (T_{min}) depending on whether T_{BW} and T_{ST} are generated from 4-phase or 8-phase clocks, respectively.

The proposed method enables a circuit to operate elastically at the clock period of T_{min} or T_{max} according to the detection of time borrowing [Figure 5.2(a)]. If the critical

paths (the paths that cause time borrowing) are not activated, the pipeline with the proposed approach operates at the minimum clock period, T_{min}. When the critical paths are activated, the design operates at the maximum clock period, T_{max}. As the clock period changes adaptively depending on the activation statistics of critical paths, the system with the proposed method will have different clock periods as shown in Figure 5.2(b). Hence, effective operating frequency (F_{EFF}) is defined to estimate the effective performance of the pipelined system as follows:

$$F_{EFF} = T_{EFF}^{-1} = [(P_C T_{max} + (1 - P_C) T_{min})]^{-1} , \qquad (5.3)$$

where T_{EFF} is the effective clock period. The P_C is the probability of time-borrowing events. P_C function is different according to the designs. From the equation, it can be concluded that as P_C gets smaller, T_{EFF} gets smaller (i.e., higher performance). Hence, for a target operating voltage, the pipeline can operate at a clock period less than the critical path delay without causing any timing error. The effective performance depends on the activation probability of the critical path and can be better than a conventional design for a given power.

(a)   (b)
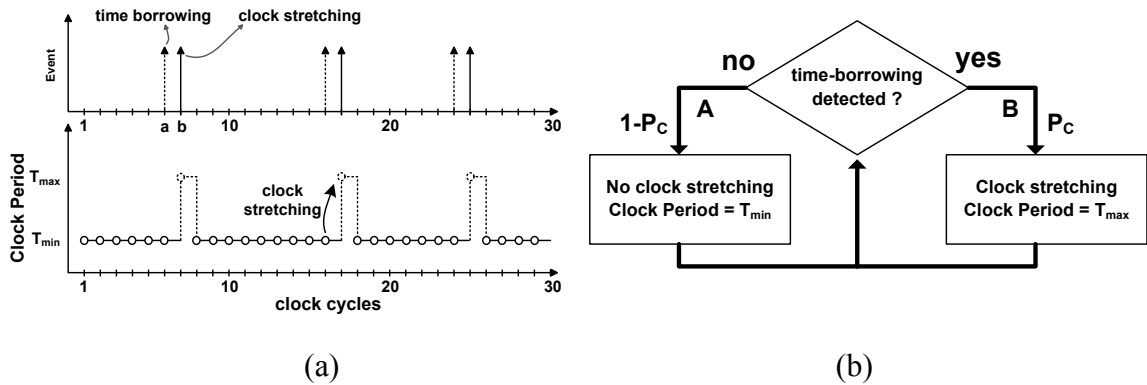
Figure 5.2: (a) The clock stretching concept in time domain and (b) the control flow of the proposed methodology.

5.2.2　Circuit-level implementation

5.2.2.1　<u>Latch with time-borrowing detection</u>

The LTD shown in Figure 5.3 is comprised of a latch and the time-borrowing detection circuit. The basic operation of the LTD used in this work is similar to the latches with the error detection circuit used in [66]-[70]. The time-borrowing window of the latch L0 in the data path is determined by the clock high pulse width generated from a clock pulse generator in the clock control circuit. If the input data D arrives before the rising clock edge, the output Q has valid transition like a flip-flop. If the input data D arrives late after the rising clock edge, the output Q still has valid transition like a latch as long as the input changes during the clock high pulse i.e., the time-borrowing window. In this case, the data sampled in the latch L1 will be different from the output of the buffer BUF0. Hence, the time-borrowing pulse (TBP) signal (i.e., the output of the XOR gate) will be high. Once the TBP signal is set during the high pulse of the clock, the pre-charged node (PRE) in the TBP detection circuit will be discharged, and eventually the TD signal will be set. The input change while the clock is high indicates time borrowing from the next pipeline stage, and the TD signal is set to notify this event. Therefore, the LTD allows valid output transition as long as the input arrives within T_{BW}. In the TBP detection circuit, there could be static current if TBP becomes high while clock is low. During clock low, transistor M1 should be turned off to prevent the case when both M0 and M1 are on. In the proposed design, the buffer BUF0 is used to match the input-to-output propagation delay (T_{D-Q}) of the latch L1. The latch L1 will be in transparent mode and behaves like a buffer while clock is low. Hence, although the input changes while clock is low, the unnecessary transitions of TBP can be prevented as illustrated in the A and B point in Figure 5.3(b). As a result, the TBP detect circuit can be implemented without a footer transistor in the evaluation path. It improves the evaluation speed and reduces area. The purpose of the buffer BUF1 is to make the M0 transistor turned off

before TBP is set or turned on after TBP is cleared. This can be achieved by making the buffer have fast rising time and slow falling time. It also helps extend the time zone where time borrowing can be detected (i.e., extend the pulse width of TD signal). However, the keeper circuit in the PRE node needs to be very weak considering the contention during pre-charge and evaluation. The time-borrowing window makes the setup-time requirement more flexible but makes hold-time requirement more stringent. The minimum delay requirement of the logic paths increases as the time-borrowing window in LTD increases. Therefore, more number of buffers to fix hold time violation should be inserted if a LTD is used with a short delay path. However, as the LTDs are used only for long delay paths (critical paths) in the proposed design the required number of hold fix buffers is expected to be less.
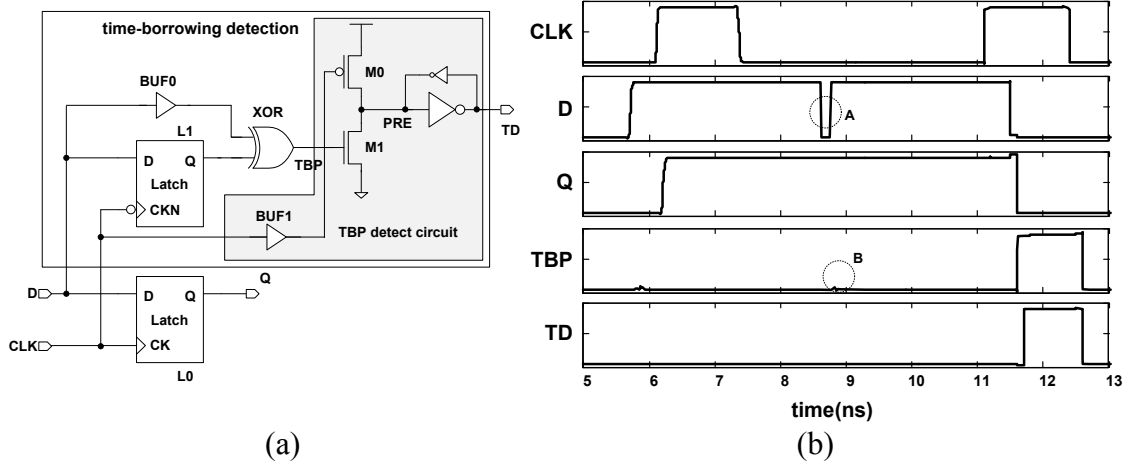
Figure 5.3: (a) The schematic of the proposed latch with the time-borrowing detection (LTD) and (b) its timing diagram.

5.2.2.2   *Time-borrowing detection collector*

Time-borrowing detection signals from the LTDs are combined to generate one clock shift signal that is used to stretch the clock period. The TD collecting (TDC) circuit shown in Figure 5.4 gathers TD signals from LTDs and generates the clock stretch signal

91

(SHIFT) for the clock shifter. The TDC circuit functions as a wired-OR logic and is implemented using dynamic logic. However, time-borrowing detection cannot be evaluated correctly in the TDC circuit if the pulse width of the TD signal is too short. This case can happen when the time-borrowing event happens almost near the falling edge of the clock. This can be limiting factor of the error-prevention range of the proposed technique. When the clock is high, the TDC circuit pre-charges the PRE node. After the clock becomes low, the PRE node is evaluated according to the value of the TD signals generated by the LTDs. However, the propagation time from the PRE node in a LTD to the TDC should be longer then the clock skew between the LTD and the TDC to avoid race condition. A Schmitt-Trigger inverter (SINV) is used in the TDC circuit to ensure sharp transition and increase noise immunity. The TBEN signal is used to turn off the TDC circuit to prevent transition of the SHIFT signal.
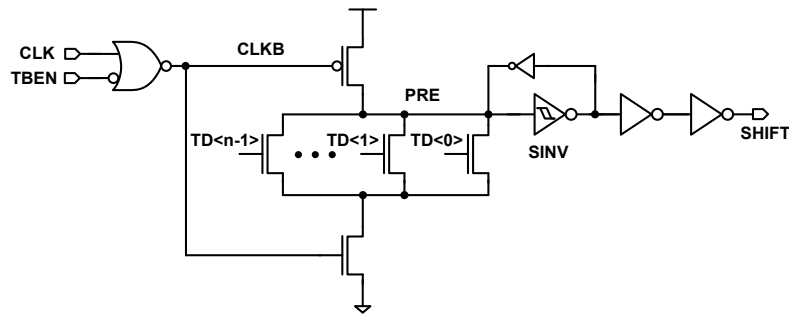
Figure 5.4: The schematic of the time-borrowing detection collector.

5.2.2.3 *Clock stretching circuit*

5.2.2.3.1 *Clock pulse generator*

A phase-locked loop (PLL) is a common building block for frequency synthesis in digital systems. The PLL includes a voltage-controlled oscillator (VCO) that generates the clock with the target frequency. The VCO is comprised of multiple stages like a

differential ring oscillator. Hence, it generates multiple clocks with the same frequency but different phases. For example, when the VCO has 4 differential delay cells like in Figure 5.5, there are 8 output clocks with different phases. The time difference of adjacent phase clocks is $T_{CK}/8$ assuming the clock period is T_{CK}.

A clock pulse generator [Figure 5.6(a)] is designed to generate multiple clock pulses from the VCO clocks. The high pulse width and the phase difference of each clock pulse are determined by how to match the different phase clocks to create clock pulses. The primary clock inputs (the pins marked in block in Figure 5.6(a) and (b)) determine the rising edge and the secondary clock inputs determine the falling edge of the generated clock pulse (CLK4P<3:0> or CLK8P<7:0>). Hence, the clock high pulse width (T_{BW}) is determined by the selection of clock phases to primary and secondary clock inputs (the matching marked A in Figure 5.6(a)). The selection of clock phases to the primary clock inputs decides the time difference (T_{ST}) of each clock pulses (matching marked B in Figure 5.6(a)). As mentioned earlier, T_{BW} and T_{ST} are considered to be equal in this thesis. 4-phase (4P) or 8-phase (8P) clocks are chosen to generate the clock pulses (Figure 5.6). Simulations in an 180nm CMOS technology show that the clock pulse generators in Figure 5.6 can have 4 clock pulses with $T_{CK}/4$ high pulse width and time difference or 8 clock pulses with $T_{CK}/8$ high pulse width and time difference (Figure 5.6).
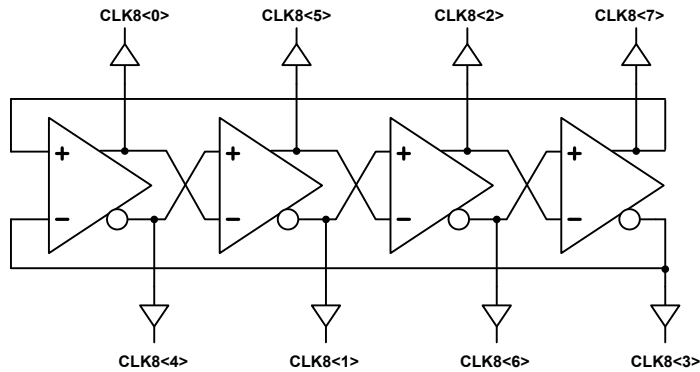
Figure 5.5: The block diagram of the ring VCO.
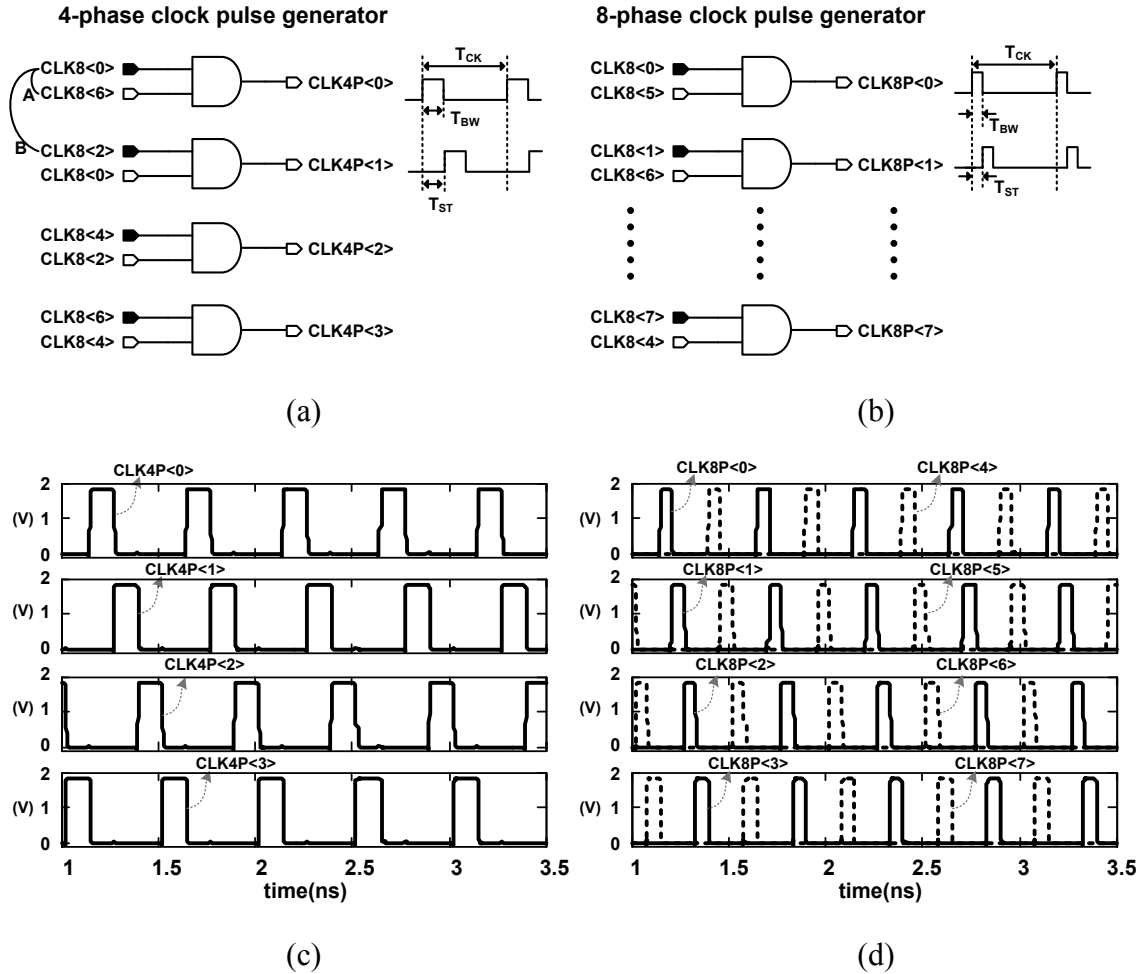
Figure 5.6: The clock pulse generator for (a) the 4-phase clocks and (b) the 8-phase clocks. The operation of the clock pulse generator for (c) the 4-phase clocks and (d) the 8-phase clocks.

5.2.2.3.2 Clock shifter

The phase-shifting circuit is designed as shown in Figure 5.7 to implement clock stretching. The clock shifter is comprised of shift registers and clock gating circuit. The purpose of the shift registers is to generate selection signals (SEL<3:0> or SEL<7:0>) that are used to select one clock pulse among multiple clock pulses with time difference but same frequency. The initial value of the shift registers is one-hot. Hence, only one of the multiple clock pulses is enabled at each clock cycle and the others are gated in the clock gating circuit.
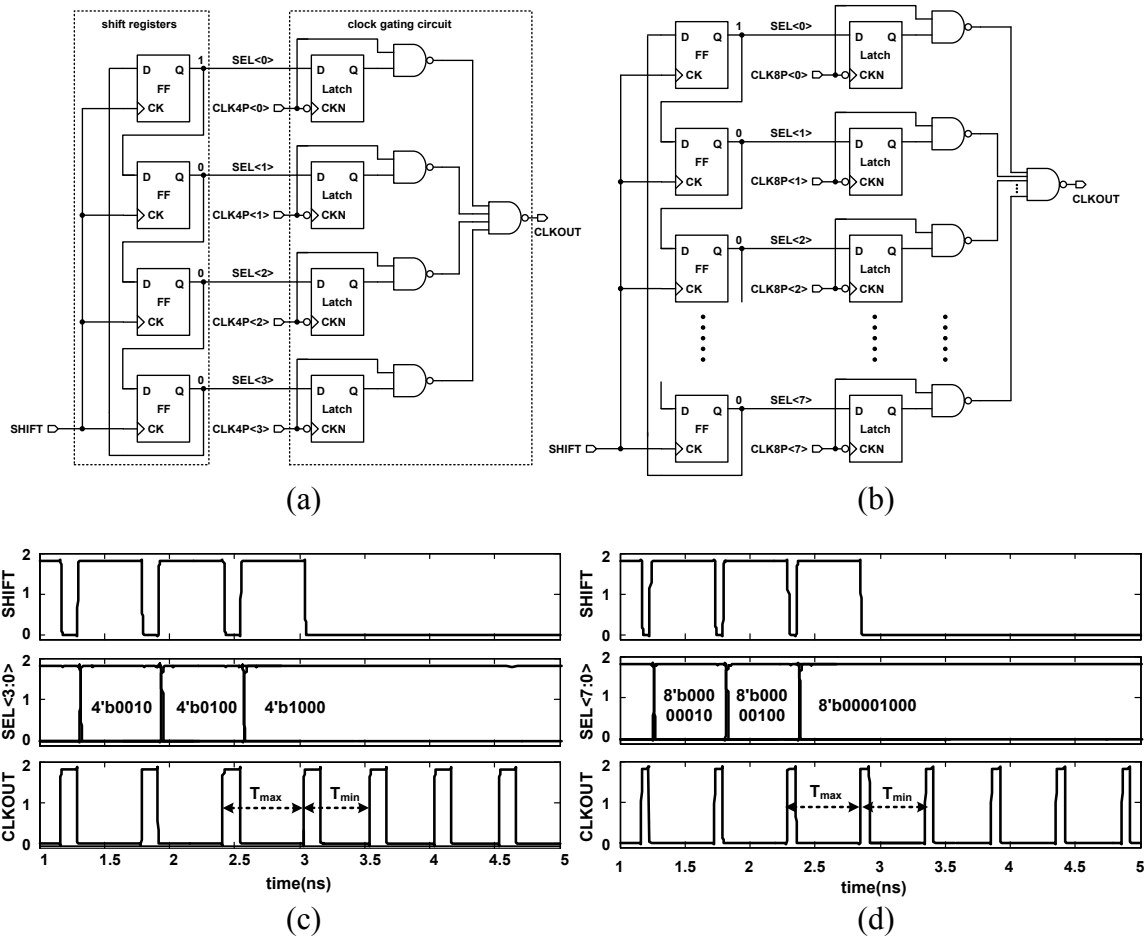
Figure 5.7: The block diagrams of the clock shifter for (a) the 4-phase clocks and (b) the 8-phase clocks. The operation of the clock shifter for (c) the 4-phase clocks (d) the 8-phase clocks.

When SHIFT signal transits from low to high, the shift registers shift the selection signals. This shifting selection signals indicates changing to a different clock phase. Eventually, by shifting the clock phase from one to other clock phase, the clock period can be stretched effectively as shown in Figure 5.7. Hence, without shifting selection signals, a clock pulse with the clock period (T_{min}) is delivered to the system. With shifting selection signals, which means time-borrowing detected, a clock pulse with the synthesized clock period (T_{max}) is generated in the clock shifter as shown in Figure 5.7. Thus, the clock shifter can change the different clock periods - T_{min} or T_{max} - depending on the presence of time borrowing.

5.2.3 Test chip and measurement results

The test circuit shown in Figure 5.8 was fabricated in an 180nm CMOS technology to verify the proposed approach. A simple 3-stage pipeline with the proposed methodology was designed with master-slave flip-flops (MSFF) in non-critical paths and LTDs in critical paths. The combinational logic paths were implemented with inverter chains to emulate the path delay distribution like in Figure 5.9. The MSFFs are used in non-critical paths (path0~path47) as shown in Figure 5.8. LTDs are used in 16 critical paths (path48~path63). The critical paths of the successive pipeline stages are assumed to be cascaded. This scenario is chosen in the design as it defines the worst-case performance penalty of the proposed approach. The TDC, CPG, and CS circuits are designed. CPG and CS circuits are different according to the selection of phase (4P or 8P), which defines time-borrowing window and clock-stretching amount.
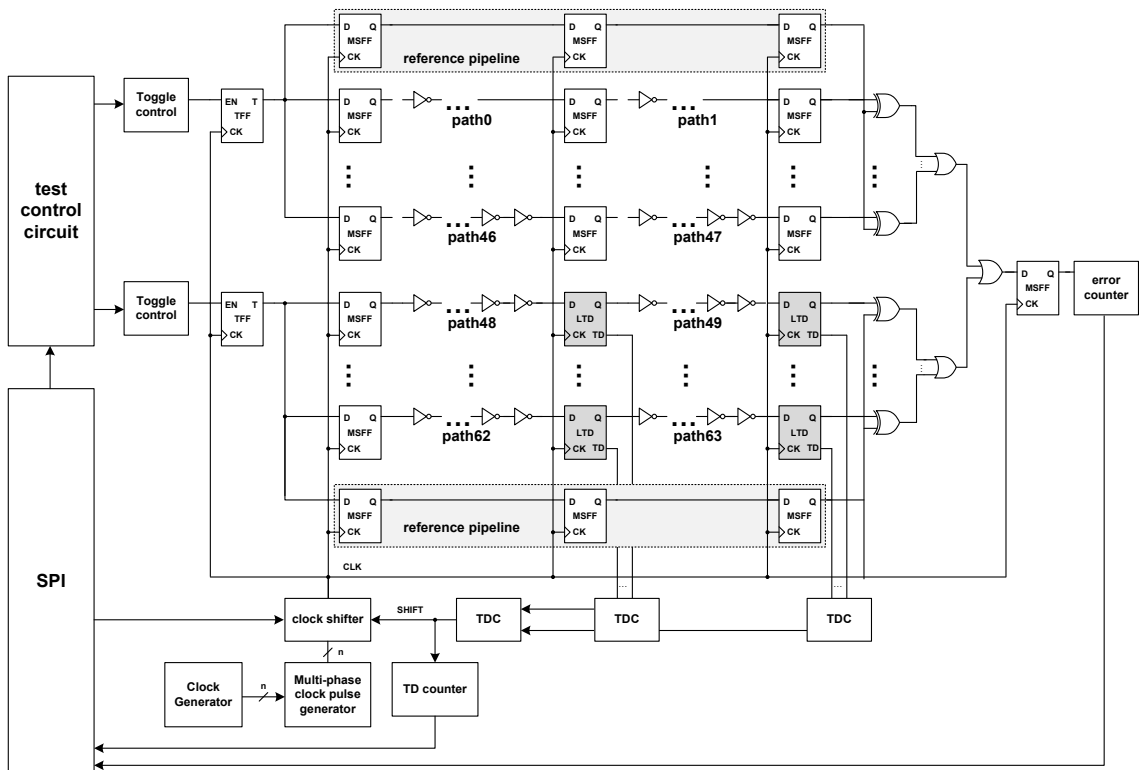
Figure 5.8: The block diagram of the test pipeline.
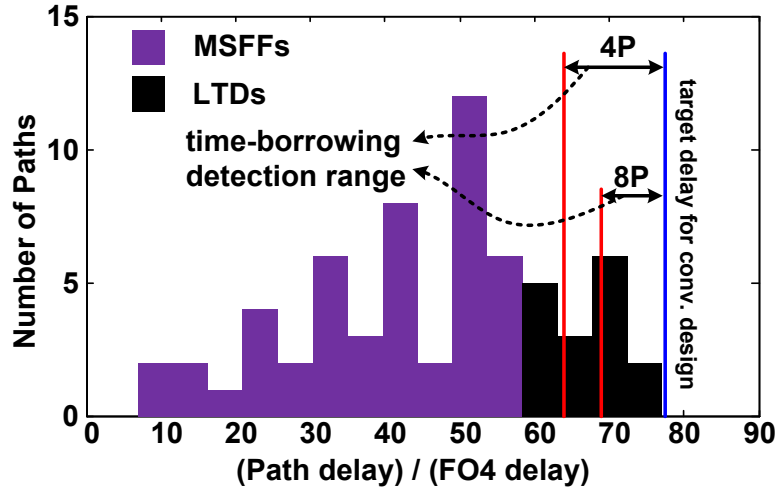
Figure 5.9: The path delay distribution (FO4 delay=76.23ps).

The test circuit includes serial peripheral interface (SPI) slave controlled by a test program from a computer. The SPI block contains a 128-bit register file, which is accessible by the test program. The non-critical path group and the critical path group are activated separately to control the activation probabilities of the non-critical paths and critical paths independently. This is achieved by setting two different 8-bit toggling-rate-control registers. These registers are controlled by corresponding toggling-enable bits. Each path group is connected to one toggle flip-flop, which is used as the input to the test pipeline as shown in Figure 5.8. This implies the paths in one group are controlled together i.e., all non-critical paths in a pipeline stage toggle at the same time, and all critical paths also toggle at the same time. The toggling rates of the flip-flops are programmable from 0.39% to 100% depending on the value of toggling-rate-control register. The toggling occurs when the toggling enable bit is set. If the toggling enable bit is cleared, the toggling rate becomes 0%. During the measurement, the activation probability of non-critical paths is fixed at 20%. This implies the toggling flip-flop associated with the non-critical paths changes value once at every 10 clock cycles resulting in 20% activation probability. Note 20% activation probability means that there is a 20% chance that any non-critical path is activated per cycle. The activation rate of the

toggling flip-flop associated with the critical paths i.e., the critical path activation probability (P_C) was varied using SPI slave from 0% to 100%.

To detect the malfunction of the pipelines, the reference pipelines with MSFFs and short delay paths are also implemented. The reference pipelines generate the correct output values for all (non-critical + critical) the paths. The final values of the pipelines are compared with the reference value and the number of errors is counted by the error counter whose value is accessible from the control program through SPI slave.

To measure the maximum operating frequency or the minimum voltage range, the error counter is monitored while changing the input clock frequency or the input voltage. The time-borrowing detection (TD) counter is used to count the number of the clock-stretching events to calculate the effective frequency and observe the time-borrowing probability. The time-borrowing probability is same as the critical path activation probability (P_C). To calculate the effective frequency, the pipeline operates in one-time operation mode (i.e., only during a pre-determined clock cycles). After the test starts the pipeline operates for 2^{16} clock cycles. The effective frequency and P_C can be calculated with the total operation clock cycles and the value of the TD counter [P_C = (TD counter value)/2^{16}].

The test environment is shown in Figure 5.10. The measurements are done with two scenarios. The first scenario is to fix the supply voltage and vary the input clock frequency. From this scenario, the achievable maximum operating frequency of the test circuit with the proposed methodology can be measured. The second scenario is to fix the input clock frequency and vary the supply voltage. From this measurement, it can be observed whether the proposed method can increase the range of operating voltage of the circuits. All the measurements are done for the reference and the test pipeline with MSFF and LTDs. In addition, the test pipeline was verified with the 4-phase clock pulses (4P) and the 8-phase clock pulses (8P). Table 5.1 summarizes the area and the power of different components required to implement the proposed system.
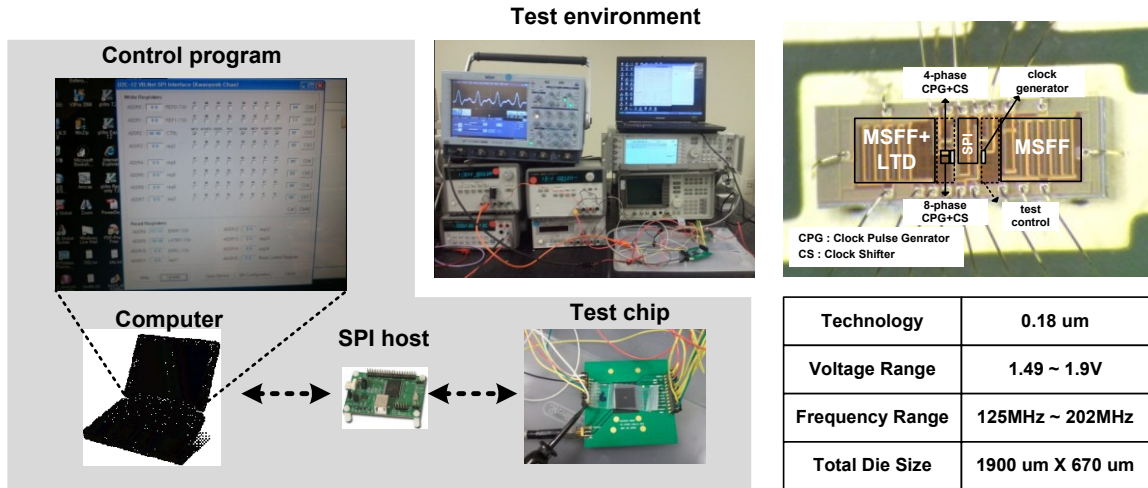
Figure 5.10: The test environment and the die-photo of the test chip.

Table 5.1: Area and power of the components.

Cell	Size	Power
MSFF	22um x7um	35.68 uW
LTD	26um x7um	36.8 uW
TDC	15um x7um	4.5 uW
8P CPG+CS	41um x63um	295.4 uW
4P CPG+CS	41um x35um	177.3 uW

* Simulation @ 1.8V and 200MHz

5.2.3.1 *Increased clock frequency at the fixed supply voltage*

Figure 5.11 shows the measured *maximum input clock frequency* that can be applied to the test system without causing any functional failure. To perform this measurement, the frequency of the input clock is increased till the first timing failure appears. The above experiment measures the T_{CK} defined in equation (1) for a given voltage with different values of T_{BW}. Note that T_{CK} is independent of the critical path activation probability (as long as $P_c > 0$) as the timing failure occurs if the critical path gets activated even once. However, during the measurements P_c was kept at 0.1. It is

crucial to note that the clock frequency in Figure 5.11 is *not* the *effective frequency* defined in the equation (3) which depends on the activation probability of the critical paths. The measured average performance of the conventional circuit (the pipeline with MSFFs) was 166.04MHz. The proposed methodology with the 8-phase clock or 4-phase clock increased the maximum input clock frequency up to 182.71MHz (10.04% increase) and 199.17MHz (19.95% increase), respectively. Theoretically, the 4-phase (4P) case should allow the system to operate at a 25% higher T_{CK} as $T_{BW}=0.25T_{CK}$. Likewise, with the 8-phase (8P) case, ideally the input frequency can be increased by 12.5% from the conventional case, without causing any timing error. The deviation of the measurement results from the ideal values is due to the non-idealities in the duty of the pulsed clock which resulted in a reduced pulse width and hence, a reduced T_{BW} and lower improvements in the maximum input clock frequency.
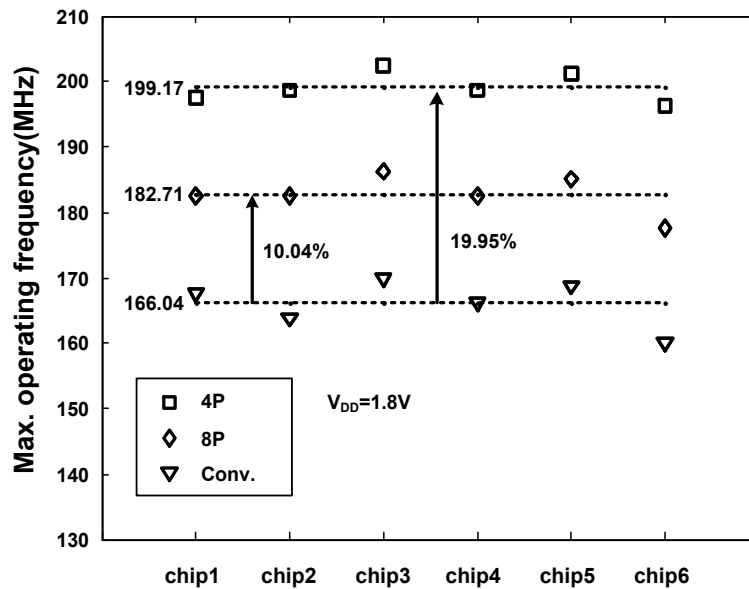
Figure 5.11: Measured maximum input clock frequency (No errors, V_{DD}=1.8V).

With the sample chip6, power consumption is measured for different input clock frequency as shown in Figure 5.12. The supply voltage was set to 1.8V and P_C was

programmed to at 0.1 (as measured by TD counter). Around 156MHz input clock, the frequency safety margin of the conventional circuit is eliminated and the circuit fails. Since time-borrowing and the clock stretching starts working, the proposed circuit operates with a faster clock but consumes more power. The CPG and the CS for the 4P case are implemented with smaller area than those for the 8P case. Consequently, the 8P case has higher power overhead than the 4P case at the same supply voltage and the clock frequency. In addition, the 4P case operates at higher frequency than the 8P due to wider time-borrowing window. Therefore, the proposed method can improve the performance beyond what is achievable by only removing the safety margin in a conventional design (i.e., wider operating frequency range).
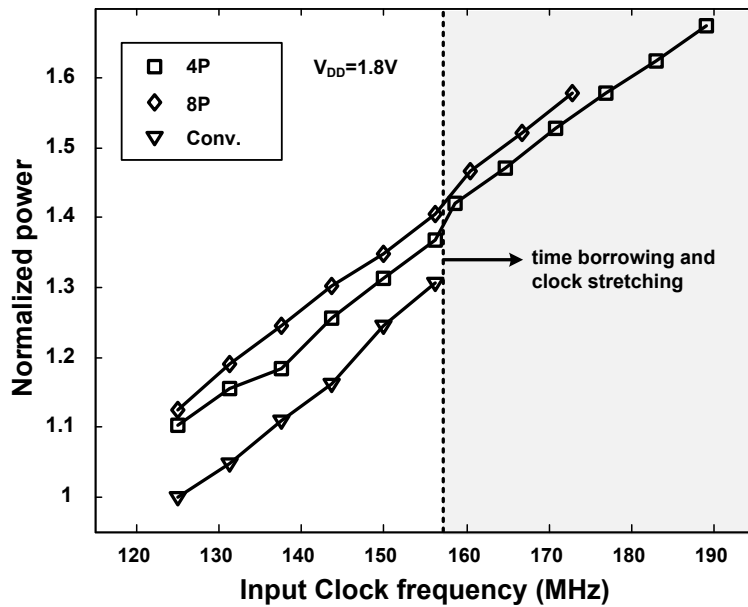
Figure 5.12: The measured frequency and the power of chip6 (V_{DD}=1.8V, P_C=0.1).

Figure 5.13 shows the measurement result of effective frequency for different Pc. During measurements, the same activation probability is used for the 4P and the 8P case to directly compare the performance of the 4P and 8P cases at different P_C. Further, during the measurements, the input clock frequency for the 4P, the 8P, and the

conventional cases were fixed at their respective "maximum input clock frequency" as noted in Figure 5.13. The effective frequency is calculated from the input clock frequency and the value of the TD counter. The trend shows that the proposed design outperforms the conventional design for $P_C < 0.9$ and the benefit increases at lower P_C. Theoretically, the proposed method should have the same performance as the conventional design at $P_C=1$. However, due to the non-ideal clock duty the proposed design is slower than the conventional case at $P_C=0.1$. During the preceding measurements, the input clock frequencies for the 4P case was higher than the 8P case i.e., $T_{min\_8P} = (1.25/1.125)T_{min\_4P}$ $= 1.11T_{min\_4P}$. But the stretched clock period (i.e., T_{max}) after time borrowing is the same for the 4P and the 8P cases as $1.25T_{min\_4P} = (1.25/1.11) T_{min\_8P} = 1.125T_{min\_8P}$. Therefore, at $P_c=1$, the two designs ideally have same effective frequency but for $P_C < 1$, the 4P design has higher effective frequency than the 8P case.

The relative difference between the effective frequencies of the 4P and the 8P case can vary from the observations in Figure 5.13. For example, when same input clock frequency is applied to both cases (i.e., $T_{min\_4P} = T_{min\_8P}$), the 4P case will have lower effective frequency than the 8P case as long as $P_c > 0$. This is because the clock period for non-critical transitions remains the same, but the increase (penalty) in the clock period for each time-borrowing event is larger for the 4P case than the 8P case. The difference in the effective frequencies of the 4P and the 8P case can also be due to differences in the critical path activation probability. Note that for a given design and input patterns, the number of 'critical' paths (i.e., paths with time-borrowing detection latches) in the 8P case will be less than the 4P case. Consequently, the time-borrowing event for the 8P case will be less than the 4P case potentially resulting in higher effective frequency of the 8P case than the 4P case. For example, based on Figure 5.13, the effective frequency of the 8P design operating at $P_c=0.1$ can be higher than the effective frequency of the 4P design operating at $P_c>0.5$. Such scenarios are a strong function of the path delay distribution of the design and the activation probabilities of different paths.
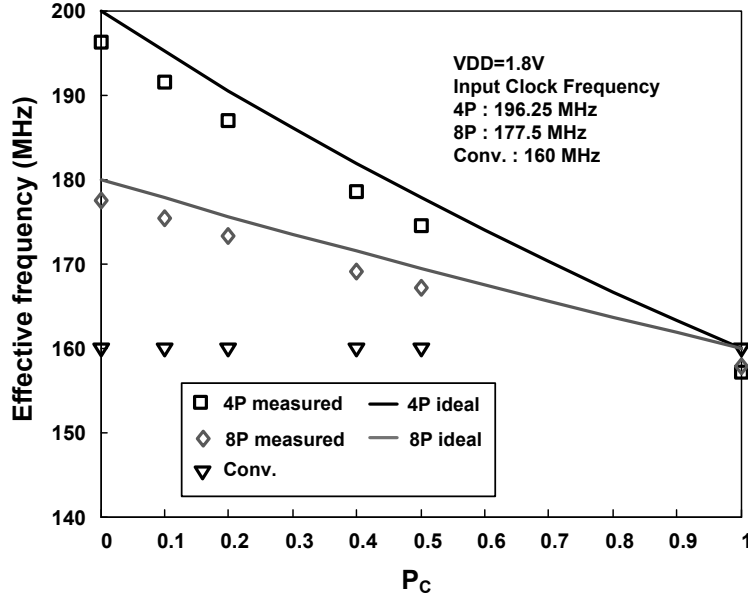
Figure 5.13: Measured performance of chip6 according to P_C.

5.2.3.2 *Reduced supply voltage at the fixed input frequency*

With the same clock frequency, the minimum operating voltage for test circuits were measured while reducing the supply voltage until the first timing error is found (Figure 5.14). As expected, the 4P case could operate at lower supply voltage (~1.51V) than the 8P (~1.65V) case. The average voltage for the conventional design without errors was 1.76V. The measurement results show that the proposed method could operate at a lower supply voltage (i.e., over a wider supply range). The effective performance and power of the design at this first failure point (i.e., at the minimum operating voltage) is summarized in the Table 5.2 (for the chip 6 only with P_C=0.1). The performance penalty of the 8P case and the 4P case are observed to be 1.25% and 2.4%, respectively. The 8P case has lower performance penalty than due to lower clock stretching amount than the 4P case. The measured power at the minimum operating voltage is reduced by 13% and 25% in the 8P and 4P cases, respectively. Finally, compared to the conventional design,

the 4P and 8P cases achieved 31% and 14% better performance per power (defined as frequency/power), respectively.
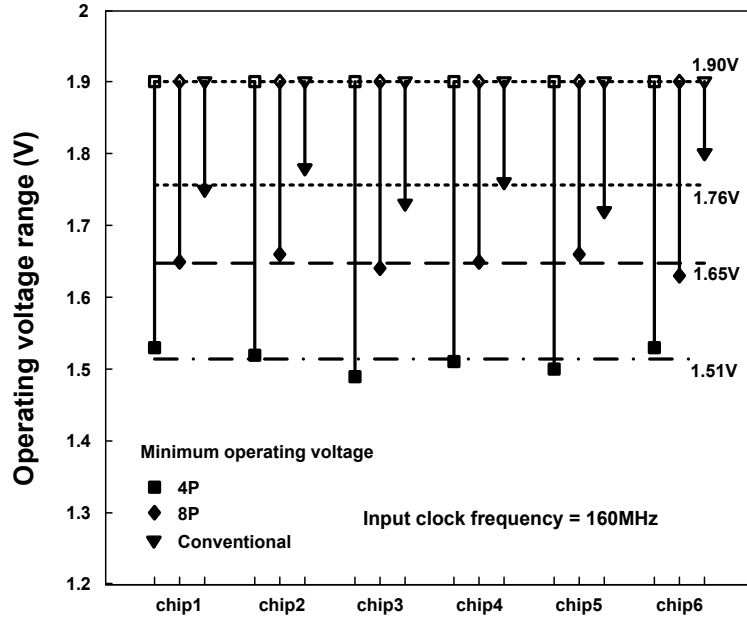
Figure 5.14: Measured operating voltage ranges of test chips at 160MHz input clock frequency.

Table 5.2: Normalized performance and power of the chip6 at the minimum operating voltage.

	Input Freq.	Min. V_{DD} (V)	Effective Frequency (P_C=0.1)	Power*	Performance per Power (Frequency/Power)
Conv.		1.80	1	1	1
8P	160 MHz	1.63	0.99	0.87	1.14
4P		1.53	0.98	0.75	1.31

* The power measurements includes the overheads

5.2.3.3 *Increasing tolerance to dynamic delay variations*

The ability of the design to tolerate dynamic variations in physical effects is demonstrated in the test-chip by reducing the supply voltage for a constant input frequency. The chip was tested under reduced dc voltage reduction. Since the test circuit

104

did not include supply noise injector, the case of fast voltage droops was not measured. Note the dc voltage reduction is a more stringent case as a time-borrowing event happens when critical path activation and dynamic variations occur at the same time. The slow or dc variations leads to higher probability of time-borrowing as they affect the system over a large number of cycles increasing the critical path activation events and hence performance penalty. On the other hand, the fast variations affect the delay only over a much shorter time interval. The measurements results can be generalized to suggest that the proposed technique implies better tolerance to dynamic variations in delay either due to critical path activation or due to environmental variations with the minimized performance penalty.

5.2.3.4   Waveforms of operation

Figure 5.15 demonstrates the dynamic change of the clock period. The measured waveform is the system clock output of the proposed circuit. The waveform shows that the system is operating at two different clock periods.
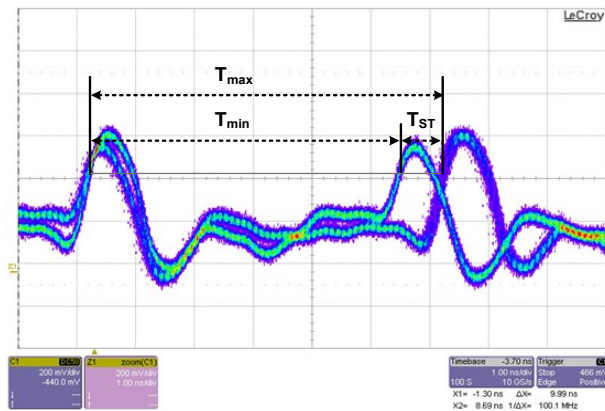
Figure 5.15: Measured system clock waveform for the 8P case.

5.2.3.5   *Power and area overheads*

The area overheads of the proposed method for 4P and 8P cases were 1.1% and 1.7%, respectively (Table 5.3). The measured power overhead of the proposed method for 4P and 8P was 4.56% and 7.38% when the activation probabilities of the non-critical paths and the critical paths are 0.2 and 0.1. Note the power values in Table 5.1 are simulated results (referred to as the simulated power), which describe the power of individual blocks. On the other hand, Table 5.3 reports the measured total circuit power (the CPG, the CS, the TDC, the LTDs, the MSFFs and logics) for 4P, 8P, and the conventional cases. The measured area and the power overheads are primarily due to the clock pulse generator and the clock shifter. As the area, complexity, and power of the pipeline increases, this overhead will reduce as power of the clock pulse generator and the clock shifter remains the same.

Table 5.3: Total area and measured power of the chip6.

	Phase	Total area (mm^2)	Total power (mW)
Conventional	-	0.198	4.61
Proposed	8P(Total)	0.201	4.95
	4P(Total)	0.200	4.82

* Measured @1.8V and 162.5 MHz clock input.

5.3   *Programmable-time-borrowing and delayed-clock-gating*

The error prevention (instead of correction) has been explored to reduce the overhead in the previous section. Timing errors in a pipeline due to supply noise can be prevented by borrowing time from the following stage and resolving the borrowed time by stretching/gating the next clock cycle. Though time-borrowing with clock stretching allows error prevention with the minimized performance penalty, the control delay from error detection to correction circuits limits the size/frequency of the pipeline.

This section presents a flexible error-prevention circuit – programmable-time-borrowing (PTB) – to prevent errors under supply noise in pipelines. The key novelty of the system is that it can be programmed to enable time borrowing over the multiple pipeline stages and clock gating after multiple cycles from the time-borrowing detection point. In addition, the proposed approach is a platform-independent solution, which can be applicable to any types of circuits, such as control circuits, state-machines, and circuits with feedback data paths. A test-chip is designed in 130nm CMOS technology to verify the effectiveness of the proposed approach considering time-borrowing over 1, 2 and 3 pipeline stages with 1, 2, and 3 cycle delayed clock gating, respectively. The potential of on-line programming of PTB to trade-off noise tolerance with performance penalty has been demonstrated.

5.3.1   Methodology

The proposed idea basically utilizes the concept of time-borrowing like the work in the previous section. The pulsed-latch with time-borrowing detection (PLTD [67]) circuit behaves like a normal flip-flop when the input data D is set before the rising edge of the pulsed clock as shown in Figure 5.16. If the input data D changes during high period of the pulsed clock, referred to as the time-borrowing window, the PLTD allows signal to propagate to the next stage. This event is referred to as a time-borrowing event.

Time-borrowing is inherent characteristics of pipelines design with pulsed latches. The noise tolerance is determined by the time-borrowing window. The PLTD includes additional circuits to detect whether signal transition occurred during the time-borrowing window and generate a time-borrowing detection (TB) signal. Assuming the cascaded pipeline stages have critical paths, TB signal is used to gate the clock cycle to resolve possible timing errors in the cascaded stages. The prior works on error prevention using time-borrowing always the *next* clock cycle after time-borrowing detection is controlled resulting in a constant performance penalty and noise tolerance for a given pulse width [71], [82]. Moreover, the delay of the feedback clock-control path between the time-borrowing detection and clock gating circuit is constrained by 1 clock cycle making the approach less suitable for large circuit blocks. The proposed system addresses this limitation by removing the nth clock pulse after the time-borrowing detection (n = 1, 2, or 3 in this work). Hence, the signal is allowed to propagate over multiple stages after time-borrowing detection before the clock gating is initiated. Figure 5.16 shows the case when n is 2.
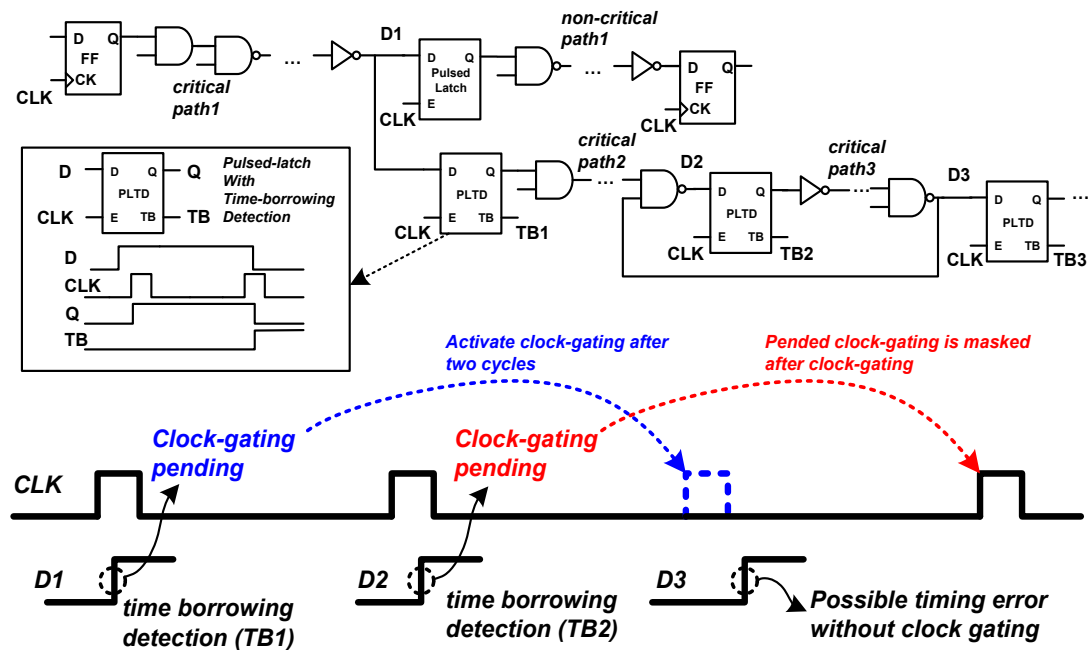
Figure 5.16: Programmable-time-borrowing and delayed-clock-gating.

108

To implement the PLTD, a pulsed latch with an additional flip-flop to detect time borrowing is used as shown in Figure 5.17 [68]. If a disparity between the pulsed latch and the flip-flop occurs, TB is set to notify time-borrowing event. If a time-borrowing event occurs, it propagates though the cascaded critical paths until the time slack is resolved by the clock gating. The time-borrowing detection (TB) signals are propagated to a clock gating (CG) circuit through a PTB detection network (PTDN$_n$ where 'n' indicates clock is gated after 'n' cycles after a time borrowing detection). In PTDN$_1$, clock is gated at the next cycle after the time borrowing detection. In PTDN$_3$, the time-borrowing window is shared across 3 pipelined stages, and CKEN becomes low 3-cycle after the detection. The CG circuit gates the clock when CKEN is low and re-activates the next clock pulse $i.e.$, the clock is gated after 3-cycle. In PTDN$_3$, once CKEN becomes low, time borrowing detection signals are masked for 2-cycle to cancel the pending time-borrowing detections in the PTDN since clock gating resolves the borrowed time in the pipelines. However, metastability does not occur in data paths since pulsed-latches are used in data paths. The time-borrowing detection signal (TB) can have metastability, but the multiple pipeline stages (1~3 stages) and convergence time (1~3 cycles) in PTDN and CG circuits help reduce the possibility of metastability in the control path. Fundamentally, the metastability cannot be eliminated but only can be reduced adding more flip-flops or increasing convergence time.

The proposed methodology has four key benefits. *First*, a system with PTDN$_1$, PTDN$_2$, or PTDN$_3$ (i.e., PTB mode: PTB method with PTDN$_n$) allows on-line trade-off between noise tolerance and performance penalty even with a single time-borrowing window. A higher value of n implies less performance penalty per time-borrowing event but also less noise tolerance as the single time-borrowing window is shared across multiple stages. Hence, each PTB mode can have different performance penalty and noise tolerance. *Second,* PTB relaxes the control-delay requirement - PTDN$_1$ has 1-cycle control delay requirement while PTDN$_3$ has 3-cycle constraints. The system can be

designed with the appropriate PTB mode depending on the size/ frequency of the pipeline. *Third*, a system with $PTDN_1$, $PTDN_2$, or $PTDN_3$ guarantees minimum performance since the performance penalty saturates at the worst case scenario since pended time-borrowing events can be canceled for multiple cycles. *Fourth*, the proposed solution is applicable to general pipelines including state machines and circuits with feedbacks.
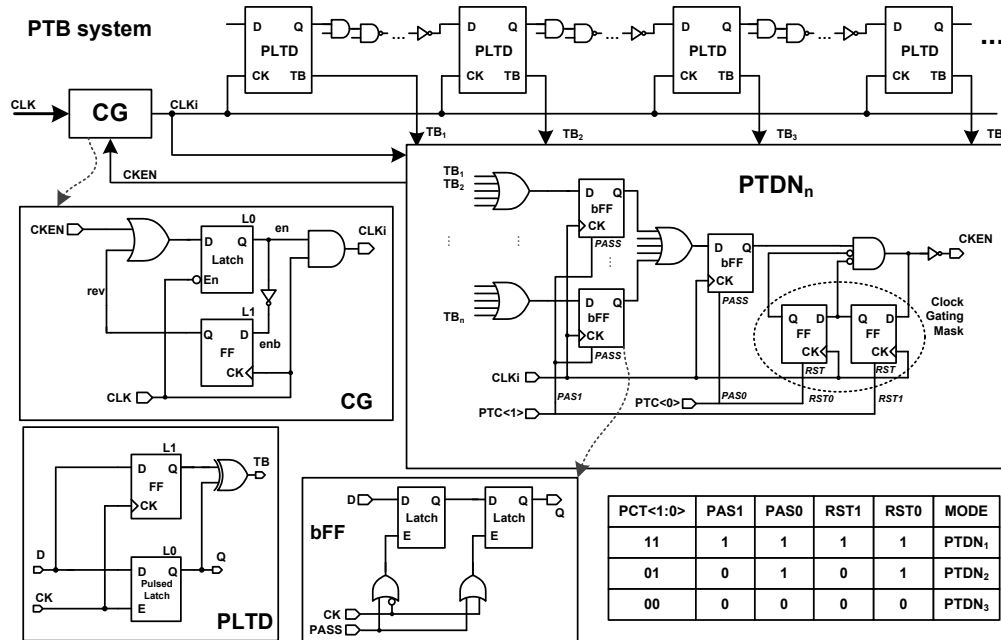
Figure 5.17: The overall architecture of a pipeline with the proposed programmable time borrowing with delayed clock gating.

5.3.2 Test chip and measurement results

To verify the proposed method, a test-chip including test pipelines, control circuits, and a noise injector circuit is designed in 130nm CMOS as in Figure 5.18. In addition, a clock modulator to change the input clock frequency (CKp) in response to the global noise [83] is integrated. Simple five-stage pipelines (Figure 5.17) are implemented with cascaded critical paths considering worst case timing scenario (i.e., the input changes every cycle). The noise injector is comprised of nMOS transistors, which draw

instantaneous current from the power supply and incur voltage noises in the supply when an enable pulse is applied as shown in Figure 5.18. The VCO generates CKIN, which is used for the input clock to the clock pulse generator for the test system clock. The frequency of the VCO is controlled by the external VCO control voltage (V_{REF}). Figure 5.19 shows the die-photo of the test-chip. Figure 5.20 shows the operational waveforms of the proposed methodology. When the supply noise is injected, clock pulse is gated after one, two, or three cycles for PTB1, PTB2, or PTB3 case, respectively. The clock pulse with approximately 625ps high pulse width is generated from the clock modulator.
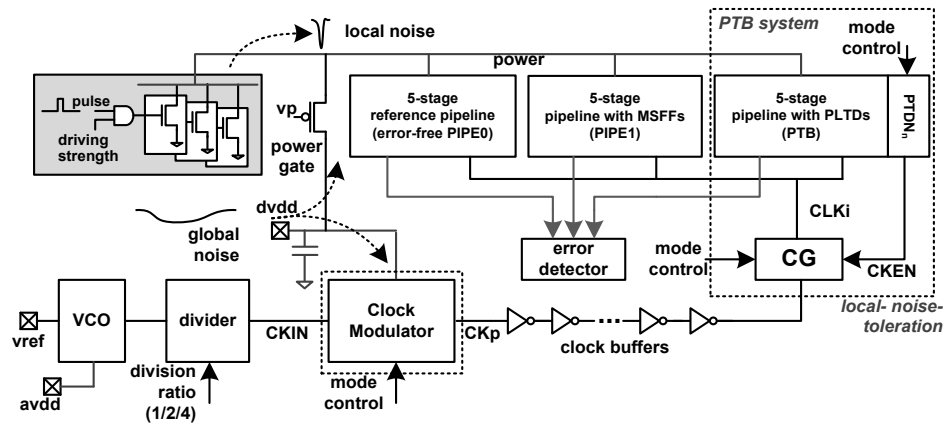
Figure 5.18: The architecture of the test-chip.

Technology		130nm
Voltage		0.71V~1.15V
PTB	Area	8484 µm²
	Area Overhead	11.87% (PTB path only)*
	Power	598.4 µW @1.1V 200MHz
	Power Overhead	12.32% (PTB path only)*
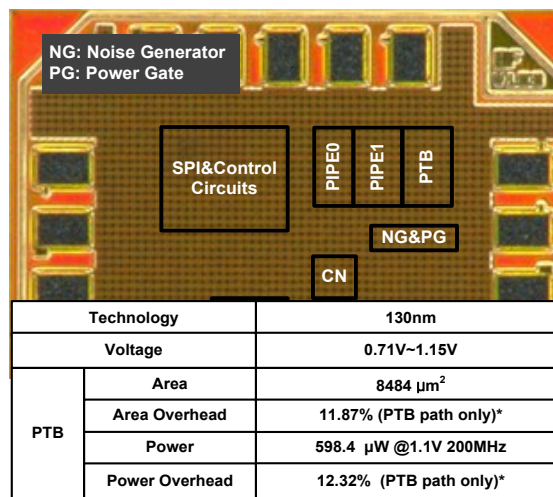
As a design size increases, overheads decrease since PLTDs&PTDN are used only in cascaded critical paths

Figure 5.19: The die-photo of the test-chip and key design features.
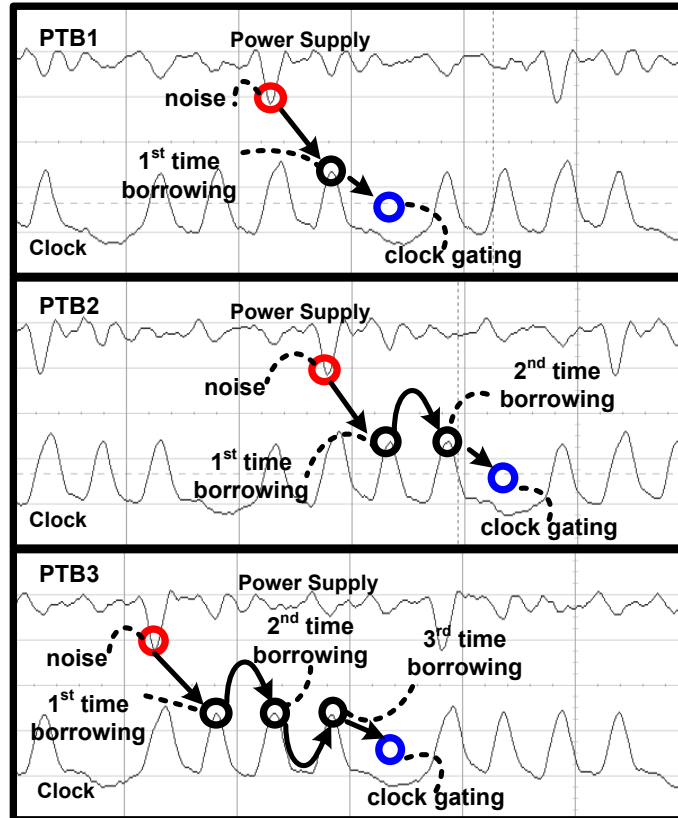
Figure 5.20: Measured operational waveforms of the proposed method.

5.3.2.1 *Effect of DC voltage noise*

Figure 5.21 shows the DC operating voltage range of the test pipeline with master-slave flip-flops (PIPE1) and PTB at reduced voltage (DC noise). The measurements of the point of the first failure (PoFF) indicate that PTB1 (PTB method with $PTDN_1$) has the highest DC noise tolerance. The error probability was measured with an error counter implemented in the test block while reducing the supply voltage. The effective frequency was measured utilizing frequency counter, which counts the number of the clock edges during a pre-determined time period (i.e., the time period is controlled by an external test clock). The effective frequency with PTB1 drops to 133MHz under DC noise shift. PTB3 can improve the effective performance to 160MHz. Hence, Figure 5.21 demonstrates the ability of PTB to trade-off noise tolerance and

effective frequency. As shown in Figure 5.21, PTB3 can tolerate less DC noise then PTB1 or PTB2 since the time-borrowing window is shared across three pipeline stages. On the other hand, PTB3 shows lower performance penalty than PTB1 or PTB2. PTB3 removes clock pulse three cycles after the time borrowing detection as shown in Figure 5.20. Thus, pending time borrowing detections in the PTDN3 can be neglected after the clock gating (i.e., all timing slacks in the pipelines can be resolved by clock gating). As a result, PTB3 can have lower performance penalty. The measurement results are when the activation probability of the critical paths (PC) are 100% considering the worst case scenario. The performance penalty will reduce as PC reduces. The measurement results prove that the proposed method always guarantees the minimum performance of the pipeline system unlike the error detection and correction methodology.
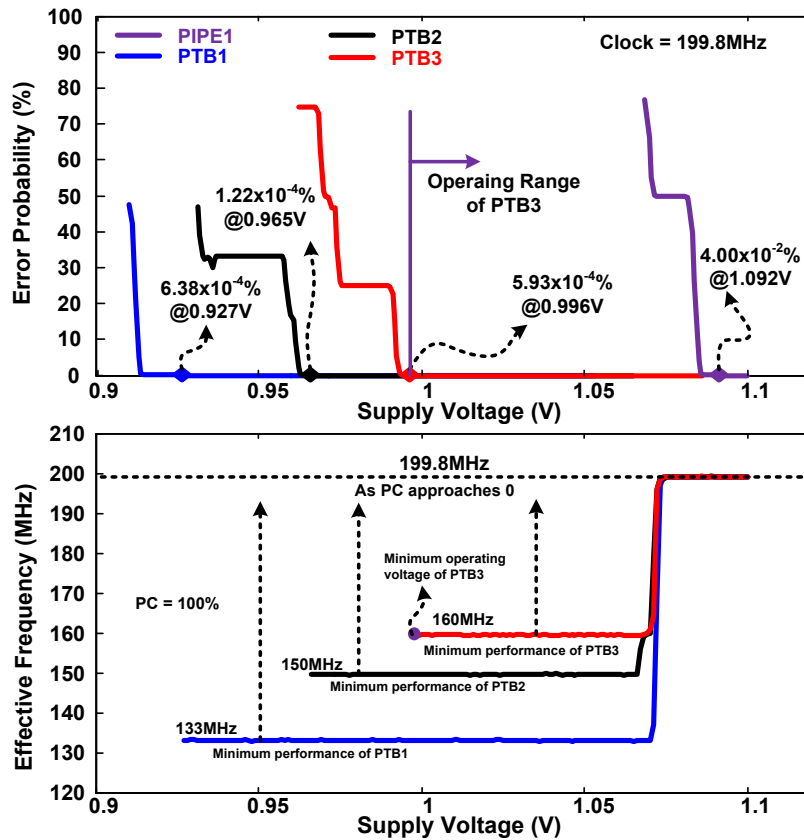
Figure 5.21: Measured error rate and effective frequency of the test pipelines under DC voltage shift/noise.

5.3.2.2   *Effect of AC voltage noise*

Figure 5.22 shows the operation of PTB under transient local noise. When the noise is injected every clock cycle, the measured effective frequencies for PTB1, PTB2, and PTB3 are 133, 150, and 160 MHz, respectively. For the $PTDN_3$ case, the performance penalty is constant for the noise injection ratio of 1 to 1/4 as the clock is gated once in every 5 cycles causing pending time-borrowing events to be canceled with clock gating. It implies PTB3 has less performance penalty for frequent noise but has less noise tolerance than PTB1 or PTB2. At points A and B in Figure 5.21, the effective noise injection ratio becomes 1/6 and 1/4 although the controlled noise injection ratios are 1/3 and 1/2, respectively. It happens as noise during the clock gating period does not cause time borrowing as shown in Figure 5.23. In other words, the injected noise during the clock gating event can be invalidated. As a result, the proposed system can show better performance than expected at a certain noise injection frequencies (i.e., lower effective noise frequency then the injected noise frequency).
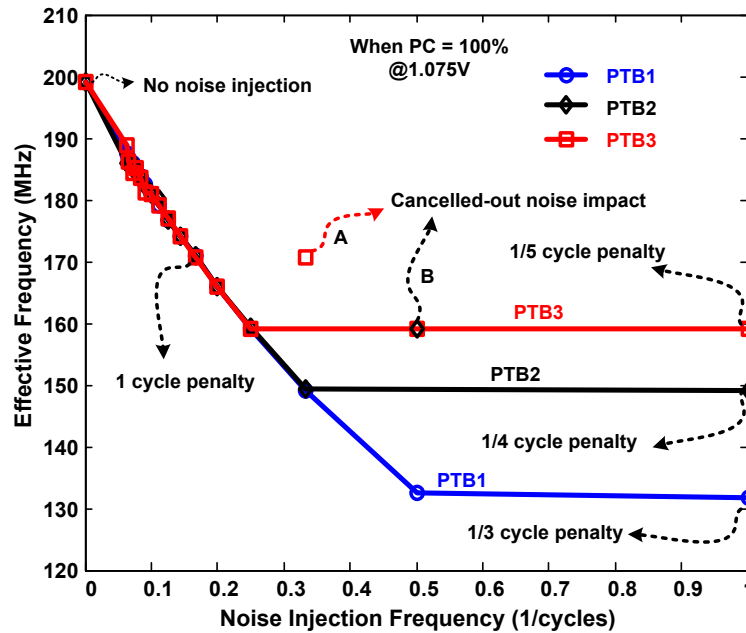
Figure 5.22: Measured effective frequency of the test pipeline only with PTB under local noise injection.

Noise Frequency = 1/1

VDD

noise

ignore pending time-borrowing events

CLKi

gating

1 clock gating per 5 cycles

Noise Frequency = 1/2

VDD

noise

ignore pending time-borrowing events

CLKi

gating

1 clock gating per 5 cycles

Noise Frequency = 1/3

VDD

noise

injected noise during clock gating is invalidated

Effective Noise Frequency = 1/6

CLKi

gating

1 clock gating per 7 cycles

Noise Frequency = 1/4

VDD

noise

CLKi

gating

1 clock gating per 5 cycles

Noise Frequency = 1/5

VDD

noise

CLKi

gating

1 clock gating per 6 cycles

Noise Frequency = 1/6

VDD

noise

CLKi

gating

1 clock gating per 7 cycles

Figure 5.23: Noise cancel-out effect of the PTB3.

The noise tolerance of the PTB is measured with DC noise and AC noise injection as in Figure 5.26. While injecting AC noise up to 130mV, changed DC noise level from the power supply utilizing general purpose interface bus (GPIB). In the measurement, DC noise implies possible IR drop or voltage regulator offset. AC noise emulates the transient local voltage noise due to the instantaneous current. Measurement results demonstrate that the pipeline with the proposed method can give good noise tolerance with the minimized performance penalty. In the presence of 130mV local noise, using only PTB, 125mV~196mV global noise can be tolerated. However, the main contribution of this work is to relax the control time requirement up to three clock cycles while achieving supply noise tolerance. The measured area and power overheads of the test chip were

11.87% and 12.32%, respectively. However, remember that the implemented test case just include 5-stage pipelines only with cascaded critical paths.

5.3.2.3 *Integration of PTB-DCG with adaptive clocking*

The noise tolerance of the pieline can be further improved by integrating PTB with an adaptive-clocking method [83]. The adaptive clocking uses a global clock modulator, as shown in Figure 5.24, to change the clock frequency in response to global supply noise [83]. The measrued output clock frequency of the clock modulator in response to the DC voltage shift is shown in Figure 5.24.
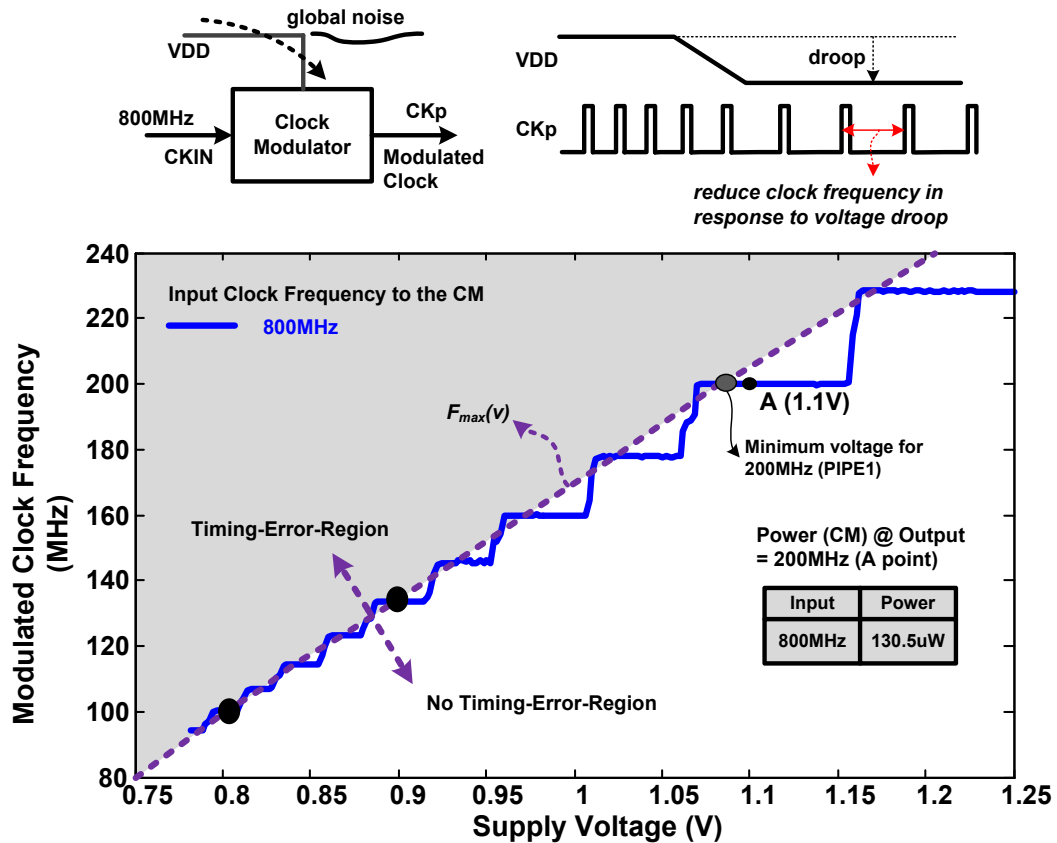
Figure 5.24: Measured output frequency of the clock modulator with DC voltage variations.

To verify the operation of the combined system, significant voltage droop was generated as shown in Figure 5.25. Figure 5.26 summarizes the noise tolerance of PTB without clock modultion and with clock modulation. The global noise tolerance was improved up to 405mV ~ 442mV using the combined system. Adaptive clocking helps improve the noise tolerance over what is achievable with PTB alone. Moreover, adaptve clocking proactively change the clock frequency in response to DC voltage drop. Hence, if there exists sustained global noise, instead of continuosly employing time-borrowing and clock gating, the combined system moves to a reduced frequency to prevent errors and decreases the energy and performance overhead.
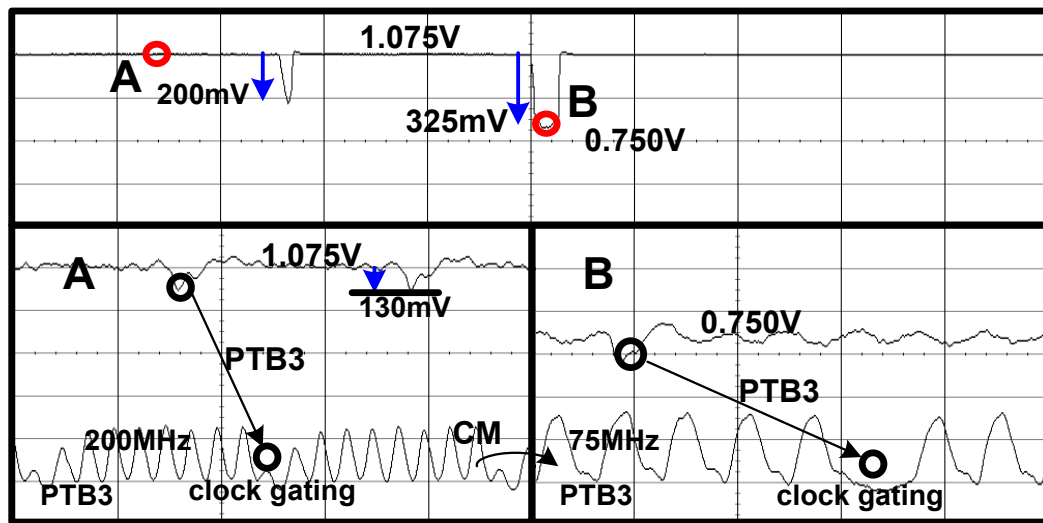
Figure 5.25: Measured output frequency of the clock modulator and PTB3 with DC voltage variations.

117
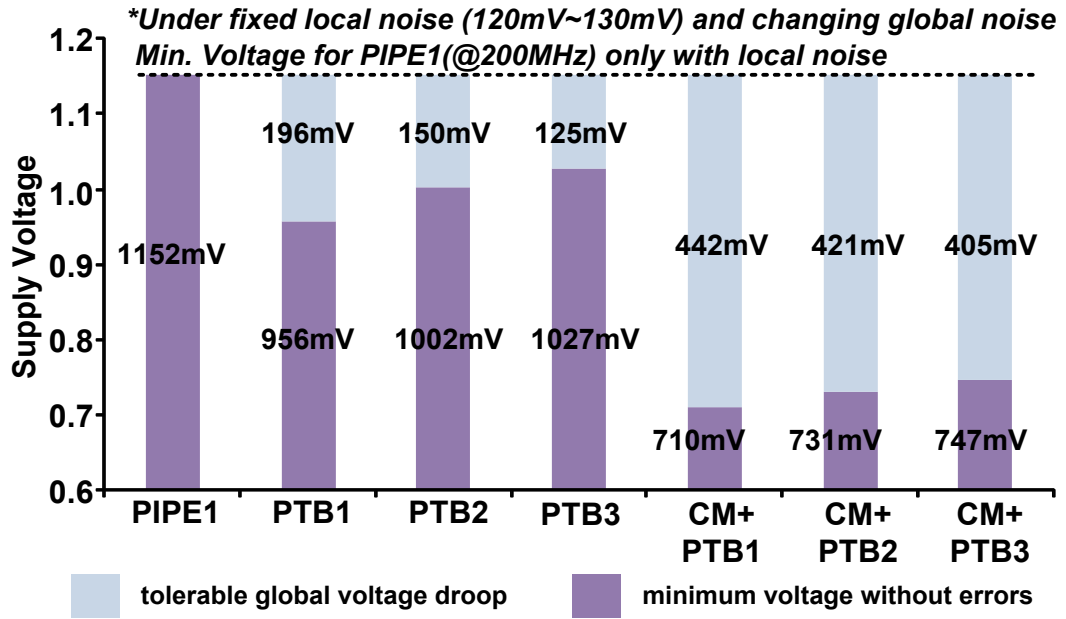
Figure 5.26: Measured tolerable noise ranges under DC and AC noise injection.

5.4 Case studies for overhead estimation

An automated design flow is developed to apply two proposed approaches to a large design and performed a case study for the overhead and the performance gain analysis. For this case analysis with the automated design flow, a rasterizer was chosen [84]. The rasterizer is an essential graphic processing unit, which converts a vector graphic format into a raster image on a video display or printer, or in a bitmap file. This section presents realistic area and power overheads based on the real hardware implementation.

5.4.1 Case study for TB–CS

An automated design flow is developed and applied to implement the rasterizer with the proposed TB-CS technique. The rasterizer was implemented with an 180nm CMOS technology. To reduce the performance overhead, LTDs are used only in the cascaded critical timing paths. If the next stage has enough timing slack to resolve the borrowed time from the previous stage, only pulsed-latches can be used. The developed design flow is shown in Figure 5.27. First, after the place and route of the synthesized design and the timing analysis, the list of FFs in critical paths is generated. Then, the FFs in critical paths are replaced with the pulsed-latches. Second, from the timing report from the replaced pulsed-latches, the list of cascaded critical paths is generated. Then, pulsed-latches in cascaded critical paths are replaced with LTDs. The automated layout shown in Figure 5.28 is generated using the design flow, and the locations of the LTDs and pulsed flip-flops are shown.
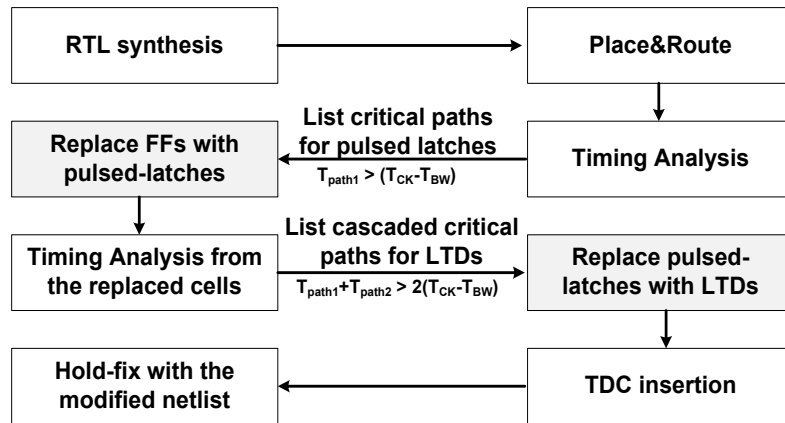
Figure 5.27: Design flow for inserting pulsed-latches and LTDs.
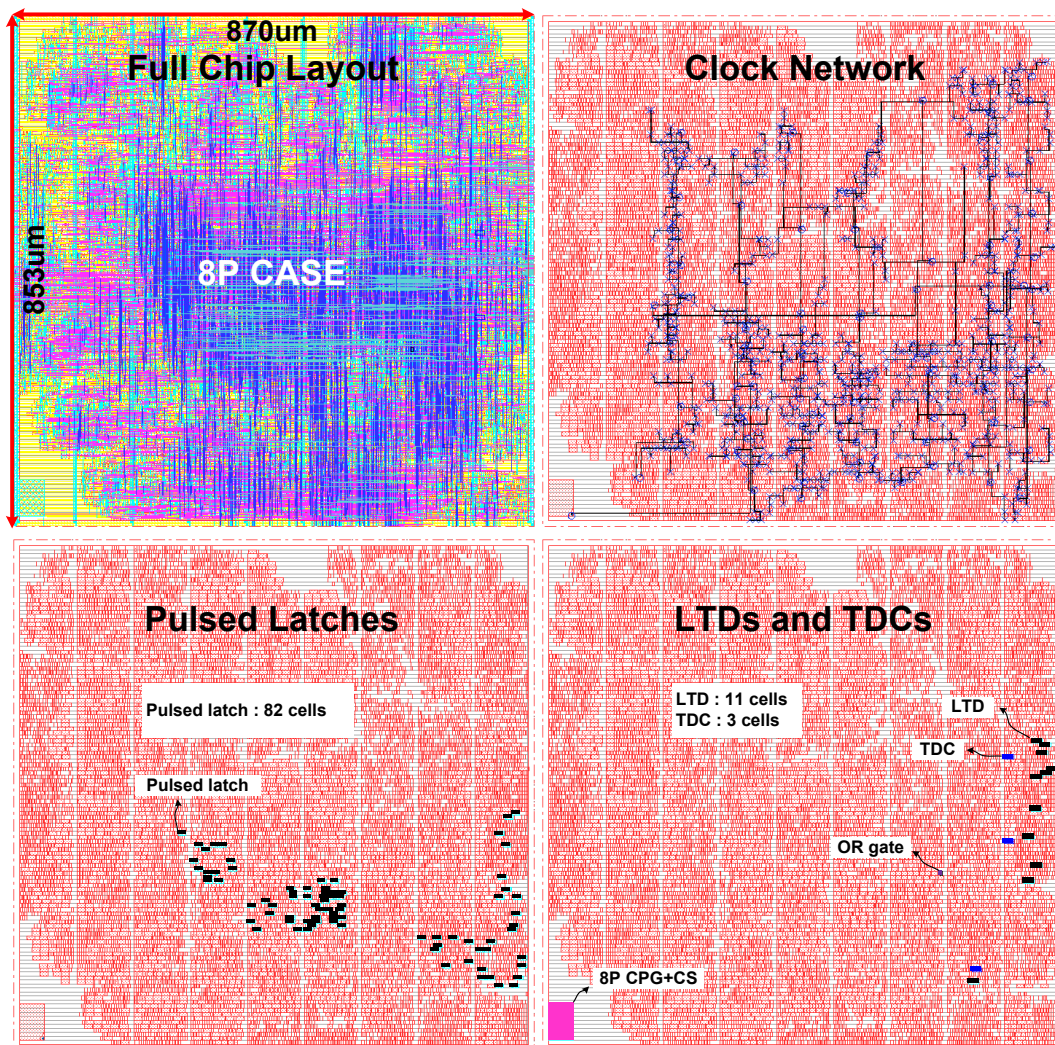
Figure 5.28: The layout of the implemented graphic processing unit with 8P case with an 180nm CMOS technology.

Figure 5.29(a) shows the path-delay distribution of the rasterizer. Critical paths are highly populated close to the target delay. To find the flip-flops, which are candidates for replacements, the delay distribution of most critical paths for each flip-flop is evaluated. Depending on the time-borrowing window, the flip-flops, which have long delay paths as input, are selected to be replaced to pulsed latches. This is illustrated in Figure 5.29(b), 93 and 155 flip-flops are chosen to be replaced by pulsed latches for the 8P and the 4P case, respectively. However, only a fraction of these pulsed latches are replaced by LTDs depending on whether any path originating from that pulsed latch terminates in another pulsed latch. This is performed by elaborating all the output paths from each flip-flop, evaluating their delay, and finding whether it has any output path with a delay higher than the critical delay. Figure 5.30(a) shows the distribution of the worst-case path delays from all of the pulsed latches selected in Figure 5.29(b) for the 4P case. Only the pulsed latches with the worst-case output path delay higher than T_{min} are selected to be replaced by LTDs. Figure 5.30(b) shows the same analysis for the 8P case. Figure 5.29 clearly illustrates that only a small fraction of the flip-flops are replaced by the pulsed latches and LTDs. The major overhead of the proposed approach comes from the need for hold fixing. Since the critical path includes convergent short-delay paths, hold-fix buffers should be inserted in short-delay paths to avoid hold-timing violation. This is illustrated in Figure 5.31, which shows the distribution of delay of all input paths of an example critical flip-flop (a pulsed latch or a LTD). The paths whose delay is less than the time-borrowing window require hold-fixing and hence, incur additional area/power overhead. The numbers of such paths are higher for the 4P case due to the larger T_{BW}.
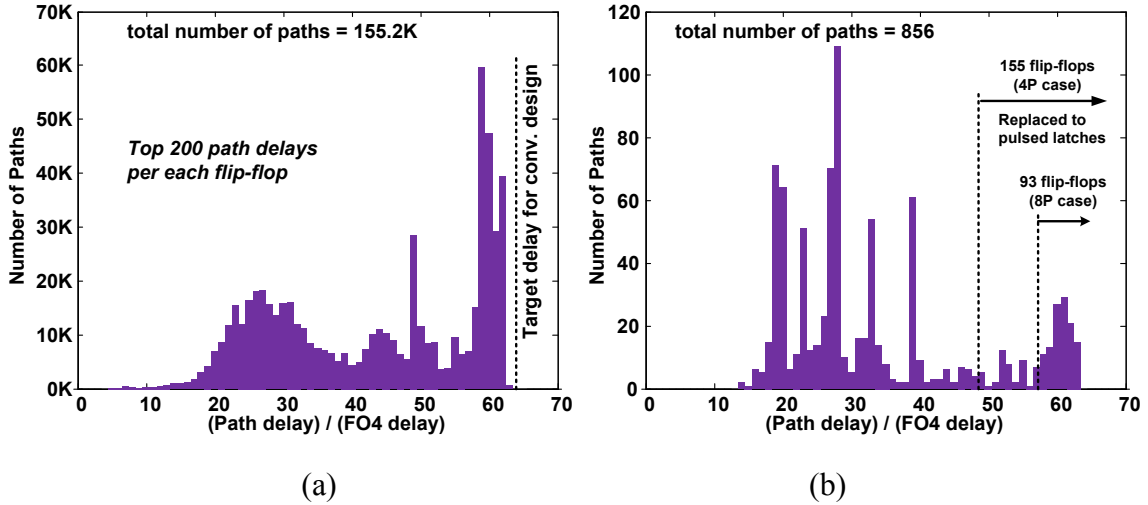
Figure 5.29: The path delay analysis of the rasterizer with an 180nm CMOS technology: (a) distribution of all path delays; (b) the worst path delay per each flip-flop showing the flip-flops that are selected to be replaced by pulsed latches.
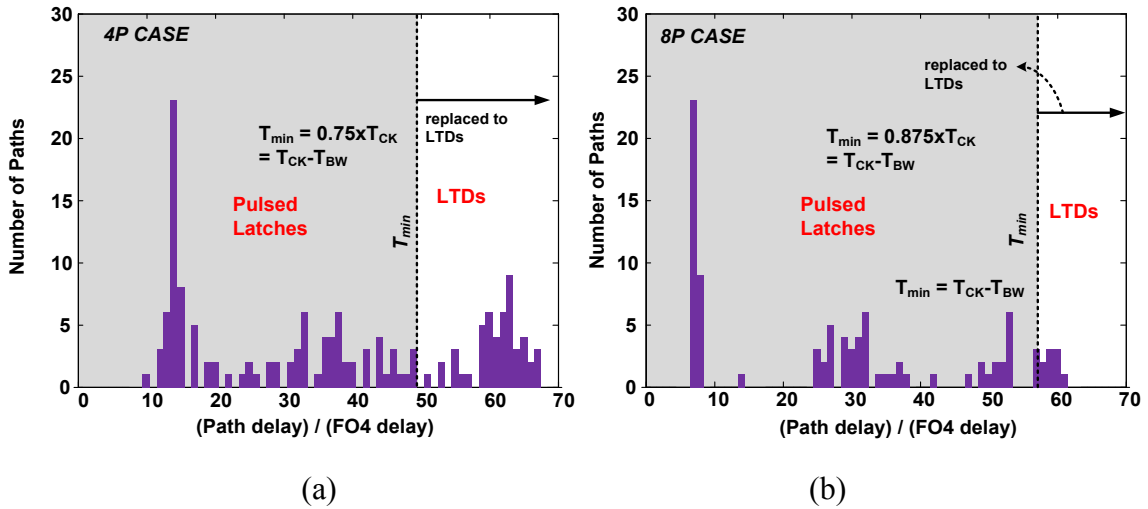
Figure 5.30: The distribution of the worst-case output path delays of all the pulsed latches for the (a) the 4P case and (b) the 8P case showing the ones that will be replaced by LTDs.
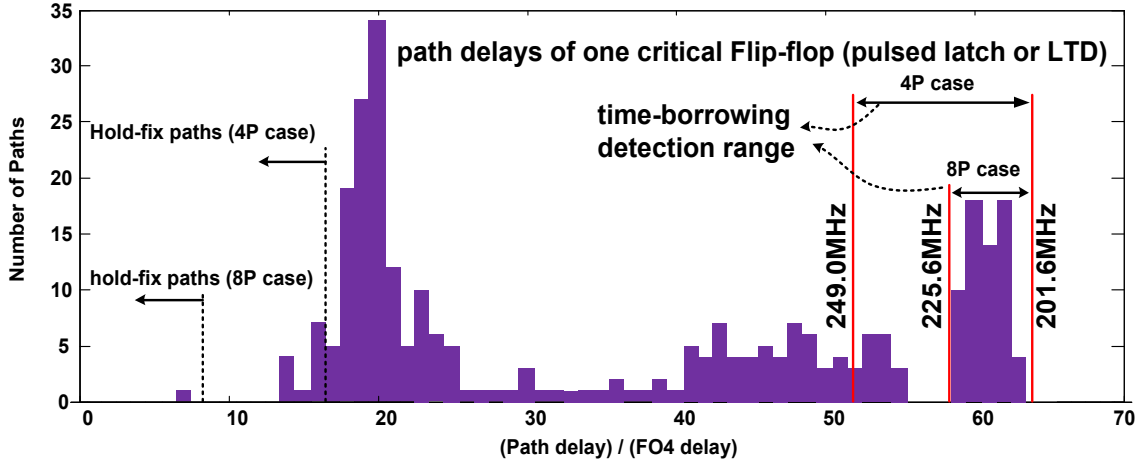
Figure 5.31: Distribution of the delay of the input path of one critical flip-flop showing the need for hold fixing in certain paths.

Table 5.4 summarizes the result of the proposed design. In the implemented rasterizer, 12.7% and 9.6% FFs were replaced with pulsed-latch and 5.4% and 1.3% were replaced with LTDs for the 4P and the 8P case, respectively. The overhead due to additional circuits for the proposed technique reduced as the design size is larger, and the overhead due to the hold-fix buffers became dominant (Table 5.4). The 4P case and the 8P case improved the performance per power by 35% and 19%, respectively. The proposed technique extended the operating frequency range of the rasterizer. This is shown in

Table 5.5. P_C was measured with different test vectors (vector1~vector3) with the maximum possible input clock frequency. The effective frequency was calculated with P_C and input clock frequency. With these different test vectors, P_C was measured at the maximum input clock frequency without errors as shown in 3rd, 4th, and 5th rows of

Table 5.5. The effective frequencies (F_{EFF}) are smallest with vector1 and vector2 for the 8P case and the 4P case, respectively. With the same vector, the 8P case showed much smaller probability of clock-stretching event than the 4P case since the number of LTDs in the 8P case is smaller than that in the 4P case. The maximum input clock frequency of the 8P case is lower than that of the 4P case.

Table 5.4: Summary of implemented 3D graphic processing unit.
(@ 1.8V and 201.6 MHz)

	MSFF	8P	4P
FF	856 (100%)	763 (89.1%)	701 (81.9%)
Pulsed-latch	0 (0%)	82 (9.6%)	109 (12.7%)
LTD	0 (0%)	11 (1.3%)	46 (5.4%)
CPG+CS	0	1 (8P)	1 (4P)
TDC	0	3	12
# of hold-fix buffers	179	765	1708
Area (overhead)	436547.3 um^2	448638.8 um^2 (+2.77%)	470485.0 um^2 (+7.78%)
Power (overhead)	41.63mW @1.8V, 201.6MHz	42.88mW (+3.00%) @1.8V, 201.6MHz	43.46mW (+4.40%) @1.8V, 201.6MHz
Performance per power	1 @1.8V, 201.6MHz	1.19 @1.65V, 201.6MHz	1.35 @1.55V, 201.6MHz

(*) estimated from spice simulation considering the vector1.

Table 5.5: Simulated maximum input clock frequency and P_C.
(@ 1.8V and 201.6 MHz)

	MSFF	8P	4P
Max. input clock frequency	201.6 MHz @1.8V	225.6 MHz (+11.9%) @1.8V	249.0MHz (+23.5%) @1.8V
P_C (vector1)	-	0.68%	7.83%
P_C (vector2)	-	0.04%	9.02%
P_C (vector3)	-	0.02%	6.18%
Min. $Feff$	201.6 MHz	225.4 MHz (+11.8%)	243.5 MHz (+20.8%)

It is observed that the proposed technique will be beneficial for graphic processing units since graphic accelerators are not much heavily pipelined and have slower operating clock frequency (i.e., 200MHz~400MHz) in mobile processors. In addition, a low performance penalty can be expected in the graphic processing units since the possibility of critical patterns in arithmetic is generally low. It is interesting to note that the test-chip measurement shows a lower power overhead for the 4P case compared to the 8P case (Table 5.3) while the observation in Table 5.4 is opposite. This is because the test-chip was implemented with inverter chains to verify the basic concepts. In the

test-chip, the critical paths do not include convergent short-delay paths, and hence, there were no LTDs (or pulsed latches) that received input from the short paths. Consequently, hold-fix buffers were not required in the test-chip. The higher overhead for the 8P case was due to the higher complexity of the pulse generator and the clock shifter. On the other hand, the path delay distribution shown in Figure 5.31 illustrates that hold fixing was required in the rasterizer design. A larger time-borrowing window in the 4P case resulted in an increased number of required buffers (Table 5.4 and Figure 5.31). Hence, the area/power overhead of the 4P case is observed to larger than the 8P case in Table 5.4. In general, for a moderate size design, the overhead can be higher for the 4P case due to the need for more hold-fix buffers. However, the power overhead will also depend on the switching activity in these short paths (i.e., activity of the additional buffers).

5.4.2 Case study for PTB–DCG

The PTB-DCG technique is also applied to the rasterizer with a Nangate 45nm technology model [85] (Figure 5.32). PTB1, PTB2, and PTB3 cases are implemented with the programmable PTDNn (n is 1, 2 or 3). Table 5.6 compares the baseline design (all MSFFs) with the PTDN1, PTDN2, and PTDN3 cases. To implement the PTDN1, the MSFFs in the baseline designs are selectively replaced by the pulsed latches and PLTDs. The basic approach is to keep MSFFs in the non-critical paths. When a critical path in one stage is followed by non-critical paths in the successive stage, the MSFF is replaced by a pulsed latch to allow time-borrowing. The borrowed time in the current stage is resolved by the inherent slack of the connected non-critical path(s) in the following stage. When a critical path is connected to another critical path in the following stage, the corresponding MSFF is replaced by a PLTD. The PTDN modes are programmable (PTDN1, PTDN2, or PTDN3 mode) and the PTB1 design can operate with PTDN1~PTDN3 modes. However, a programmable PTB1 design requires more number of PLTDs compared to a fixed PTB2 or PTB3 design. To understand the overhead

125

incurred to enable programmability, the PTB2 or PTB3 designs were also implemented directly. For PTB2 and PTB3 cases, PLTDs are inserted only if three and four critical paths are connected in successive stages, respectively. Hence, the number of PLTDs is less than the number of PLTDs in the PTB1 design. However, PTB2 can only work in PTDN2 or PTDN3 modes, and PTB3 can only work in PTDN3 mode. The overheads are primarily determined by the number of hold-fix buffers. The choice between the different design cases in the Table 5.6 depends on the design size, number of critical paths and clock frequency.
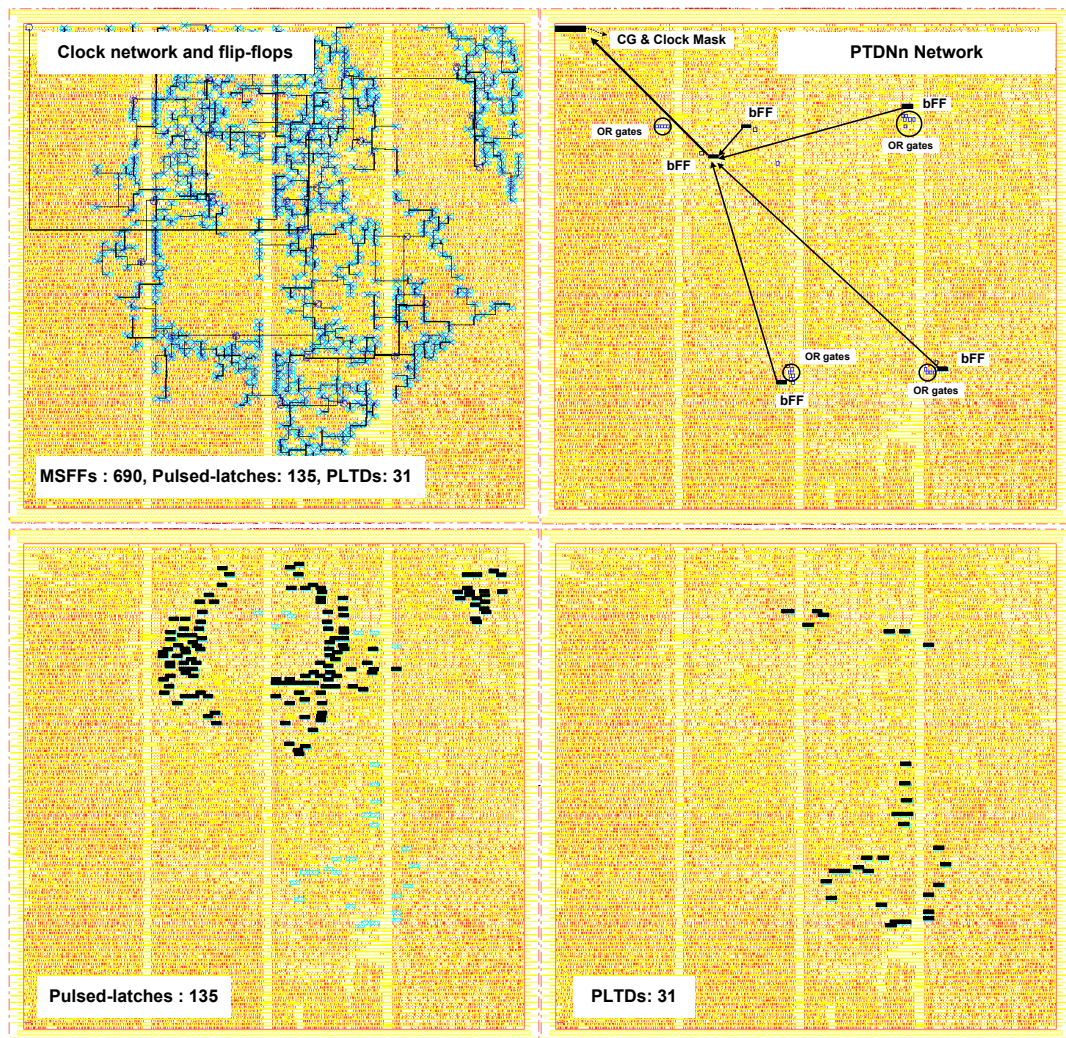
Figure 5.32: The automated layout of a rasterizer unit with programmable time borrowing (considering PTDN$_1$) in 45nm node.

Table 5.6: Overhead summary of the implemented rasterizer in a 45nm technology.

	MSFF	CASE1	CASE2	CASE3
Design	-	PTB1	PTB2	PTB3
PTDN mode	-	PTDN1/2/3	PTDN2/3	PTDN3
Operating modes		PTB1/2/3	PTB2/3	PTB3
Control time requirement		1/2/3 cycles	2/3 cycles	3 cycles
MSFFs	856 (100%)	690 (80.61%)	690 (80.61%)	690 (80.61%)
Pulsed-latches	0 (0%)	135 (15.77%)	138 (16.12%)	139 (16.24%)
PLTDs	0 (0%)	31 (3.62%)	28 (3.27%)	27 (3.15%)
# of hold-fix buffers	-	+1150	+1148	+1145
Area (um^2)	38999.7	39950.36 (+2.44%)	39931.98 (+2.39%)	39929.49 (+2.38%)
Power (mW)	6.325	6.517 (+3.04%)	6.541 (+3.42%)	6.540 (+3.40%)

* 454.5MHz, 1.1V, and 300ps clock pulse width

5.5   *Summary*

This chapter presented effective methods for preventing timing failures. First, the TB-CG approach achieved more than eliminating the safety margin in design and improved power-performance trade-off of the design. As the timing error is prevented using time-borrowing and clock stretching, the time/energy overhead of error recovery is significantly reduced. The design and measurement of the test chip demonstrates that a system employing the proposed method can operate at a higher frequency and/or at a lower supply voltage compared to the conventional design. The proposed design can efficiently tolerate timing variations due to process, voltage, and temperature fluctuations with minimal performance penalty even at high activation probability of critical paths. In other words, as the proposed circuit enables operation at lower supply voltage under the same environmental variation, it helps reduce the voltage safety margin required for the

127

conventional design. Hence, the proposed approach allows a system to operate over a wide voltage and frequency range while maintaining the system reliability. Second, the platform-independent PTB-DCG solution is proposed. It allows trade-off between noise tolerance and performance penalty while using a fixed time-borrowing window and relaxes the required control time. The measurement results from a test chip in 130nm CMOS under DC and AC supply noise demonstrate the effectiveness of the programmable time-borrowing. The proposed circuit enables operation at lower supply voltage even under transient supply noise and can help reduce the voltage safety margin required in conventional pipelines. In addition, the analysis results with the graphic processing unit are presented to show the real area and power overhead. For this case study, the automated design flow was developed. The implemented designs with the automated design flow proved the effectiveness of the proposed ideas.

CHAPTER 6

CONCLUSIONS

The goal of this thesis is to develop methodologies for robust low-power digital systems under static and dynamic variations. Increasing static and dynamic variations due to the device scaling and the increased operating frequency limit the system performance. To improve the system performance with the limited power budget, safety margins for worst corner cases should be minimized. Even though minimizing safety margins could reduce the performance or the power loss, it also increases the risk of functional failures under variations. This thesis explored design methodologies to reduce safety margin while maintaining robust operation of digital systems. In this research, three different methodologies are proposed to compensate for different types of variations efficiently.

In chapter 3, two post-silicon tuning methods to apply AVS and ABB to 3D ICs are explored to compensate for process variations considering implementation types of 3D ICs. First, considering the block-level 3D integration (i.e., 3D system with separate clock networks), TAVS is proposed to apply adaptive supply voltage to 3D ICs. In addition, the design flows for level shifters are developed. The proposed methodology improved not only the average performance but also the variability of power consumption of 3D ICs. Second, the clock skew issue in 3D ICs is investigated considering the logic-level 3D integration. In this design case, 3D clock skews can be the critical limiting factor deciding the performance of 3D ICs. TABB is proposed to adaptively minimize the 3D clock skew and thereby, improve the variability of 3D systems. In addition, circuit techniques for variation sensors are developed. TABB with the proposed sensor technique reduced clock skew and slew variation and improved the overall performance of 3D ICs implemented in logic level with a one clock network.

In chapter 4, two non-design-intrusive circuit techniques are proposed for adaptation to increasing dynamic variations. Minimizing dynamic variations is a key challenge to minimizing the safety margins. Since dynamic variations are time-dependent variations, faster adaptation for fast changing variations can lead to lower safety margins. The proposed two circuit techniques are based on replica circuits. Thus, modification in real data paths is not required. First, fast clock modulation techniques for global and local variations are proposed. The proposed adaptation techniques achieved fast clock modulation in response to global and local transient supply noises within a clock cycle. The proposed techniques improved noise tolerance of a system while maintaining reliable operations with minimized safety margins. Second, the adaptive bias-voltage generation technique for on-chip regulators is proposed to reduce the safety margin associated with static and dynamic variations. The adaptive voltage generator allows seamless adaptation to static and dynamic variations with a reduced design cost. In addition, it enables automatic DVFS.

In chapter 5, design-intrusive methods to eliminate a safety margin are proposed. Even though the design-intrusive method requires modification in the real data paths to embed the timing error-detection and the error-management schemes into them, it does not require safety margins, which cannot be eliminated in a replica-based technique. In addition, the timing errors occur only when the critical paths are activated. Not all dynamic variations necessarily lead to timing errors. Thus, timing errors happen on the condition that the dynamic variations and the critical-path activation occur at the same time. As a result, the joint probability of dynamic variations and critical-path activation can be very low. Compared to the replica-based approaches, which do not consider the probability of critical-path activation, this design-intrusive method can be more efficient. However, if the activation probability of critical paths is high, the performance penalty associated with the error management can overshadow the benefits achieved by this methodology. In addition, the benefits come with the high design effort to modify the

core circuits. This thesis presented two design-intrusive methodologies that can minimize the penalty for error management with reduced design efforts, thereby improving effectiveness of the design-intrusive method even at high activation probability of critical paths. Furthermore, the proposed techniques are platform-independent solutions and hence, applicable to general circuits. First, this work presented time-borrowing and clock-stretching (TB-CS) methods. The proposed methodology achieved timing-error prevention in advance with the minimized performance penalty. Thus, the minimum performance can be guaranteed even at high activation probability of critical paths. However, this solution has a limitation in the operating frequency. The control time requirement from the timing error detection to the clock control limits the operating frequency of this solution. Second, programmable-time-borrowing and delay-clock-gating (PTB-DCG) method is proposed to eliminate the safety margin with relaxed control time requirement. By allowing time-borrowing over the multiple pipeline stages and delaying clock gating, the proposed technique could relax the control time requirement up to 3 cycles. Thus, it makes the solution applicable to high performance processors. In addition, a performance penalty can be minimized even at the worst case without complex controls.

This thesis presented effective solutions to minimize static variations and adapt to dynamic variations considering design types and variation types. As a result, the proposed approaches help minimize safety margins while maintaining robust operations, thereby achieving robust low-power digital systems.

Furthermore, this thesis can lead to combined solutions for a future work. Non-design-intrusive approach has advantages in terms of design effort and wide operation range. However, it cannot eliminate the safety margin associated with adaptation speed and mismatches. On the other hand, design-intrusive approach can eliminate the safety margin, but is has a limited variation-tolerance range due to the limited transparency window. Future works may involve the combined solution of non-design-intrusive and

131

design-intrusive approaches presented in this thesis. Non-design-intrusive approach can determine the operating condition without consideration of the safety margin if it is combined with design-intrusive approaches as shown in Figure 6.1. Without any safety margin, there can be timing errors due to mismatches and local variations. If these possible errors can be managed by the design-intrusive approach, the combined solution can provide a wide variation-tolerance range without any safety margin. As a result, the integrated work, which includes adaptive bias-voltage generation, clock modulation, and the error-prevention technique, can provide total solutions in the system level for minimizing static variations and tolerating dynamic variations.
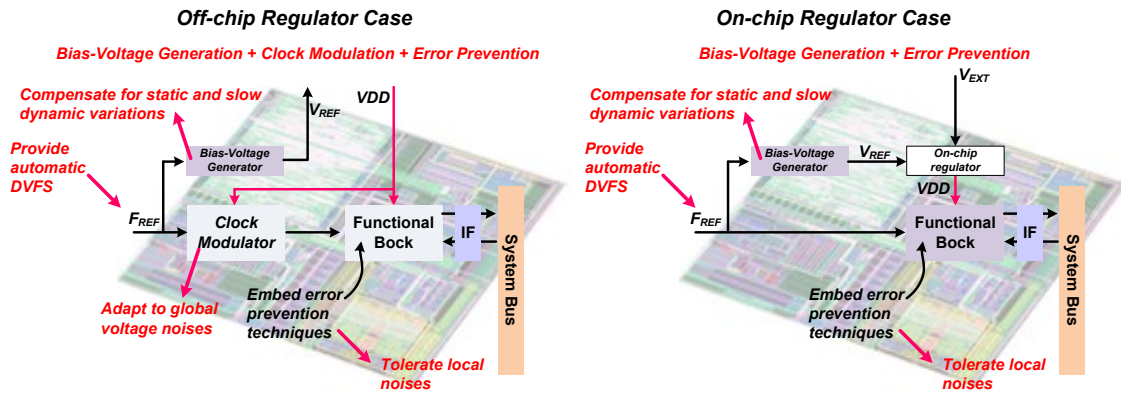
Figure 6.1: Integrated solution for static and dynamic variations.

REFERENCES

[1] S. Mukhopadhyay and K. Roy, "Modeling and estimation of total leakage current in nano-scaled CMOS devices considering the effect of parameter variation," in *Proc. International Symposium on Low Power Electronics and Design*, 2003, pp. 172-175.

[2] http://cpudb.stanford.edu.

[3] J. Tschanz, S. Narendra, R. Nair, and V. De, "Effectiveness of adaptive supply voltage and body bias for reducing impact of parameter variations in low power and high performance microprocessors," *IEEE Journal of Solid-State Circuits*, May 2003, pp. 826-829.

[4] J. W. Tschanz, J. T. Kao, S. G. Narendra, R. Nair, D. A. Antoniadis, A. P. Chandrakasan, and V. De, "Adaptive body bias for reducing impacts of die-to-die and within-die parameter variations on microprocessor frequency and leakage," *IEEE Journal of Solid-State Circuits*, vol.37, no. 11, pp.1396–1402, Nov. 2002.

[5] J. Tschanz, N. Kim, S. Dighe, J. Howard, G. Ruhl, S. Vanga, S. Narendra, Y. Hoskote, H. Wilson, C. Lam, M. Shuman, C. Tokunaga, D. Somasekhar, S. Tang, D. Finan, T. Karnik, N. Borkar, N. Kurd, and V. De, "Adaptive frequency and biasing techniques for tolerance to dynamic temperature-voltage variations and aging," in *IEEE ISSCC Dig. Tech. Papers,* Feb. 2007, pp. 292-293.

[6] W. Yao, Y. Shi, L. He, S. Pamarti, "Joint design-time and post-silicon optimization for digitally tuned analog circuits," in *Proc. IEEE/ACM International Conference on Computer-Aided Design*, pp725-730, 2009.

[7] J. Van Olmen, A. Mercha, G. Katti, C. Huyghebaert, J. Van Aelst, E. Seppala, C. Zhao, S. Armini, J. Vaes, R. C. Teixeira, M. Van Cauwenberghe, P. Verdonck, K. Verhemeldonck, A. Jourdain, W. Ruythooren, M. de Potter de ten Broeck, A. Opdebeeck, T. Chiarella, B. Parvais, I. Debusschere, T. Y. Hoffmann, B. De Wachter, W. Dehaene, M. Stucchi, M. Rakowski, P. Soussan, R. Cartuyvels, E. Beyne, S. Biesemans, and B. Swinnen, "3D stacked IC demonstration using a through silicon via first approach," in *Proc. IEEE International Electron Devices Meeting*, 2008.

[8] D. H. Kim, K. Athikulwongse, and S. K. Lim, "A study of through-silicon-via impact on the 3D stacked IC layout," in *Proc. IEEE/ACM International Conference on Computer-Aided Design*, pp674-680, 2009.

[9] F. Akopyan, C. Otero, D. Fang, S. J. Jackson, and R. Manohar, "Variability in 3-D integrated circuits," in *Proc. IEEE Custom Integrated Circuits Conference*, 2008.

[10] S. Garg and D. Marculescu, "3D-GCP: An analytical model for the impact of process variations on the critical path delay distribution of 3D ICs," in *Proc. International Symposium on Quality Electronic Design*, 2009.

[11] S. Reda, A. Si, and R. I. Bahar, "Reducing the leakage and timing variability of 2D ICs using 3D ICs," in *Proc. International Symposium on Low Power Electronics and Design*, 2009.

[12] S. Garg and D. Marculescu, "System-level process variability analysis and mitigation for 3D MPSoCs," in *Proc. IEEE/ACM Design, Automation, and Test in Europe*, 2009.

[13] S. Ozdemir, G. Memik, Y. Pan, G. Loh, A. Das, and A. Choudhary, "Quantifying and coping with parametric variations in 3D-stacked microarchitectures," in *Proc. IEEE/ACM Design Automation Conference*, 2010.

[14] C. Ferri, S. Reda, and R. I. Bahar, "Strategies for improving the parametric yield and profits of 3D ICs," in *Proc. IEEE/ACM International Conference on Computer-Aided Design*, 2007.

[15] G. Smith, L. Smith, S. Hosali, and S. Arkalgud, "Yield considerations in the choice of 3D technology," in *Proc. IEEE International Symposium on Semiconductor Manufacturing*, 2007.

[16] S. Reda, G. Smith, and L. Smith, "Maximizing the functional yield of wafer-to-wafer 3-D integration," *IEEE Transactions on VLSI Systems*, Sept. 2009.

[17] J. Verbree, E. J. Marinissen, P. Roussel, and D. Velenis, "On the cost-effectiveness of matching repositories of pre-tested wafers for wafer-to-wafer 3D chip stacking," in *Proc. IEEE European Test Symposium*, 2010.

[18] D. H. Kim, S. Mukhopadhyay, and S. K. Lim, "TSV-aware interconnect length and power prediction for 3D stacked ICs," in *Proc. IEEE International Interconnect Technology Conference*, 2009.

[19] X. Zhao, S. Mukhopadhyay, and S. K. Lim, "Variation-tolerant and low-power clock network design for 3D ICs," in *Proc. IEEE Electronic Components and Technology Conference*, 2011, pp. 2007–2014.

[20] S. Mukhopadhyay, K. Kang, H. Mahmoodi, and K. Roy, "Reliable and self-repairing SRAM in nano-scale technologies using leakage and delay monitoring," in *Proc. IEEE International Test Conference*, 2006.

[21] B. Zhang, L. Liang, and X. Wang, "A new level shifter with low power in multi-voltage system," in *Proc. IEEE International Conference on Solid-State and Integrated Circuit Technology*, Shanghai, pp. 1857-1859, 2006.

[22] B. Nikolic, V. Stojanovic, V. G. Oklobdzija, W. Jia, J. Chiu, and M. Leung, "Sense amplifier-based flip-flop," in *IEEE ISSCC Dig. Tech. Papers*, 1999.

[23] http://www.eda.ncsu.edu/wiki/FreePDK45:Contents.

[24] http://www.itrs.net/home.html.

[25] W. Kim, M. S. Gupta, G.-Y. Wei, and D. Brooks, "System level analysis of fast, per-core DVFS using on-chip switching regulators," in *Proc. IEEE International Symposium on High Performance Computer Architecture*, 2008.

[26] M. Cho, C. Liu, D. H. Kim, S. K. Lim, and S. Mukhopadhyay, "Design method and test structure to characterize and repair TSV defect induced signal degradation in 3D system," in *Proc. IEEE/ACM International Conference on Computer-Aided Design*, 2010.

[27] K. Chae and S. Mukhopadhyay, "Tier-adaptive-voltage-scaling (TAVS): a methodology for post-silicon tuning of 3D ICs," in *Proc. IEEE/ACM Asia and South Pacific Design Automation Conference*, Jan. 2012, pp. 277-282.

[28] S. Sauter, D. Schmitt-Landsiedel, R. Thewes, and W. Weber, "Effect of parameter variations at chip and wafer level on clock skews," *IEEE Transactions on Semiconductor Manufacturing*, vol. 13, no. 4, pp. 395 –400, nov 2000.

[29] A. Narasimhan and R. Sridhar, "Impact of variability on clock skew in H-tree clock networks," in *Proc. IEEE International Symposium on Quality Electronic Design*, 2007, pp. 458–466.

[30] J. Minz, X. Zhao, and S. K. Lim, "Buffered clock tree synthesis for 3D ICs under thermal variations," in *Proc. IEEE/ACM Asia and South Pacific Design Automation Conference*, 2008, pp. 504–509.

[31] X. Zhao, D. L. Lewis, H. H. S. Lee, and S. K. Lim, "Pre-bond testable low-power clock tree design for 3D stacked ICs," in *Proc. IEEE/ACM International Conference on Computer-Aided Design*, 2009, pp. 184–190.

[32] T.-Y. Kim and T. Kim, "Clock tree synthesis with pre-bond testability for 3D stacked IC designs," in *Proc. IEEE/ACM Design Automation Conference*, 2010, pp. 723–728.

[33] X. Zhao and S. K. Lim, "Power and slew-aware clock network design for through-silicon-via (TSV) based 3D ICs," in *Proc. IEEE/ACM Asia and South Pacific Design Automation Conference*, 2010, pp. 175–180.

[34] X. Zhao, J. Minz, and S. K. Lim, "Low-power and reliable clock network design for through-silicon via (TSV) based 3D ICs," *IEEE Transactions on Components, Packaging and Manufacturing Technology*, vol. 1, no. 2, pp. 247–259, 2011.

[35] T.-Y. Kim and T. Kim, "Clock tree embedding for 3D ICs," in *Proc. IEEE/ACM Asia and South Pacific Design Automation Conference*, 2010, pp. 486–491.

[36] X. Zhao and S. K. Lim, "TSV array utilization in low-power 3D clock network design," in *Proc. IEEE International Symposium on Low Power Electronics and Design*, 2012.

[37] C.-L. Lung, Y.-S. Su, S.-H. Huang, Y. Shi, and S.-C. Chang, "Fault-tolerant 3D clock network," in *Proc. IEEE/ACM Design Automation Conference*, 2011, pp. 645–651.

[38] H. Xu, V. F. Pavlidis, and G. De Micheli, "Process-induced skew variation for scaled 2-D and 3-D ICs," in *Proc. International workshop on System level Interconnect Prediction*, 2010, pp. 17–24.

[39] S. Herbert and D. Marculescu, "Variation-aware dynamic voltage/frequency scaling," in *Proc. IEEE International Symposium on High Performance Computer Architecture*, 2009, Raleigh, NC, Feb. 2009.

[40] S. Dighe, S. R. Vangal, P. Aseron, S. Kumar, T. Jacob, K. A. Bowman, J. Howard, J. Tschanz, V. Erraguntla, N. Borkar, V. K. De, and S. Borkar, "Within-die variation-aware dynamic-voltage-frequency-scaling with optimal core allocation and thread hopping for the 80-Core TeraFLOPS processor," *IEEE Journal of Solid-State Circuits*, vol. 46, no. 1, pp. 184–193, 2011.

[41] S. H. Kulkarni, D. M. Sylvester, and D. T. Blaauw, "Design-time optimization of post-silicon tuned circuits using adaptive body bias," *IEEE Transactions on Computer-Aided Design of Integrated Circuits and Systems*, vol. 27, no. 3, pp. 481-pp. 494, Mar. 2008.

[42] M. Bhushan, M. Ketchen, S. Polonsky, and A. Gattiker, "Ring oscillator based technique for measuring variability statistics," in *Proc. IEEE International Conference on Microelectronic Test Structures*, 2006, pp. 87–92.

[43] B. Wan, J. Wang, G. Keskin, and L. T. Pileggi, "Ring oscillators for single process-parameter monitoring," in *Workshop on Test Structure Design for Variability Characterization*, 2008.

[44] L. Pang and B. Nikolic, "Measurements and analysis of process variability in 90 nm CMOS," *IEEE Journal of Solid-State Circuits*, vol. 44, no. 5, pp. 1655–1663, 2009.

[45] I. A. K. M. Mahfuzul, A. Tsuchiya, K. Kobayashi, and H. Onodera, "Process-sensitive monitor circuits for estimation of die-to-die process variability," in *Proc. ACM/ IEEE International Workshop on Timing Issues in the Specification and Synthesis of Digital Systems*, 2010, pp. 83–88.

[46] K. Shinkai and M. Hashimoto, "Device-parameter estimation with on chip variation sensors considering random variability," in *Proc. IEEE/ACM Asia and South Pacific Design Automation Conference*, pp. 683-688, 2011.

[47] T. Iizuka, J. Jeong, T. Nakura, M. Ikeda, and K. Asada, "All-digital on-chip monitor for pMOS and nMOS process variability measurement utilizing buffer ring with pulse counter," in *Proc. IEEE European Solid-State Circuits Conference*, pp. 182–185, Sep., 2010.

[48] J. Jeong, T. Izuka, T. Nakura, M. Ikeda, and K. Asada, "All-digital pMOS and nMOS process variability monitor utilizing buffer ring with pulse counter," in *Proc. IEEE/ACM Asia and South Pacific Design Automation Conference*, pp. 79-80, 2011.

[49] X. Zhang, K. Ishida, M. Takamiya, and T. Sakurai, "An on-chip characterizing system for within-die delay variation measurement of individual standard cells in 65-nm CMOS," in *Proc. IEEE/ACM Asia and South Pacific Design Automation Conference*, 109-110, 2011.

[50] A. Hokazono, S. Balasubramanian, K. Ishimaru, H. Ishiuchi, C. Hu, and T. K. Liu, "Forward body biasing as a bulk-Si CMOS technology scaling strategy," *IEEE Transactions on Electron Devices*, Vol.55, No.10, October 2008, pp. 2657-2664.

[51] S. G. Narendra and A. Chandrakasan, *Leakage in Nanometer CMOS Technologies*, Springer, November 2005.

[52] T. Sato and Y. Kunitake, "A simple flip-flop circuit for typical-case designs for DFM," in *Proc. International Symposium on Quality Electronic Design*, 2007, pp.539–544.

[53] A. K. Uht, "Going beyond worst-case specs with TEAtime," *IEEE Computer*, vol.37, no.3, pp 51-56, Mar. 2004.

[54] A. Drake, R. Senger, H. Deogun, G. Carpenter, S. Ghiasi, T. Nguyen, N. James, M. Floyd, and V. Pokala, "A distributed critical-path timing monitor for a 65 nm high-performance microprocessor," in *IEEE ISSCC Dig. Tech. Papers*, Feb. 2007, pp. 398–399.

[55] R. Franch, P. Restle, N. James, W. Huott, J. Friedrich, R. Dixon, S. Weitzel, K. Van Goor, and G. Salem, "On-chip timing uncertainty measurements on IBM microprocessors," in *Proc. IEEE International Test Conference*, Oct. 2007, pp. 1–7.

[56] J. Xu, P. Hazucha, P. Huang, M. Huan, P. Aseron, F. Paillet, G. Schrom, J. Tschanz, C. Zhao, V. De, T. Karnik, and G. Taylor, "On-die supply-resonance suppression using band-limited active damping," in *IEEE ISSCC Dig. Tech. Papers*, Feb. 2007, pp. 286–603.

[57] J. Gu, R. Harjani, and C. Kim, "Distributed active decoupling capacitors for on-chip supply noise cancellation in digital VLSI circuits," in *IEEE Symp. VLSI Circuits Dig.*, Jun. 2006, pp. 216–217.

[58] N. Kurd, P. Mosalikanti, M. Neidengard, J. Douglas, and R. Kumar, "Next generation Intel® Core™ micro-architecture (Nehalem) clocking," *IEEE Journal of Solid-State Circuits*, vol. 44, no. 4, pp. 1121–1129, Apr. 2009.

[59] K. L. Wong, T. Rahal-Arabi, M. Ma, and G. Taylor, "Enhancing microprocessor immunity to power supply noise with clock-data compensation," *IEEE Journal of Solid-State Circuits*, vol. 41, no. 4, pp. 749–758, Apr. 2006.

[60] D. Jiao, and C. Kim, "A programmable adaptive phase-shifting PLL for clock data compensation under resonant supply noise," in *IEEE ISSCC Dig. Tech. Papers*, Feb. 2011, pp. 272-274.

[61] T. Fischer, J. Desai, B. Doyle, S. Naffziger, and B. Patella, "A 90-nm variable frequency clock system for a power-managed itanium architecture processor," *IEEE Journal of Solid-State Circuits*, vol. 41, no. 1, pp.218–228, Jan. 2006.

[62] S. Borkar, "Designing reliable systems from unreliable components: the challenges of transistor variability and degradation," in *Proc. IEEE/ACM International Symposium on Microarchitecture*, Nov-Dec 2005, pp. 10-16.

[63] D. Ernst, N. Kim, S. Das, S. Pant, R. Rao, T. Pham, C. Ziesler, D. Blaauw, T. Austin, K. Flautner, and T. Mudge, "Razor: A low-power pipeline based on circuit-level timing speculation," in *Proc. IEEE/ACM International Symposium on Microarchitecture*, Dec. 2003, pp. 7–18.

[64] S. Das, D. Roberts, S. Lee, S. Pant, D. Blaauw, T. Austin, K. Flautner, and T. Mudge, "A self-tuning DVS processor using delay-error detection and correction," *IEEE Journal of Solid-State Circuits*, vol. 41, no. 4, pp.792–804, Apr. 2006.

[65] S. Das, C. Tokunaga, S. Pant, W. H. Ma, S. Kalaiselvan, K. Lai, D. M. Bull, and D. T. Blaauw, "RazorII: In situ error detection and correction for PVT and SER tolerance," *IEEE Journal of Solid-State Circuits*, vol. 44, no. 1, pp.32–48, Jan. 2009.

[66] K. A. Bowman, J. W. Tschanz, N. S. Kim, J. C. Lee, C. B. Wilkerson, S. L. L. Lu, T. Karnik, and V. K. De, "Energy-efficient and metastability-immune resilient circuits for dynamic variation tolerance," *IEEE Journal of Solid-State Circuits*, vol. 44, no. 1, pp. 49-63, Jan. 2009.

[67] K. A. Bowman and J. W. Tschanz, "Resilient microprocessor design for improving performance and energy efficiency," in *Proc. IEEE/ACM International Conference on Computer-Aided Design*, 2010, pp. 85-88.

[68] J. Tschanz, K. Bowman, S.-L. Lu, P. Aseron, M. Khellah, A. Raychowdhury, B. Geuskens, C. Tokunaga, C. Wilkerson, T. Karnik, and V. De, "A 45nm resilient and adaptive microprocessor core for dynamic variation tolerance," in *IEEE ISSCC Dig. Tech. Papers*, 2010, pp. 282-283.

[69] K. A. Bowman, J. W. Tschanz, S. L. Lu, P. A. Aseron, M. M. Khellah, A. Raychowdhury, B. M. Geuskens, C. Tokunaga, C. B. Wilkerson, T. Karnik, and V. K. De, "A 45 nm resilient microprocessor core for dynamic variation tolerance," *IEEE Journal of Solid-State Circuits*, vol. 46, pp. 194-208, 2011.

[70] D. Bull, S. Das, K. Shivashankar, G. S. Dasika, K. Flautner, and D. Blaauw, "A power-efficient 32 bit ARM processor using timing-error detection and correction for transient-error tolerance and adaptation to PVT variation," *IEEE Journal of Solid-State Circuits*, vol. 46, pp. 18-31, 2011.

[71] K. Chae, S. Mukhopadhyay, C.-H. Lee, and J. Laskar, "A dynamic timing control technique utilizing time borrowing and clock stretching," in *Proc. IEEE Custom Integrated Circuits Conference*, Sept. 2010, pp. 1-4.

[72] V. G. Oklobdzija, V. Stojanovic, D. Markovic, and N. Nedovic, *Digital System Clocking, High-Performance and Low-Power Aspects*, John Wiley, January 2003.

[73] J. Rabaey, A. Chandrakasan, and B. Nikolic, *Digital Integrated Circuits: A Design Perspective*, Prentice Hall, January 2003.

[74] N. Weste and D. Harris, Eds., *CMOS VLSI Design: A Circuits and Systems Perspective*, Addison Wesley, 2005.

[75] L. T. Clark, E. J. Hoffman, J. Miller, M. Biyani, L. Luyun, S. Strazdus, M. Morrow, K. E. Velarde, and M. A. Yarch, "An embedded 32-b microprocessor core for low-power and high-performance applications," *IEEE Journal of Solid-State Circuits*, vol. 36, no. 11, pp. 1599-1608, Nov. 2001.

[76] S. D. Naffziger, G. Colon-Bonet, T. Fischer, R. Riedlinger, T. J. Sullivan, and T. Grutkowski, "The implementation of the Itanium 2 microprocessor," *IEEE Journal of Solid-State Circuits*, vol. 37, no. 11, pp. 1448-1460, Nov. 2002.

[77] H. Partovi, R. Burd, U. Salim, F. Weber, L. DiGregorio, and D. Draper, "Flow-through latch and edge-triggered flip-Flop hybrid elements," in *IEEE ISSCC Dig. Tech. Papers*, 1996, pp. 138-139.

[78] S. Kozu, M. Daito, Y. Sugiyama, H. Suzuki, H. Morita, M. Nomura, K. Nadehara, S. Ishibuchi, M. Tokuda, Y. Inoue, T. Nakayama, H. Harigai, and Y. Yano, "A 100 MHz 0.4W RISC processor with 200 MHz multiply-adder, using pulse-register technique," in *IEEE ISSCC Dig. Tech. Papers*, 1996, pp. 140-141.

[79] S. Paik, L. Yu, and Y. Shin, "Statistical time borrowing for pulsed-latch circuit designs," in *Proc. IEEE/ACM Asia and South Pacific Design Automation Conference*, 2010, pp. 675-680.

[80] V. Joshi, D. Blaauw, and D. Sylvester, "Soft-edge flip-flops for improved timing yield: design and optimization," in *Proc. IEEE/ACM International Conference on Computer-Aided Design*, Nov. 2007, pp. 667-673.

[81] K. Bowman, J. Tschanz, M. Khellah, M. Ghoneima, Y. Ismail, and V. De, "Time-borrowing multi-cycle on-chip interconnects for delay variation tolerance," in *Proc. International Symposium on Low Power Electronics and Devices*, Oct. 2006, pp. 79-84.

[82] M. Fojtik, D. Fick, K. Yejoong, N. Pinckney, D. Harris, D. Blaauw, and D. Sylvester, "Bubble Razor: An architecture-independent approach to timing-error detection and correction," in *IEEE ISSCC Dig. Tech. Papers*, 2012, pp. 488-490.

[83] K. Chae and S. Mukhopadhyay, "All-digital adaptive clocking to tolerate transient supply noise in low voltage operation," *IEEE Trans. Circuits and Systems II,* vo. 59, no. 12, pp. 893-897, Dec. 2012.

[84] OpenCores: http://opencores.org/

[85] Nangate: http://www.nangate.com/

[86] S. Dhar, D. Maksirnovi, B. Kranzen, "Closed-loop adaptive voltage scaling controller for standard-cell ASICs," in *Proc. International Symposium on Low Power Electronics and Devices*, Oct. 2002, pp. 103-107.

[87] J. Kim and M. A. Horowitz, "An efficient digital sliding controller for adaptive power-supply regulation," IEEE J. Solid-State Circuits, vol. 37, no. 5, pp. 639–647, May 2002.

[88] H. Okano, T. Shiota, Y. Kawabe, W. Shibamoto, T. Hashimoto, and A. Inoue, "Supply voltage adjustment technique for low power consumption and its application to SOCs with multiple threshold voltage CMOS," in *IEEE Symp. VLSI Circuits Dig.*, Jun. 2006, pp. 208–209.

[89] A. Raychowdhury, D. Somasekhar, J. Tschanz, V. De, "A fully-digital phase-locked low dropout regulator in 32nm CMOS," in *IEEE Symp. VLSI Circuits Dig.*, Jun. 2012, pp. 148-149.

PUBLICATIONS

[1] **Kwanyeob Chae** and Saibal Mukhopadhyay, "Resilient pipeline under supply noise with programmable-time-borrowing and delayed-clock-gating," *IEEE Trans. Circuits and Systems II, under review*.

[2] **Kwanyeob Chae** and Saibal Mukhopadhyay, "A dynamic timing error prevention technique in pipelines with time borrowing and clock stretching," *IEEE Trans. Circuits and Systems I, accepted*.

[3] **Kwanyeob Chae** and Saibal Mukhopadhyay, "All-digital adaptive clocking to tolerate transient supply noise in low voltage operation," *IEEE Trans. Circuits and Systems II,* vo. 59, no. 12, pp. 893-897, Dec. 2012.

[4] **Kwanyeob Chae**, Xin Zhao, Sung Kyu Lim, and Saibal Mukhopadhyay, "Tier adaptive body biasing: a post-silicon tuning method to minimize clock skew variations in 3-D ICs," *IEEE Trans. Components, Packaging, and Manufacturing Technology, accepted.*

[5] **Kwanyeob Chae**, Xin Zhao, Sung Kyu Lim, and Saibal Mukhopadhyay, "Post-silicon tuning method for clock network to minimize clock skews in 3D ICs," *TECHCON*, Sep. 2012.

[6] **Kwanyeob Chae**, and Saibal Mukhopadhyay, "Tier-adaptive-voltage-scaling (TAVS): a methodology for post-silicon tuning of 3D ICs," *IEEE ASP-DAC*, Feb. 2012.

[7] *[Invited]* **Kwanyeob Chae**, Minki Cho, and Saibal Mukhopadhyay, "Low-power design under variation using error prevention and error tolerance," *LATW*, 2012.

[8] **Kwanyeob Chae**, Mitchelle Rasquinha, Syed Minhaj Hassan, Sudhakar Yalamanchili, and Saibal Mukhopadhyay, "Statistical analysis of the effect of network on performance of many-core platform with 3D-stacked DRAM," *TECHCON*, Sep. 2011.

[9] *[Invited]* **Kwanyeob Chae**, Chang-Ho Lee, and Saibal Mukhopadhyay, "Timing error prevention using elastic clocking," *IEEE International Conference on IC Design and Technology*, May 2011.

[10] **Kwanyeob Chae**, Saibal Mukhopadhyay, Chang-Ho Lee, and Joy Laskar, "A dynamic timing control technique utilizing time borrowing and clock stretching," *IEEE Custom Integrated Circuits Conference*, Sept. 2010.

VITA

Kwanyeob Chae was born in Haenam, South Korea. He received his B.S. and M.S. degrees in electronics engineering from Korea University, Seoul, Korea, in 1998 and 2000, respectively. He is currently pursuing the Ph.D. degree in electrical and computer engineering with the Georgia Institute of Technology, Atlanta, GA.

He joined Samsung Electronics Co., Ltd., in 2000, where he was engaged in the development of digital circuits. His research interests include self-adaptive circuits, low-power circuits and systems, variation-tolerant design, non-volatile memories, and 3D ICs. He was a recipient of the 2007 Samsung LSI Presidential Award and the 1998 LG Semiconductor Contest Award.